MODELING, SIMULATION AND OPTIMIZATION OF ELECTROMAGNETIC SYSTEMS

by
Moadh Mallek

A thesis submitted to the Department of Mechanical Engineering,
Cullen College of Engineering
in partial fulfillment of the requirements for the degree of

DOCTOR OF PHILOSOPHY

in Mechanical Engineering

Chair of Committee: Matthew A. Franchek

Committee Member: Karolos Grigoriadis

Committee Member: Gangbing Song

Committee Member: Zheng Chen

Committee Member: Robert S. Provence

University of Houston
December 2019

DEDICATION

I dedicate my dissertation work to my family. A special feeling of gratitude to my loving parents, Said Mallek and Radhia Dammak whose words of encouragement and push for tenacity ring in my ears. My sister, Dr Atika Mallek, and her family, Hedi Bejar, Mahmoud Bejar and Youssef Bejar, my brother, Amine Mallek, and his family, Marwa Mnif and Ahmed Mallek, you have never left my side. You have made me stronger, better and more fulfilled than I could have ever imagined.

ACKNOWLEDGMENTS

Many thanks are due to my supervisor, Prof. Matthew A. Franchek, for his continued encouragement, advice and support throughout this PhD study, who was the main creator of the great ideas, techniques and whole background of this thesis. Your advice on both research as well as on my career have been priceless.

I would like to acknowledge the precious insights and guidance of the Director of Technology Development at National Oilwell Varco, Jay A. Pickett, who provided meaningful assistance in the conduct of the Halbach Array study and insightful reviews of key project results.

Thanks are also due to many other current and former members of the Team at the University of Houston, who have assisted in the research process, particularly to Dr Taoufik Wassar, Dr Mete Mutlu, Dr Amine Meziou, Dr Oussama Hattab and Dr Yingjie Tang for their many helpful and productive discussions.

Finally, I thank my parents and family for their love, encouragement and constant support for the strength to bring this task to completion.

ABSTRACT

Permanent magnet machines having Halbach Array exhibit a number of attractive features. Therefore, they have been increasingly applied to different market sectors, including aerospace, industrial, domestic, renewable, and healthcare. The need for fast global optimization, cost-effective design, and physical understanding of the relationship between parameters and performance requires a powerful analytical model. This Thesis develops a two-dimensional mathematical model estimating the torque of a Halbach Array surface permanent magnet motor. The magnetic field domain for the 2-D motor model is divided into five regions: slots, slot openings, air gap, rotor magnets and rotor back iron. Applying the separation of variable method, an expression of magnetic vector potential distribution can be represented as the Fourier series. By considering the interface and boundary conditions connecting the proposed regions, the Fourier series constants are determined. The proposed model offers a computationally efficient approach to analyzing SPM motor designs including those having a Halbach Array. Furthermore, design for traction Halbach Array motor is performed using the analytical model developed beforehand, according to two different duty cycles. In addition, global optimization via Analysis led Design procedure is proposed to evaluate the most effective design areas.

The Neodymium Iron Baron magnet has been become more expensive over the last few years, increasing the awareness of cost-effective design. Meanwhile, the needs of high electromagnetic performance, including lower torque ripple and sinusoidal air-gap flux density, are also critically required. In order to meet such

demands, magnet poles with unequal thickness, main design parameters, and Halbach magnetization are proposed in this thesis.

Other than permanent magnet motors, Halbach Array configuration is proposed in double-sided magnetic lead screw (MLS). An analytical model is developed based on the subdomain method to calculate the magnetic field distribution. This allows calculating the electromagnetic performances such as the generated thrust force. The analytical model is deployed in early stage design process of a MLS. It has been incorporated within a simulation based analysis process.

With the aid of developed analytical models and finite element analysis, the findings provide useful guidelines for design and analysis of permanent magnet machine and magnetic lead screw device having Halbach Arrays.

TABLE OF CONTENTS

LIST OF TABLES

LIST OF FIGURES

Nomenclature

Variable	Description	Unit
M	Magnetization Magnitude	A/m
B_r	Magnet Remanence	T
$B_{I,II,III}$	Flux density in region I,II,III	T
$H_{I,II,III}$	Magnet field intensity in region I,II,III	A/m
φ	Magnetic scalar potential	V
F_{pole}	Thrust force acting on one pole	lbf
τ_r	Radial magnet length	m
τ	Pole length	m
M_R	Magnet ratio	---
R_s	Outer radius	m
R_m	Inner magnets outer radius	m
R_r	Inner Magnets inner radius	m
R_0	Back iron inner radius	m
μ_0	Air permeability	H/m
μ_r	Relative permeability of permanent magnet	H/m
μ_{iron}	Relative permeability of iron	H/m
h_g	Air gap	m
h_m	Halbach array thickness	m
h_b	Back iron thickness	m
J_s	Equivalent surface current	Amp/m^2
J_{ci}	Current density	Amp/m^2

1 MOTIVATION AND OPPORTUNITY

1.1 Motivation

At the United Nations Sustainable Development Summit in 2015, more than 196 world leaders committed to a 2030 agenda that includes 17 Sustainable Development Goals (SDGs) aimed ending extreme poverty, fight inequality and taking action on climate change and more [1]. Twelve of the 17 SDGs are directly impacted by electricity. Goal number seven is to ensure access to affordable, reliable, and environmentally sustainable electrification systems. It is considered the key enabler for most of the other sustainable development objectives.

As generation moves more to renewable sources, electrification becomes the foundation of the modern society. It creates environmental benefits by shifting many end uses of electricity away from fossil fuel sources, and in many cases electricity systems have the potential to operate more efficiently compared to traditional ones.

Nowadays, global interest in clean, reliable and efficient energy generation is at its peak. Fossil fuels based energy systems are the main contributors to global pollution and environment degradation [2]. As of 2015, transportation is the US's largest contributor to the total of 5 billion tons of CO_2 emissions with 1.9 billion tons [3]. Commercial/industrial processes and manufacturing (1.4 billion tons) and residential heating and appliances (1 billion ton) are the second and third contributors to CO_2 emissions, respectively. Within the transportation sector, cars and small trucks represent more than half occupancy (55%). Today, the automotive industry is moving towards electrification, which leads to brand new electric vehicles (EVs) or electric version of existing models. EV technologies help countries shift their economies from being fossil fuel driven to ones that are sustainable and green [4]. Moreover, because electricity can be generated and oil must be extracted, electric cars have inherent price stability when it comes to fuel.

Today, more than 90% of American transportation still uses liquid fuels and a huge amount of it goes to vehicles transporting passengers [5], which produces harmful emissions and noise pollution. Many governments start taking critical steps to tackle the emissions generated by these vehicles in an attempt to cope with climate change concerns and improve population health [6]. Countries across the globe such as Japan, Korea, Denmark, Netherlands, Spain and Portugal have already established targets for EV sales. The UK and France are planning for all new cars to be electric and produce zero emissions by 2040 [7]. In Norway more than half of the new cars sold in 2017 are electric or hybrid [8]. Similarly in China, which is the leader of EV sales, more than 600 000 electric vehicles were sold. The market keeps growing and by 2025, China wants 20% of all cars sold to be electric [9]. Bikes, scooters and other light-duty vehicles powered by electric motors give their owners additional mobility in comparison to normal internal combustion engine (ICE) cars, with much less expense [10]. The lightweight of electric vehicles would easily meet the customers' requirements on portability and flexibility on the road as well, which becomes highly desirable in overcrowded modern city. This could have an immediate impact in a number of new markets for countries around the world.

Maritime transportation is another area for energy electrification. Nowadays, most commercial ships still use diesel engines, while many naval vessels use gas turbine engines [11]. Motivations to achieve higher efficiency and lower emissions will lead designs toward the electric propulsion in shipping. Transports such as passenger/cargo ships and ferries are currently developing hybrid and electric alternatives to reduce dependency on traditional fossil fuel based energy system, with zero emissions and higher operating efficiency.

Additionally, industrial applications with electric motors also tend to be more reliable, more responsive, and are more adaptable to innovative systems, especially in smaller-sized devices (e.g. robots, medical devices) [12]. Many of the recent state-of-the-art designs in electric motors are found in drones, robotics, and medical devices, which need smarter motors that can perform quick and accurate response, and reliably deliver variable levels of power on demand for short periods. Beyond the lower cost in installation and maintenance, electric motors can provide mobile robotic devices with significantly longer battery life, compared to traditional hydraulic systems.

1.2 Opportunity

Electrification means fully or partially moving from technologies that directly use fossil fuel to those that use electricity. As electricity is progressively produced from low-carbon sources such as wind and solar, there is a shift from technologies that use fossil fuels to those that use electricity often reducing emissions. Electrification also increases load for electric utilities, making it beneficial for the environment. As mentioned in the previous section, the growing set of energy efficiency opportunities in buildings, transportation and industrial sectors protect our environment by switching from inefficient fossil fuel technologies to more efficient electric ones while often also providing economic, environmental, health and equity benefits. The American Council for an Energy Efficient Economy appreciates electrification as a form of energy efficiency when it saves energy, saves money, and reduces emissions [13]. The big picture includes that both efficiency and electrification can reduce costs and emissions.

With such a complex and wide-ranging topic, an efficient electric motor is highly needed. This can help enduring the relationship between electrification and efficiency, and becoming aligned toward common goals for a clean and affordable energy future.

A motor converts electrical energy into mechanical energy to perform useful work. Reducing motor losses is the only way to improve motor efficiency. Even though standard motors operate efficiently, with standard efficiencies ranging between 80% and 93%, top efficiency motors perform significantly better. A 25% reduction in losses results in an efficiency gain of only 2%, from 92% to 94% [14]. Because most motor losses result in heat rejected into the atmosphere, reducing losses can drastically reduce cooling loads on an industrial facility's air conditioning system. As a result, motor design and optimization represents a tremendous necessity in the modern engineering. Analysis Led Design (ALD) is a strategy to change the widespread test-first culture. It has had a major impact on product development, with noteworthy benefits that include improved products performance, shorter development time and lower costs. In fact, there is an opportunity on applying ALD method to improve electric motor's electromagnetic performances and efficiency.

2 LITERATURE REVIEW AND INTRODUCTION

Permanent magnet synchronous machines (PMSM) are increasingly appealing in various implementations recently. They can be implemented on Low-speed (20-500rpm) applications such as large wind generators and high-speed (10,000rpm) applications such as electric vehicle traction

Different from the traditional wound-field synchronous machines with the DC excitation coils in the rotor, the Permanent Magnet (PM) motors are based on rotor permanent magnets for the excitation. PMSM have the capability of outstanding electromagnetic performances, such as high efficiency, high torque density and power factor.

2.1 Introduction to Permanent Magnets

Magnets are presented in two main different types, permanent magnets and electromagnets. An electromagnet is made from a coil of wire wrapped around a ferrous core and requires an electric current to generate a magnetic field unlike a permanent magnet, as its magnetism is always active; it generates its own persistent magnetic field. In addition to permanent magnets and electromagnets, there are temporary magnets. Some metals are defined as ferromagnetic, this means that they demonstrate their own magnetic properties and are described as magnetically soft materials. Magnetically soft materials such as steel conduct magnetism when attached to a magnet but this ends when the magnet is detached.

There are numerous types of permanent magnets, each manufactured differently from different materials and different properties. The five types of permanent magnets are alnico, samarium cobalt, ferrite, flexible rubber and the strongest permanent magnets, neodymium magnets. The following table provides a summary overview over strengths and weaknesses of each permanent magnet type.

Table 2-1 Magnet Types Comparison

Magnet Type	Strengths	Weaknesses
Neodymium iron boron (NdFeB)	• High magnetism • Ultra-high resistance to demagnetization • High power to volume or weight ratio	• Low operating temperature • Poor resistance to corrosion
Alnico	• High operating temperature • Good resistance to corrosion • Good magnetic stability	• Low resistance to demagnetization • Expensive
Ferrite (Fe3O4)	• Moderate operating temperature • High corrosion resistance • Cheap production	• Poor level of magnetization
Samarium cobalt (SmCo)	• Moderate magnetization • Good power to weight ratio • High corrosion resistance • Medium temperature resistance	• Expensive production cost
Magnetic rubber	• Flexible • Easy to cut • Good corrosion resistance	• Poor magnetic flux density • Low operating temperature

Neodymium magnets are the most powerful magnets with the to attract 1000 times of their own weight. They are composed mainly of neodymium, iron and boron. They are popular across a wide range of products, such as high performance permanent magnet motors and generators for automotive, industrial and domestic applications. The PM can be made into many kinds of shape and magnetized in certain orientation such as radial and parallel magnetization shown in Figure **2-1**, or any other direction. The normal direction to the surface is indicated by vector **n** and the magnetization vector by **M**. Both the structure and magnetization of PM, which form the rotor poles, influence significantly the air- gap flux density distribution, which in turn affects the electromagnetic performance of PM machines.

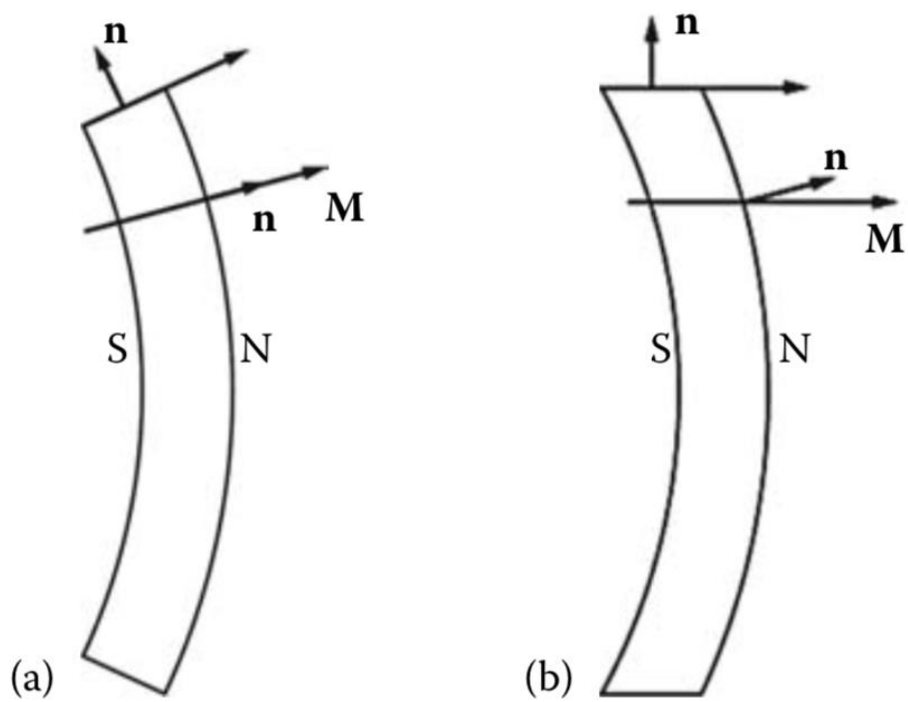

Figure 2-1 Magnetization (a) Radial Magnetization (b) Parallel Magnetization

2.2 Halbach Array

The magnetization orientation influences the quality and amplitude of the air gap flux density distribution as shown in Figure **2-2** and indirectly affects the power density in a given arrangement of the PM machines. The air gap flux density distribution affects in turn the harmonic torque generation in the machine and the presence of the harmonic torques corrodes the quality of torque output in the machine. There is also the case where the magnets can be in any direction. Such magnetization is exploited in an arrangement due to Halbach. When conventional magnets arrangement is considered, the flux lines path in a ring is shown in Figure **2-3**. It should be note that the magnets are in alternating polarity.

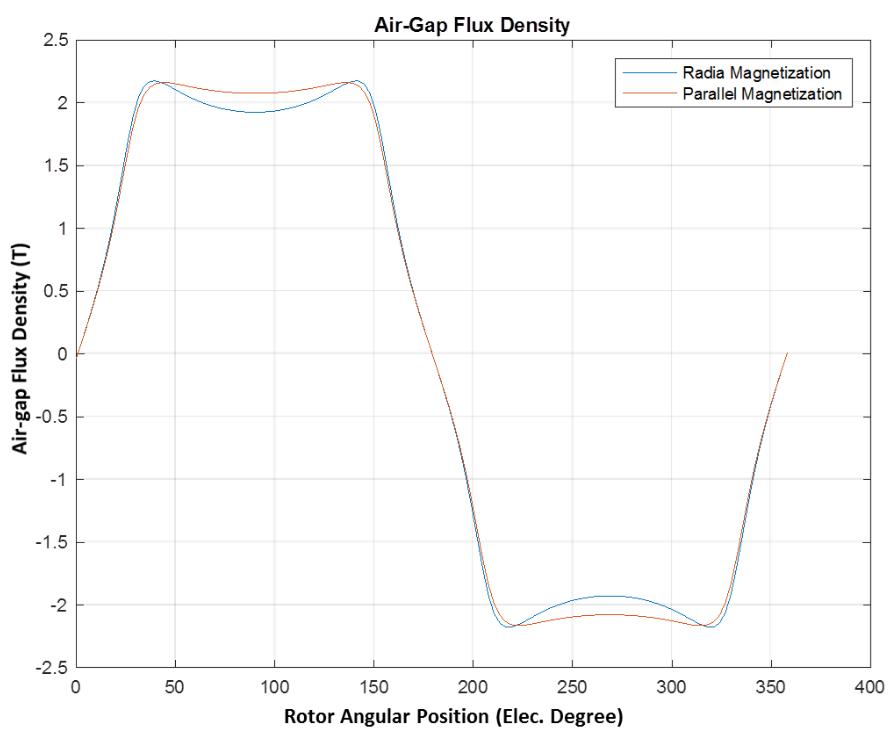

Figure 2-2 Air Gap Flux Density for Radial and Parallel Magnetization

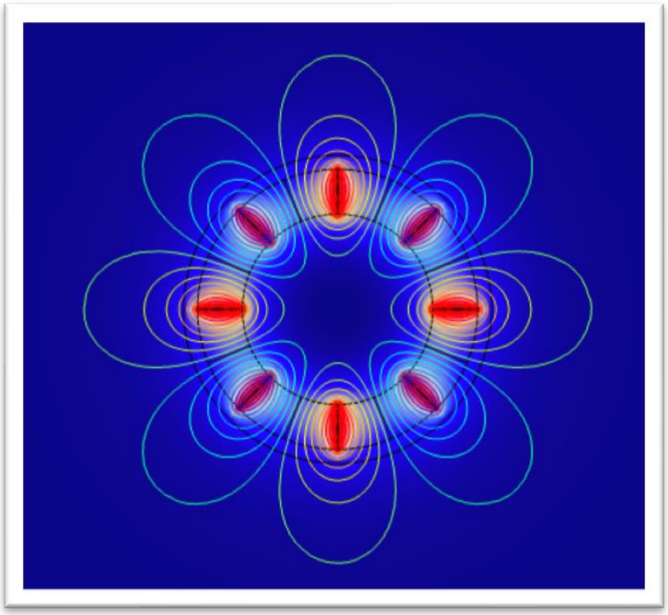

Figure 2-3 Conventional Magnet Arrangement Flux Lines in a Ring

The Halbach Array arrangement [15-18] shown in Figure **2-4** is a combination of two magnet arrays: one radial magnet array and one azimuthal magnet array. The combination is built in a way that the following magnets in the Halbach array have either a clockwise or counterclockwise magnetization. The resultant flux distribution shown in Figure **2-4** can be obtained at by summing the flux distributions of the radial and azimuthal magnet arrays. Flux lines located on bottom of the magnet array are very small compared to the number of flux lines at the top of the magnet array. Hence, there is almost no flux at the bottom of the array, implying that back iron is not required for this Halbach array. When Halbach array is applied on a ring shape, the flux lines are presented in Figure **2-5**.The flux is downward (interior) or upward (outward) depending on the orientation of the Halbach magnet segments. Clockwise orientation gives upward (outward) flux distribution and counter clockwise rotation of magnet polarities gives inward (downward) flux distribution. Consequently, the preferred orientation for machines with inner rotors and outer stators (known as inside- out machines in industrial circles) is clockwise.

Halbach magnet arrays are realized by using discrete magnet segments or blocks of magnetic material uniformly magnetized in a specific direction. Another way to build Halbach arrays is to inject sintered neodymium powder in molding process and impulse magnetizing them with the required Halbach field distribution.

Couple of features of Halbach array can be summarized as follows:

1. The increase in the flux does not always exceed 40% in practice due to non-idealities in cylindrical environment and rotor construction; system studies for rotating PMSMs [19].

2. No back iron is needed, as flux almost exists on the passive side; thus, Halbach array can be attached right with nonferrous substrates such as materials with good structural properties [20].

3. Sinusoidal distribution for ideal Halbach array, but not possible to realize in manufacturing [21].

4. Torque ripple is minimal while sinusoidal field distribution exists [22, 23].

5. Skewing of the rotor magnets and stator is not needed, which is a big saving in-manufacturing operation [24].

6. In spite of some of its unique advantages, this magnet array is yet to be

exploited in commercial applications due to its complex construction and magnetization of PMs.

7. Higher magnetic potential of the fundamental in a linear motor is theoretically proven [25].

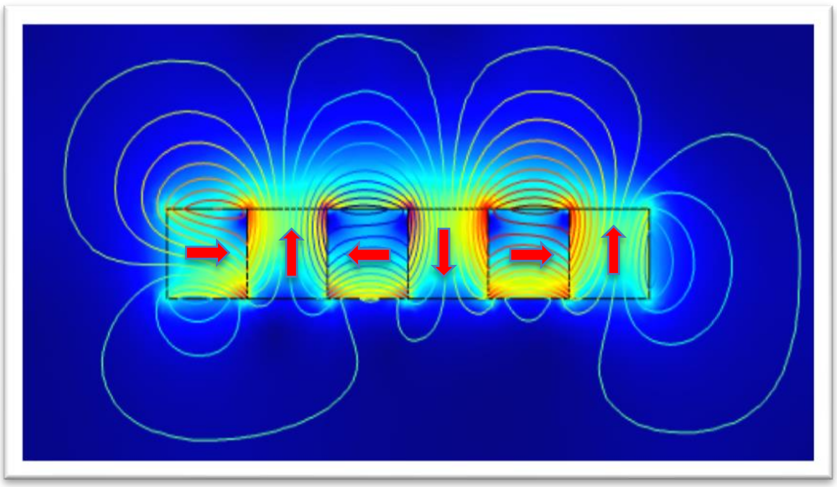

Figure 2-4 Halbach Array arrangement and Flux Lines

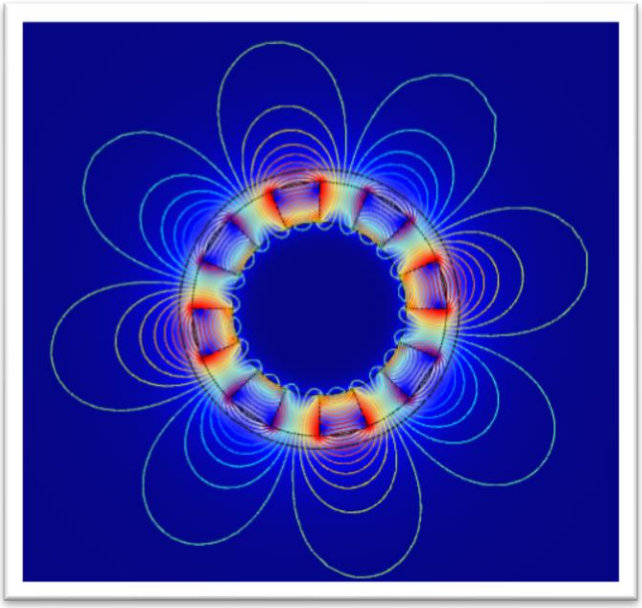

Figure 2-5 Halbach Array Flux Lines on a Ring

The main drawback of the Halbach Array geometry is that it is difficult to manufacture. All of the magnetic segments repel each other in a Halbach Array, which create a variety of assembly issues:

- Needing to assemble the magnets magnetized
- Combating the forces during assembly
- Ensuring the assembly will hold together during its use

2.3 Permanent Magnet Machines

The electromagnetic poles with windings requiring an electric energy supply are replaced with PM in compact dc machines. Similarly in synchronous machines, the PM poles substitute the usual electromagnetic field poles in the rotor.

2.3.1 Permanent Magnet Machines Configuration

The PM machines are classified on the basis of the direction of field flux, radial field: where the flux is along the radius of the machine [26, 27], and axial field: where the flux is on the axis direction of the machine [28, 29].

In the radial field version, the magnets are placed in many ways on the rotor. Different ways of arranging magnets on the rotor have produced many types of PM synchronous machines.

2.3.1.1 Surface Mounted PM machines

Figure **2-6** shows the magnets mounted on the surface of the outer boundary of rotor laminations. Such a machine configuration is called Surface PM machine (SPM). This configuration delivers the highest air gap flux density as it directly faces the air gap without the interruption of any other medium such as part of rotor laminations [30]. Drawbacks of such machine type are lower structural integrity and lower mechanical robustness, as they are not fitted into the rotor laminations to their thickness. With respect to this mechanical issue, the rotor sleeves made from either carbon fiber or Titanium are habitually used in SPM rotors [31, 32].

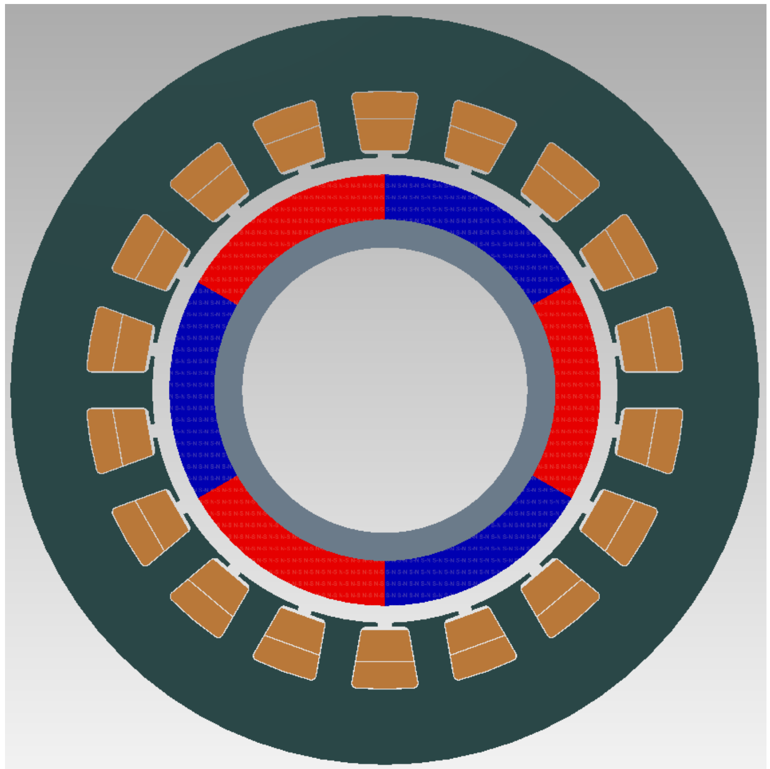

Figure 2-6 Surface Mounted PM motor

2.3.1.2 Interior Mounted PM machines

Figure **2-7** shows the placement of magnets in the middle of the rotor laminations in radial orientation. Such a machine configuration is called interior PM machine (IPM). The interior PM rotor construction is mechanically robust and consequently appropriate for high-speed applications. The manufacturing of this configuration is more complex than the surface mount or inset magnet rotors. The IPM allows various structures for embedding PMs. Examples of Rotor shapes are presented in Figure **2-8**; V-shape of magnet, double magnet shape, delta shape, hybrid delta shape, hybrid double shape [33].

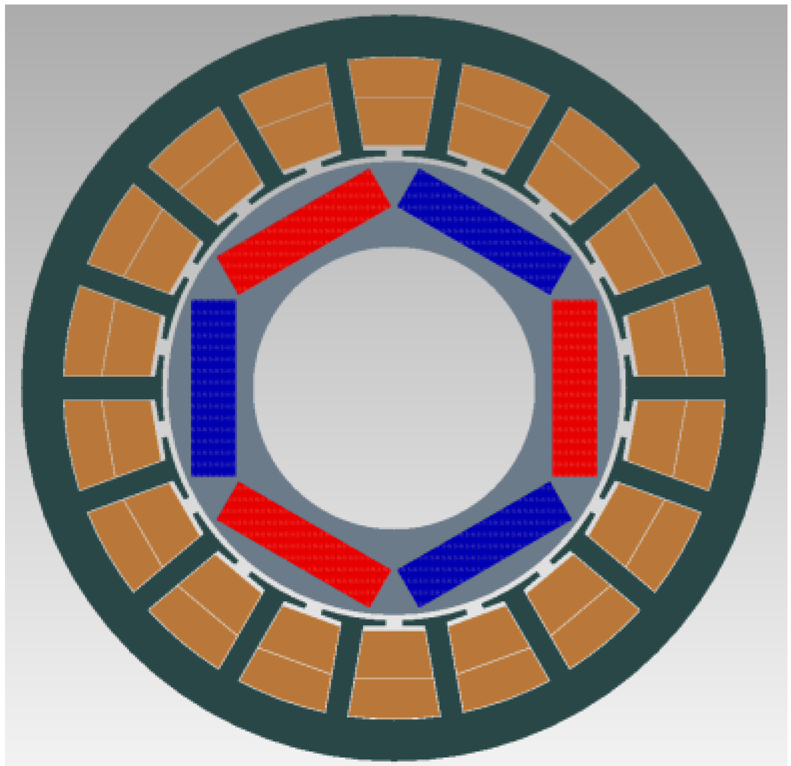

Figure 2-7 Interior PM motor

Figure 2-8 Interior Permanent Magnet Synchronous Motor Design

2.3.2 Winding Layout in PM machines

In the stator, the winding layouts are divided into concentrated and distributed windings, where both single and double layer windings can be adopted [34-41]. The double layer winding is shown in Figure 2-9, which is employed in distributed winding machines. The concentrated winding layout adopts two configurations; single layer shown in Figure 2-10 and double layer in the form of two adjacent radial layers winding shown in Figure 2-11. The double layer has two forms; the two adjacent radial layers or the two layers on top of each other.

The double layer layout displays lower harmonic contents than the single layer winding owing to reduced harmonic winding factor and increased coil number per phase [42]. The PM machine adopting concentrated double layer winding presents shorter end winding length, lower magneto motive force (MMF), lower spatial harmonic contents, lower torque ripple and higher efficiency than PM machine equipped with single layer winding. Nonetheless, PM machine having concentrated single layer winding exhibits higher flux weakening capability and self-inductance, higher fault tolerant. Moreover, this configuration improves electric isolation potentials [43]. On the other hand, PM machines having concentrated winding provides higher least common multiple number between stator slot number and rotor pole number, which achieves higher cogging torque frequency and lower cogging torque magnitude than PM machine having distributed winding. This last statement is valid except for the developed cases of 3-phase machine having coil pitch equal to 2 [44].

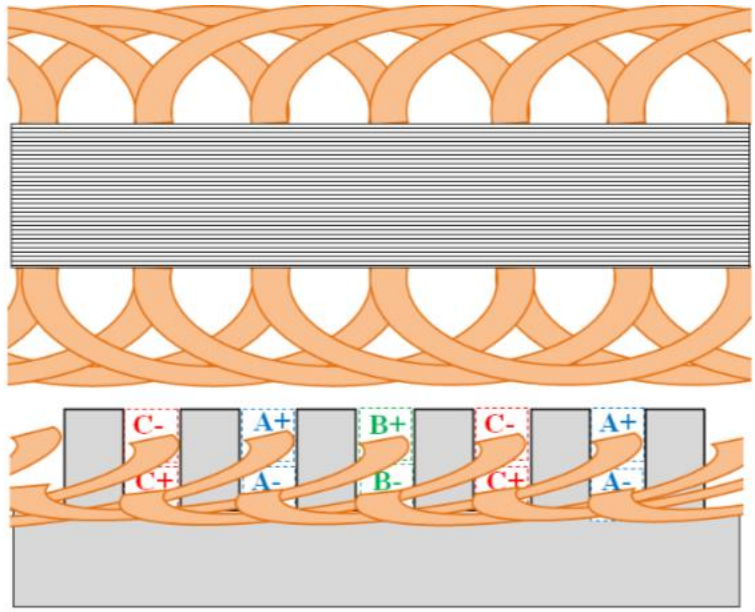

Figure 2-9 Distributed Winding Configuration Double Layer

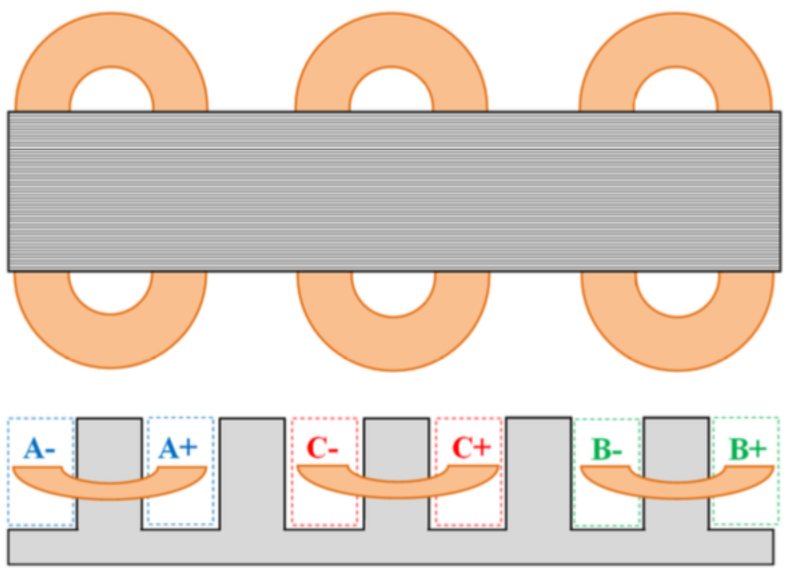

Figure 2-10 Concentrated Winding Configuration Single Layer

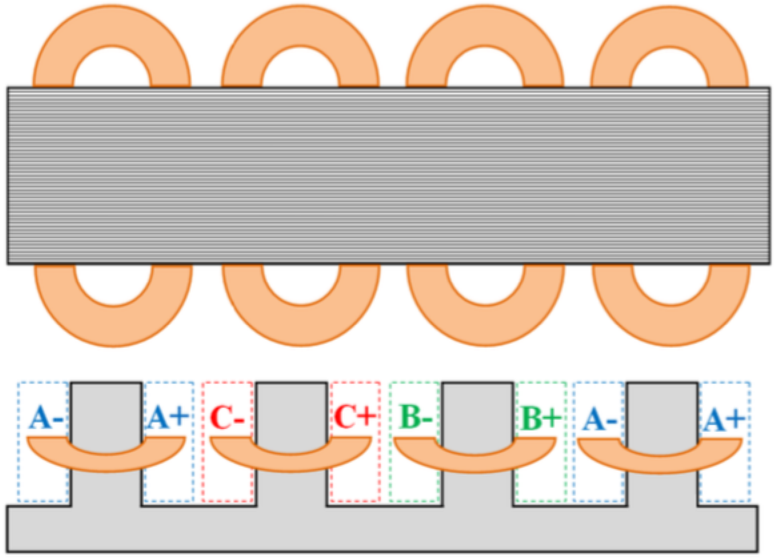

Figure 2-11 Concentrated Winding Configuration Double Layer

2.4 Losses Analysis in PM machines

The efficiency of a motor depends of intrinsic losses that can be reduced only by changes in motor design. There are various kinds of losses associated with machines when electrical and mechanical energy conversion happens. The main losses in PM machines are core loss, winding loss, magnet loss and friction losses. Core (iron) loss represents energy required to magnetize the core material (hysteresis) and includes losses due to generation of eddy currents that flow in the core. Then the iron losses are

$$P_{iron} = P_h + P_e + P_{ex} = k_h \hat{B}^b \omega_s + k_e \hat{B}^2 \omega_s^2 + k_{ex} \hat{B}^{1.5} \omega_s^{1.5} \tag{2-1}$$

represented by the sum of hysteresis, excess and eddy current losses [45]:

where k_h , k_e and k_{ex} $_{are}$ hysteresis, eddy current and excess losses coefficients, β is Steinmetz constant (equal to 1.8-2.2 [45]), $\hat{B}$ is the peak flux density and ωs is the angular frequency. The iron loss increases considerably as speed increases. Thus, several methods including appropriate slot/pole combination, optimal slot opening width, magnet shaping and thin lamination are used to effectively reduce the iron loss [46-48]. While the core loss in rotor lamination is usually small because the PM field is stationary in the machine axis, it is still noticeable and heating the magnets. Hence, this increase of temperature risks the magnets to suffer irreversible demagnetization because of stator slotting and armature reaction field harmonics. The eddy current loss in the magnet exists, since the majority of magnets are conductive. Generally, the magnet loss are classified into skin and resistance limited eddy current losses. The magnet loss directly increases the temperature of magnet; consequently it is unavoidably to be minimized to avoid magnet characteristic deterioration. In order to minimize the magnet loss, couple methods can be applied to PM machine during machine design [49, 50]. Therefore, circumferential and radial magnet segmentations, which reduce resistance-limited loss, can be adopted. In addition, conductive retaining sleeve, which reduces skin-limited loss, can be implemented.

2.5 **Modeling of Magnetic Field methods**

As regards to the advent Halbach magnetization applications, the necessity of accurate prediction and optimization of electromagnetic performance for PM machines and devices having Halbach array becomes increasingly hypercritical. The magnetic field models are extensively used to facilitate prediction of electromagnetic performance for PM machines. They are classified into two categories: numerical and analytical models. Commonly, numerical models also known as Finite Element Methods (FEA) are very accurate and capable of considering saturation effects, however the majority of analytical models are fast and simple. Nonetheless, they cannot account for saturation effects.

2.5.1 Numerical Methods

The FEA models are very powerful with the widespread availability and development of computer devices. They are capable of handling large systems of equations, nonlinearities, and complicated geometries. As the FEA models are extremely accurate and capable of accounting saturation effect, the variety of commercial software for machine design are established based on FEA, e.g, Ansys Maxwell, Infylitica, Flux, JMAG, Vector Field and MotorCad etc. Yet, FEA is very complicate for modeling 3D structure and time-consuming. In following chapters, numerical models are used to validate the accuracy and validity of analytical models.

2.5.2 Halbach Array Analytical Methods

The main goal of discussing analytical modeling is to accelerate and facilitate the optimal design process of electrical machines. The analytical field solution allows the analytical prediction of machines performances, trough calculation of global quantities, which, in turn, expedites machines characterization, and provides a basis for design optimization and system dynamic modeling [51]. The analytical models include 2-D slotless, 2-D slotted field models and lumped-parameter circuit model. 1-

D and 3-D models are not discussed in this thesis.

As mentioned previously, the numerical methods, such as FEA, are very prevailing; the global optimization is still very time-consuming, especially for a magnet pole having a Halbach Array. Solving physics equations become more complex as the meshing becomes finer. The numerical methods are also hard to provide insight into physical relationships between the performance and parameters. Eventually, analytical models are preferable and capable of facilitating physical understanding, an initial design and fast global optimization, while the numerical methods are suitable for the validation and tweaking of the design.

A simple 2-D field model for rectangular pole having perfectly sinusoidal magnetization was developed in [52, 53]. Then, in [54], analytical model for ideal Halbach Array is extended to cylindrical, planar and spherical structures as well. Furthermore, a 2-D model for slotless PM machine having ideal Halbach array with either air or iron cored rotor back iron was developed in [55] with the considering both internal and external rotors. More details about analytical models of Halbach array machines are presented in chapter 3. A compromise is always inevitable because the design tradeoff between performance and manufacturing. Therefore, this thesis aims to propose a general analytical model called on a sub-domain method for Halbach arrays magnetization and its application in high torque, electric vehicle, magnetic linear screw actuator.

2.6 Thesis Outline

The focus of this thesis is to propose general 2-D field analytical models to predict magnetic field and electromagnetic performance of proposed magnet poles and Halbach arrays. In Chapter 3, a two-dimensional mathematical model estimating the torque of a Halbach Array surface permanent magnet (SPM) motor with a non-overlapping winding layout is developed. An analytical field modeling and derivation with the subdomain method is developed. Then, the electromagnetic performance, including back-EMF waveforms, electromagnetic torque and cogging torque are compared with the FE results, and the impact of magnet ratio on torque improvement is analyzed. Thermal analysis is carried out in the next part. Finally, a performance comparison between a conventional and Halbach Array SPM motor is performed.

Chapter 4 describes design techniques for HA motor and compares the optimized design with the IPM used in Nissan Leaf 2012 model that are based on two standard driving cycles: the Urban Dynamometer Driving Schedule (UDDS) and US06 Supplemental Federal Test Procedure (SFTP). These driving cycles are adopted to carefully test the traction motor performance in terms of torque, efficiency, and thermal condition, while satisfying the required torque–speed requirements. The torque–speed envelope is derived under the power limit that the Nissan Leaf inverter can supply which is 80 kW. To check the temperature of the windings and magnets under various driving conditions, Thermal analysis is performed. Based on the analytical design presented in chapter 3, the torque is estimated to calculate current and losses in the HA traction motor. Accordingly, The benefits and the disadvantages of the HA motor for EV tractions can be fully elaborated. Some suggestions regarding the design of EV traction motors are provided.

Presented in chapter 5 is a MLS employing a double-sided Halbach Array. The manuscript starts by describing the structure of the proposed MLS. Next, a detailed analytical model was developed to assess the electromagnetic performances of the designed MLS by applying the scalar potential and the equivalent surface-distributed current method to calculate the generated magnetic flux and thrust force. Then, a model validation is presented based on FEA. The chapter concludes by an example of a practical application of the newly developed model and a summary of these work findings.

Finally, in Chapter 6, the main findings and conclusions are summarized. Various outstanding issues are identified and suggestions for future research are given.

3 TORQUE DENSE HALBACH ARRAY SURFACE PERMANENT MAGNET MOTORS

3.1 Introduction

Permanent magnet (PM) motors have been deployed on machine electromechanical machinery for decades, owing to their reliable performance, electrical stability and durability [56]. These motors have been the industry gold standard, finding their way into both rotary and linear applications. PM machines are largely classified into three categories based on the placement of permanent magnets, namely the (i) inset PM machine, (ii) internal PM machine and (iii) surface PM machine. To improve the electromagnetic torque density, investigations have focused on improving permanent magnet performance within the rotor. Recently, motor designs have moved from Samaraium Cobalt SmCo to Neodymium Iron Boron NdFeB. While NdFeB has higher remanence, achieving torque enhancements, such embodiments suffer from less coercivity and are prone to demagnetization. As a result, motor designs have created intricate ways to remove heat from this class of machines whereby NdFeB is applicable. Different laminate materials have also been investigated with the use of water-cooling and different magnet arrangements to improve performance. All these advancements are valuable and have improved the torque density of rotating machines. Presented in this manuscript is the application of these integrated principles to discover new magnet arrangements based on the Halbach Array.

The Halbach Array was originally discovered in the 1970's and replicated by Hans Halbach in the mid 1980s. This new magnetic array arrangement oriented the magnet poles such that the flux is magnified in a specific direction while limiting the flux in the opposite direction. Despite concentrating the magnetic flux is a desired direction; a Halbach Array may not necessarily improvement torque density. In fact, it is possible to create an adverse effect on torque density. For that reason and the associated manufacturing costs, Halbach Arrays have not found a niche in electric motor applications.

Halbach Array magnetization was proposed in many applications [57] and has become increasingly popular [56] with various topologies and applications: radial [58] and axial-field [59], slotted and slotless [60-63], tubular and planar for rotary [21, 64] or linear [65] machines. Halbach Array configurations exhibit several attractive features including a sinusoidal field distribution in air gap that results in a minimal cogging torque and a more sinusoidal back EMF waveform [18]. Thus, using Halbach Array SPM eliminates the conventional design techniques such as skewing of the stator/rotor [66], optimization of the magnet pole-arc [67] and distributed stator windings [68]. The Halbach Array magnets configuration generates a steady magnetic field in the active region which has yielded to many benefits including: (i) compact form with high torque density up to 30%, (ii) less weight due to less rotor back iron volume and (iii) lower rotor inertia [69]. Adopting Halbach Array does not always assure torque improvement in motors. To improve torque performance, the magnetization pattern of the PMs in the array must be cautiously designed. Furthermore, the theoretical electro-magnetic modeling is very advantageous to improve the control applications [70, 71]. Torque-dense motor design optimization requires a computationally efficient mathematical model parameterized by design parameters including geometric, electric and magnetic motor properties. Many studies have been dedicated to the analytical calculation of the electromagnetic devices and Halbach Array machines [72].

Liu proposed a method to divide and establish nonlinear adaptive lumped equivalent magnetic circuit (LPMC) that included the slot effect [73]. Using Kirchhoff's Laws, the model predicts the electromagnetic performance through an iterative process. The accuracy of these predictions were found to be lower than that of the subdomain analytical solutions [74]. In addition, transfer relations, such as Melcher's method, analytically predict the electromagnetic characteristics of a tubular linear actuator with Halbach Array [75]. Their work derives the generalized vector potentials due to permanent magnets and single-phase winding current using transfer relations. However, the influences of stator slot and tooth tips effects were neglected. Shen et al. applied the subdomain method for Halbach Array slotless machine [58]. The motor performance is derived through a scalar potential calculation over three regions: rotor back iron, permanent magnets and air gap. The major limitation of this approach is that the model does not account for the slot and tooth-tips effects for different winding layouts.

A two-dimensional (2D) model for SPM machines was developed in for conventional permanent magnets magnetizations [76]. A subdomain model incorporating the influence of slot and tooth-tips was developed to predict the armature reaction field for conventional SPM [77]. This particular model is valid for Halbach Array magnetization. Broadening the class of Halbach Array magnetic parameterization, a slotless motor model was developed having different pole-arc [78, 79]. This feature is employed in the developed model by introducing the so-called magnet ratio parameter that improved the electromagnetic performance over an equal pole-arc machine (conventional SPM).

The contribution of this chapter is the development of a subdomain motor model for a slotted Halbach Array SPM motor incorporating both slot and tooth-tip effects. Torque maximization is accomplished by optimizing Halbach Array magnets configuration through the introduction of the *magnet ratio*. The objective is to predict the electromagnetic characteristics quantified by cogging torque, back-EMF and electromagnetic torque. The motor embodiment is divided into five physical regions; rotor back iron, magnets region, air-gap, tooth opening and slot region. Maxwell Equations are developed for each subdomain vector potential from which the flux density is derived. The governing equations for vector potential distribution are solved using the Fourier method. This solution provides the vector potential in each subdomain expressed as a Fourier series that is a function of unknown constants. The boundary conditions are emphasized at this stage, the vector potential and magnetic field should be continuous at the interface between two subdomains. A resultant linear system of analytical independent equations relating all the unknown constants is formulated. Then, the permanent magnet flux linkage is computed as an integral of the normal flux density along the stator bore. The coil is considered as either a punctual source of current [80, 81] or a current sheet over the slot opening [82] where the slotting effect is approximated. The flux linkage is calculated by an integral of vector potential over the slot area. The flux passing through the conductors is accounted for using this method. Finally, having the flux linkage, the back-EMF and electromagnetic torque will be derived.

3.2 Methods and Mathematical Modeling

For the purposes of model development, consider the schematic view of a 10-pole/12-slot PM machine Figure 3-1. The motor has a two-segmented Halbach Array with non-overlapping windings. The 2-D mathematical model developed in this section is based on the following assumptions: (1) infinite permeable iron materials, (2) negligible end effect, (3) linear demagnetization characteristic and full magnetization in the direction of magnetization, (4) non-conductive stator/rotor laminations, and (5) the gaps between magnets have the same constant relative permeability as magnets [76].

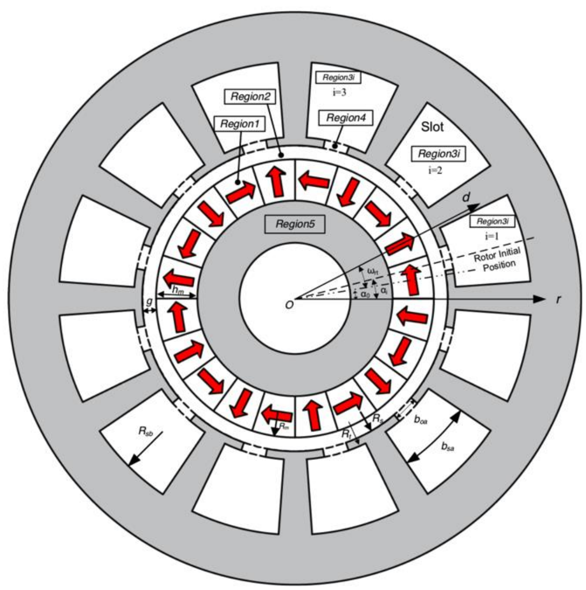

Figure 3-1 Symbols and Regions of Subdomain Model with Tooth-tips

3.2.1 Vector Potential Distribution

The magnetic flux density can be expressed as [72]

$$B = m_0 \left(m_r H + M \right). \tag{3-1}$$

and μ_r [H/m] is the relative permeability, μ_0 [H/m] is the permeability of vacuum, M [A/m] is the magnetization, and H [A/m] is the magnetic field intensity. The vector potential can be expressed using the magnetic field as

$$\nabla B = -\nabla^2 A. \tag{3-2}$$

Substituting B from (3-1) into (3-2) gives

$$\nabla^2 A = -m_0 m_r \nabla \times H - m_0 \nabla \times M = -m_0 m_r J - m_0 \nabla \times M, \tag{3-3}$$

where J [A/m^2] is the current density. Provided the eddy current does not influence the field distribution, the vector potential equation in the magnets becomes

$$\nabla^2 A = -\mu_0 \nabla \times M. \tag{3-4}$$

The 2-D field vector potential has only one component along the z-axis that must satisfy the following equations based on (3-4)

1. Magnet Region

$$\frac{\partial^2 A_{z1}}{\partial r^2} + \frac{1}{r}\frac{\partial A_{z1}}{\partial r} + \frac{1}{r^2}\frac{\partial^2 A_{z1}}{\partial^2 \alpha^2} = -\mu_0 \nabla \times M = -\frac{\mu_0}{r}\left(M_\alpha - \frac{\partial M_r}{\partial \alpha} \right) \tag{3-5}$$

2. Slot Region

$$\frac{\partial^2 A_{z3}}{\partial r^2} + \frac{1}{r}\frac{\partial A_{z3}}{\partial r} + \frac{1}{r^2}\frac{\partial^2 A_{z3}}{\partial^2 \alpha^2} = -\mu_0 J \tag{3-6}$$

3. Air-Gap, Slot Opening and Rotor Back Iron Regions

$$\frac{\partial^2 A_{z2,4,5}}{\partial r^2} + \frac{1}{r}\frac{\partial A_{z2,4,5}}{\partial r} + \frac{1}{r^2}\frac{\partial^2 A_{z2,4,5}}{\partial^2 \alpha^2} = 0 \tag{3-7}$$

where r and α are the radial and the circumferential positions respectively. The radial and circumferential components M_r Figure 3-2 and M_α Figure 3-3 are

$$M_r = \sum_{k=1,3,5,\ldots} M_{rk} \cos\left(kp\alpha\right) \tag{3-8}$$

and

$$M_\alpha = \sum_{k=1,3,5,\ldots} M_{\alpha k} \sin\left(kp\alpha\right). \tag{3-9}$$

All the series expansions in this chapter are infinite but there will be an introduction of finite harmonic orders in the following section for the sake of calculations and matrices inversions. Using the Halbach Array representation, the Fourier series coefficients are defined as

$$M_{rk} = 2\frac{B_r}{\mu_0} R_{mp} \frac{\sin\left(R_{mp}\frac{k\pi}{2}\right)}{R_{mp}\frac{k\pi}{2}} \tag{3-10}$$

and

$$M_{ak} = -2\frac{B_r}{\mu_0} R_{mp} \frac{\cos\left(R_{mp}\frac{k\pi}{2}\right)}{R_{mp}\frac{k\pi}{2}}, \quad (3\text{-}11)$$

where B_r is residual flux density of magnet and R_{mp} is the *magnet ratio* defined as the ratio of the pole arc β_r to pole pitch of a single pole β_m Figure 3-4:

$$R_{mp} = \frac{\beta_r}{\beta_m}. \quad (3\text{-}12)$$

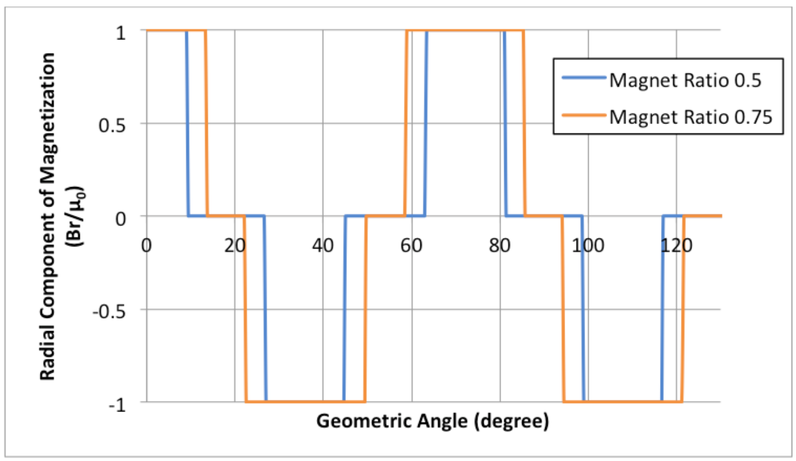

Figure 3-2 Radial Component of Magnetization for Two Magnet Ratios (0.5 and 0.75)

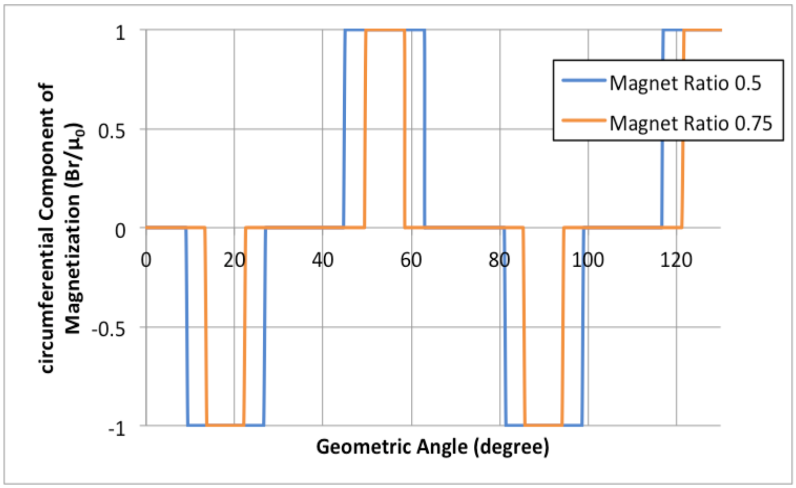

Figure 3-3 Circumferential Component for Two Magnet Ratios (0.5 and 0.75)

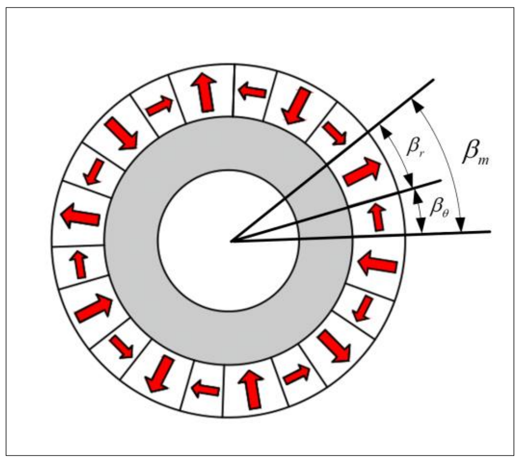

Figure 3-4 Halbach Array Magnet Ring

The current density, *J*, can be expressed as

$$J = J_{i0} + \sum_n J_{in} \cos\left[E_n\left(a + \frac{b_{sa}}{2} - a_i\right)\right], \tag{3-13}$$

$$J_{i0} = \frac{d\left(J_{i1} + J_{i2}\right)}{b_{sa}}, \tag{3-14}$$

$$J_{in} = \frac{2}{np}\left(J_{i1} + J_{i2}\cos\left(np\right)\right)\sin\left(npd / b_{sa}\right), \tag{3-15}$$

and

$$E_n = {}^{np}\!\!\diagup_{b_{sa}}, \tag{3-16}$$

where $-\frac{b_{sa}}{2} \le \alpha \le \alpha_i + \frac{b_{sa}}{2}$, and α_i and b_{sa} are the slot position and the slot width angle respectively. Thus, (3-5) becomes

$$\frac{\partial^2 A_{z1}}{\partial r^2} + \frac{1}{r}\frac{\partial A_{z1}}{\partial r} + \frac{1}{r^2}\frac{\partial^2 A_{z1}}{\partial^2 \alpha^2} = -\frac{\mu_0}{r}\left(\sum_k \left[\left(M_{\alpha ck} - kM_{rsk}\right)\cos(k\alpha) + \left(M_{\alpha sk} + kM_{rck}\right)\sin(k\alpha)\right]\right). \tag{3-17}$$

The general solution for (3-17) is

$$\begin{aligned} A_{z1} = &\sum_k \left[A_1\left(\frac{r}{R_m}\right)^k + B_1\left(\frac{r}{R_r}\right)^{-k} + \frac{m_0 r}{k^2 - 1}\left(M_{ack} - kM_{rsk}\right)\right]\cos(ka) \\ &+\sum_k \left[C_1\left(\frac{r}{R_m}\right)^k + D_1\left(\frac{r}{R_r}\right)^{-k} + \frac{m_0 r}{k^2 - 1}\left(M_{ask} + kM_{rck}\right)\right]\sin(ka) \end{aligned}, \tag{3-18}$$

where A_1, B_1, C_1 and D_1 are coefficients will be determined later and R_r and R_m are the radii of rotor back iron and magnet surfaces respectively.

The general solution for (3-7) the vector field in the air-gap, is

$$A_{z2} = \sum_k \left[A_2\left(\frac{r}{R_s}\right)^k + B_2\left(\frac{r}{R_m}\right)^{-k}\right]\cos(ka) + \sum_k \left[C_2\left(\frac{r}{R_s}\right)^k + D_2\left(\frac{r}{R_m}\right)^{-k}\right]\sin(ka), \tag{3-19}$$

where A_2, B_2, C_2 and D_2 are coefficients to be determined and R_s is the radius of inner stator surface. For non-overlapping windings, the general solution of

(3-6), the vector field in the i^{th} slot, can be derived by incorporating the boundary condition along the slot bottom on the surface of infinite permeable lamination when the circumferential component flux density is zero, namely

$$A_{z3i} = A_0 + \sum_n A_n \cos\left[E_n\left(\alpha + \frac{b_{sa}}{2} - \alpha_i\right)\right], \tag{3-20}$$

where

$$A_0 = \frac{\mu_0 J_{i0}}{4}\left(2R_{sb}^2 \ln(r) - r^2\right) + Q_{3i}, \tag{3-21}$$

$$A_n = D_{3i}\left[G_3\left(\frac{r}{R_{sb}}\right)^{E_n} + \left(\frac{r}{R_t}\right)^{-E_n}\right] + \mu_0 \frac{J_{in}}{E_n^2 - 4}\left[r^2 - \frac{2R_{sb}^2}{E_n}\left(\frac{r}{R_{sb}}\right)^{E_n}\right] \tag{3-22}$$

and

$$G_3 = \left(R_t \big/ R_{sb}\right)^{E_n}. \tag{3-23}$$

Q_{3i} and D_{3i} are coefficients to be derived using regions interactions. In the i^{th} slot opening, the vector field is derived by considering the boundary condition on both sides of the slot opening

$$A_{z4i} = D\ln(r) + Q_{4i} + \sum_m \left[C_{4i}\left(\frac{r}{R_t}\right)^{F_m} + D_{4i}\left(\frac{r}{R_s}\right)^{-F_m}\right]\cos\left(F_m\left(\alpha + \frac{b_{oa}}{2} - \alpha_i\right)\right) \tag{3-24}$$

where D, Q_{4i}, C_{4i} and D_{4i} are unknown coefficients to be determined, b_{oa} is the slot opening width and F_m is defined as follow

$$F_m = {m\pi}/{b_{oa}} . \tag{3-25}$$

The general solution for the vector field in the rotor back iron is

$$A_{z5} = \sum_k \left[A_5 \left(\frac{r}{R_r} \right)^k + B_5 \left(\frac{r}{R_0} \right)^{-k} \right] \cos(ka) + \sum_k \left[C_5 \left(\frac{r}{R_r} \right)^k + D_5 \left(\frac{r}{R_0} \right)^{-k} \right] \sin(ka), \tag{3-26}$$

where A_5, B_5, C_5 and D_5 are coefficients to be determined later, R_0 is the radius of inner rotor back iron surface.

The unknown coefficients in the expressions of vector potentials (3-18)-(3-26) are determined by applying the continuations of normal flux density and circumferential vector potential between subdomains. The details derivations are presented in the following section.

3.2.2 Boundary Conditions

The radial and circumferential components of flux density can be calculated from the vector potential distribution as

$$B_r = \frac{1}{r} \frac{\partial A_z}{\partial \alpha} \quad and \quad B_\alpha = -\frac{\partial A_z}{\partial r}. \tag{3-27}$$

In the magnet region, the magnetic flux density is

$$B = \mu_0 \mu_r H + \mu_0 M. \tag{3-28}$$

While it is expressed in the rotor back iron, air gap, slot and slot opening as

$$B = \mu_0 H. \tag{3-29}$$

3.2.2.1 Interface Between Air and Rotor Back Iron

Applying (3-29) to calculate the circumferential magnetic field intensity $H_{5\alpha}$ in rotor back iron, the boundary condition on the surface requires

$$H_{5\alpha}\Big|_{r=R_0} = \frac{1}{\mu_0 \mu_r} B_{5\alpha}\Bigg|_{r=R_0} = 0. \tag{3-30}$$

Based on (3-26) and (3-27), $B_{5\alpha}$ expression is calculated and then applied in (3-30) which leads to the following equations

$$\begin{cases} B_5 = G_5 A_5 \\ D_5 = G_5 C_5 \end{cases}, \tag{3-31}$$

where

$$G_5 = \left(\frac{R_0}{R_r}\right)^k. \tag{3-32}$$

3.2.2.2 Interface Between Rotor Back Iron and Halbach Permanent Magnets

The first boundary condition in this surface requires that the circumferential magnetic field intensity is continuous between the rotor back iron and Halbach Array permanent magnets giving

$$H_{5\alpha}\Big|_{r=R_r} = H_{1\alpha}\Big|_{r=R_r}. \tag{3-33}$$

Referring to (3-28) $H_{1\alpha}$ is calculated as

$$H_{1a} = \frac{1}{\mu_r}\left(\frac{B_{1a}}{\mu_0} - M_a\right), \tag{3-34}$$

substituting (3-34) into (3-33) gives the expressions

$$\begin{cases} A_1 G_1 - B_1 + A_5\left(G_5^2 - 1\right) = \dfrac{\mu_0 R_r}{k^2 - 1}\left(M_{rsk} - kM_{\alpha ck}\right) \\ C_1 G_1 - D_1 + C_5\left(G_5^2 - 1\right) = -\dfrac{\mu_0 R_r}{k^2 - 1}\left(M_{rck} + kM_{\alpha sk}\right) \end{cases}. \tag{3-35}$$

The second boundary condition is that the normal flux density is continuous between rotor back iron and Halbach Array permanent magnets. B_{5r} is derived from equations (3-27) and (3-29) while B_{1r} is calculated from equations (3-27) and (3-28).

$$B_{5r}\Big|_{r=R_r} = B_{1r}\Big|_{r=R_r} \tag{3-36}$$

leading to

$$\begin{cases} A_1 G_1 + B_1 - A_5\left(G_5^2 + 1\right) = \dfrac{\mu_0 R_r}{k^2 - 1}\left(kM_{rsk} - M_{\alpha ck}\right) \\ C_1 G_1 + D_1 - C_5\left(G_5^2 + 1\right) = -\dfrac{\mu_0 R_r}{k^2 - 1}\left(kM_{rck} + M_{\alpha sk}\right) \end{cases}. \tag{3-37}$$

3.2.2.3 Interface Between Rotor Back Iron and Halbach Permanent Magnets

Firstly, the circumferential magnetic field intensity is continuous between the air gap and the Halbach Array permanent magnets

$$H_{1\alpha}\Big|_{r=R_m} = H_{2\alpha}\Big|_{r=R_m}. \tag{3-38}$$

Referring to (3-29), $H_{2\alpha}$ is calculated as

$$H_{2\alpha} = \frac{B_{2\alpha}}{\mu_0}. \tag{3-39}$$

Substituting (3-39) into (3-38) and given $H_{1\alpha}$ from (3-34), we conclude

$$\begin{cases} -A_1 + B_1 G_1 + \mu_r A_2 G_2 - \mu_r B_2 = \dfrac{\mu_0 R_m}{k^2-1}\left(kM_{\alpha ck} - M_{rsk}\right) \\ -C_1 + D_1 G_1 + \mu_r C_2 G_2 - \mu_r B_2 = \dfrac{\mu_0 R_m}{k^2-1}\left(M_{rck} + kM_{\alpha sk}\right) \end{cases}. \tag{3-40}$$

Secondly, the normal flux density is continuous between the air gap and the Halbach Array permanent magnets

$$B_{2r}\Big|_{r=R_m} = B_{1r}\Big|_{r=R_m} \tag{3-41}$$

from which the following expressions can be derived

$$\begin{cases} A_1 + B_1 G_1 - B_2 - A_2 G_2 = \dfrac{\mu_0 R_m}{k^2-1}\left(kM_{rsk} - M_{\alpha ck}\right) \\ C_1 + D_1 G_1 - D2_2 - C_2 G_2 = -\dfrac{\mu_0 R_m}{k^2-1}\left(kM_{rck} + M_{\alpha sk}\right) \end{cases}. \tag{3-42}$$

3.2.2.4 Interface Between Air Gap and Slot Opening

Based on (3-24) and (3-27), the circumferential component flux density within the slot opening

$$B_{4i\alpha} = -\frac{D}{r} - \sum_m \frac{F_m}{R_s}\left[C_{4i}\left(\frac{R_s}{R_t}\right)\left(\frac{r}{R_t}\right)^{F_m-1} - D_{4i}\left(\frac{r}{R_s}\right)^{-F_m-1}\right]\cos\left(F_m\left(\alpha + \frac{b_{oa}}{2} - \alpha_i\right)\right). \qquad (3\text{-}43)$$

Since the stator core material is infinitely permeable which make the circumferential component flux density $B_{s\alpha}$ along the stator bore outside the slot opening equal to zero. Along the stator bore, the circumferential component flux density is expressed as [76]

$$B_{s\alpha} = \sum_k \left[C_s \cos(k\alpha) + D_s \sin(k\alpha)\right] \qquad (3\text{-}44)$$

where

$$C_s = \sum_i \sum_m \left(-\frac{F_m}{R_s}\left(C_{4i}G_4 - D_{4i}\right)\right)\eta_i + \sum_i \left(-\frac{D}{R_s}\right)\eta_{i0}, \qquad (3\text{-}45)$$

$$D_s = \sum_i \sum_m \left(-\frac{F_m}{R_s}\left(C_{4i}G_4 - D_{4i}\right)\right)\xi_i + \sum_i \left(-\frac{D}{R_s}\right)\xi_{i0}, \qquad (3\text{-}46)$$

$$\eta_i(m,k) = -\frac{k}{\pi\left(F_m^2 - k^2\right)}\left[\cos(m\pi)\sin\left(k\alpha_i + kb_{oa}/2\right) - \sin\left(k\alpha_i - kb_{oa}/2\right)\right], \qquad (3\text{-}47)$$

$$\xi_i(m,k) = \frac{k}{\pi\left(F_m^2 - k^2\right)}\left[\cos(m\pi)\cos\left(k\alpha_i + kb_{oa}/2\right) - \cos\left(k\alpha_i - kb_{oa}/2\right)\right], \qquad (3\text{-}48)$$

$$h_{i0}(k) = 2\sin\left(kb_{oa}/2\right)\frac{\cos\left(ka_i\right)}{kp}, \qquad (3\text{-}49)$$

and

$$\xi_{i0}\left(k\right) = 2\sin\left(kb_{oa}/2\right)\frac{\sin\left(k\alpha_i\right)}{k\pi}. \tag{3-50}$$

The first boundary condition demands that the circumferential flux density is continuous between the air gap and the slot opening giving

$$B_{2\alpha}\Big|_{r=R_s} = B_{s\alpha}\Big|_{r=R_s}. \tag{3-51}$$

Having $B_{s\alpha}$ from (3-44) and calculating $B_{2\alpha}$ from (3-19) and (3-27), condition (3-51) leads to

$$\begin{cases} R_s C_s = -kA_2 + kG_2 B_2 \\ R_s D_s = -kC_2 + kG_2 D_2 \end{cases}. \tag{3-52}$$

The vector potential distribution within air gap along the stator bore is given as

$$A_s = A_{z2}\Big|_{r=R_s} = \sum_k\left[\left(A_2 + B_2G_2\right)\cos\left(k\alpha\right) + \left(C_2 + D_2G_2\right)\sin\left(k\alpha\right)\right]. \tag{3-53}$$

The vector potential distribution over the slot opening along the stator bore is

$$\begin{aligned} A_s = &\left(\sum_k\left(\left(A_2 + B_2G_2\right)s_{i0} + \left(C_2 + D_2G_2\right)t_{i0}\right)\right) \\ &+\sum_m\left[\left(\sum_k\left(\left(A_2 + B_2G_2\right)s_i + \left(C_2 + D_2G_2\right)t_i\right)\right)\cos\left(F_m\left(a + b_{oa}/2 - a_i\right)\right)\right], \end{aligned} \tag{3-54}$$

where

$$s_{i0} = \left(\frac{p}{b_{oa}}\right)h_{i0}\left(k\right), \tag{3-55}$$

$$\tau_{i0} = \left(\frac{\pi}{b_{oa}}\right)\xi_{i0}(k), \tag{3-56}$$

$$\sigma_i = \left(\frac{2\pi}{b_{oa}}\right)\eta_i(m,k), \tag{3-57}$$

and

$$\tau_i = \left(\frac{2\pi}{b_{oa}}\right)\xi_i(m,k). \tag{3-58}$$

The vector potential distribution within slot opening along the stator bore is

$$A_{z4i}\Big|_{r=R_s} = D\ln(R_s) + Q_{4i} + \sum_m\left[C_{4i}G_4 + D_{4i}\right]\cos\left(F_m\left(\alpha + \frac{b_{oa}}{2} - \alpha_i\right)\right) \tag{3-59}$$

where

$$G_4 = \left(\frac{R_s}{R_t}\right)^{F_m}. \tag{3-60}$$

The second boundary condition involves the continuation vector potential for $(\alpha_i - \frac{b_{sa}}{2} \leq \alpha \leq \alpha_i + \frac{b_{sa}}{2})$ is

$$A_{z4i}\Big|_{r=R_s} = A_s, \tag{3-61}$$

thus

$$Q_{4i} = \sum_k\left[(A_2 + B_2G_2)\sigma_{i0} + (C_2 + D_2G_2)\tau_{i0}\right] - D\ln(R_s) \tag{3-62}$$

and

$$D_{4i} + C_{4i} G_4 = \sum_k \left[\left(A_2 + B_2 G_2 \right) \sigma_i + \left(C_2 + D_2 G_2 \right) \tau_i \right]. \tag{3-63}$$

3.2.2.5 Interface Between Slot Opening and the Slot

The circumferential component of the flux density along the interface between the slot and the slot opening is derived from (3-24) and (3-27) [76]

$$B_{4i\alpha}\Big|_{r=R_t} = B_{4i\alpha 0} + \sum_m B_{4i\alpha m} \cos\left(F_m \left(\alpha + b_{oa}/2 - \alpha_i \right) \right), \tag{3-64}$$

where

$$B_{4i\alpha 0} = -\frac{D}{R_t} \tag{3-65}$$

and

$$B_{4i\alpha m} = -\frac{F_m}{R_t} \left(C_{4i} - D_{4i} G_4 \right). \tag{3-66}$$

The circumferential flux density in the slot along the outer radius of the slot opening is null since the stator core material is infinitely permeable. This component along R_t is expressed into Fourier series over $(\alpha_i - \frac{b_{sa}}{2} \leq \alpha \leq \alpha_i + \frac{b_{sa}}{2})$ as

$$B_{4i\alpha}\Big|_{r=R_t} = B_0 + \sum_n B_n \cos\left(E_n \left(\alpha + b_{sa}/2 - \alpha_i \right) \right), \tag{3-67}$$

where

$$B_0 = B_{4i\alpha 0} \varphi_{ex}, \tag{3-68}$$

$$B_n = B_{4ia0}\varphi_0 + \sum_m B_{4iam}\varphi\ , \tag{3-69}$$

$$\varphi_{ex} = \frac{b_{oa}}{b_{sa}}, \tag{3-70}$$

$$\varphi_0(n) = \frac{4}{n\pi}\cos(n\pi/2)\sin(E_n b_{oa}/2) \tag{3-71}$$

and

$$\varphi(m,n) = -\frac{2}{b_{sa}}\frac{E_n}{F_m^2 - E_n^2}\left[\cos(m\pi)\sin\left(E_n\frac{b_{sa}+b_{oa}}{2}\right) - \sin\left(E_n\frac{b_{sa}-b_{oa}}{2}\right)\right]. \tag{3-72}$$

The circumferential flux density in the slot opening along the interface between the slot opening and the slot is

$$B_{3i\alpha}\big|_{r=R_t} = B_{3i\alpha 0} + \sum_n B_{3i\alpha n}\cos\left(E_n\left(\alpha + b_{sa}/2 - \alpha_i\right)\right), \tag{3-73}$$

where for non-overlapping winding

$$B_{3i\alpha 0} = -\frac{\mu_0 J_{i0}\left(R_{sb}^2 - R_t^2\right)}{2R_t} \tag{3-74}$$

and

$$B_{3i\alpha n} = -\frac{E_n D_{3i}\left(G_3^2 - 1\right)}{R_t} - \frac{2\mu_0 J_{in}}{R_t\left(E_n^2 - 4\right)}\left(R_t^2 - R_{sb}^2 G_3\right). \tag{3-75}$$

Applying the continuity of the circumferential component of flux density along the interface between the slot opening and the slot gives

$$B_{3ia0} = B_{4ia0}\varphi_{a} \tag{3-76}$$

and

$$B_{3ian} = B_{3ian}\varphi_{0} + \sum_{m} B_{4iam}\varphi . \tag{3-77}$$

From (3-65), (3-71), (3-74) and (3-76)

$$D = \frac{\mu_0 J_{i0}\left(R_{sb}^2 - R_t^2\right)}{2}\left(\frac{b_{sa}}{b_{oa}}\right). \tag{3-78}$$

The vector potential distribution in the slot along the radius R_t is

$$A_t = A_{z3i}\Big|_{r=R_t} = A_{3i0} + \sum_{n} A_{3in} \cos\left[E_n\left(\alpha + \frac{b_{sa}}{2} - \alpha_i\right)\right], \tag{3-79}$$

where for non-overlapping winding

$$A_{3i0} = \frac{\mu_0 J_{i0}\left(2R_{sb}^2 \ln\left(R_t\right) - R_t^2\right)}{4} + Q_{3i} \tag{3-80}$$

and

$$A_{3in} = D_{3i}\left(G_3^2 + 1\right) + \frac{\mu_0 J_{in}}{\left(E_n^2 - 4\right)}\left(R_t^2 - \frac{2R_{sb}^2 G_3}{E_n}\right). \tag{3-81}$$

The same vector potential is expressed over $\left(\alpha_i - \frac{b_{sa}}{2} \le \alpha \le \alpha_i + \frac{b_{sa}}{2}\right)$

$$A_t = A_{3t0} + \sum_{m} A_{3tn} \cos\left[F_m\left(\alpha + \frac{b_{oa}}{2} - \alpha_i\right)\right], \tag{3-82}$$

where

$$A_{3t0} = \sum_{n} A_{3in}\kappa_0 + \mu_0\!\!\not{}_{4}\, J_{i0}\left(2R_{sb}^2 \ln\left(R_t\right) - R_t^2\right) + Q_{3i}, \tag{3-83}$$

$$A_{3tm} = \sum_{n} A_{3in}\kappa, \tag{3-84}$$

$$\kappa_0 = \left(\frac{b_{sa}}{b_{oa}}\right)\varphi_0\left(n\right), \tag{3-85}$$

and

$$\kappa = \left(\frac{b_{sa}}{b_{oa}}\right)\varphi\left(m,n\right). \tag{3-86}$$

From the vector potential within the slot opening

$$A_{z4i}\Big|_{r=R_t} = D\ln\left(R_t\right) + Q_{4i} + \sum_{m}\left(C_{4i} + D_{4i}G_4\right)\cos\left(F_m\left(\alpha + \frac{b_{oa}}{2} - \alpha_i\right)\right). \tag{3-87}$$

Applying the continuity of the vector potential along the interface between the slot opening and the slot

$$A_t = A_{z4i}\Big|_{r=R_t}. \tag{3-88}$$

The following equations can now be developed

$$Q_{3i} = Q_{4i} + D\ln\left(R_t\right) - \frac{\mu_0 J_{i0}}{4}\left(2R_{sb}^2 \ln\left(R_t\right) - R_t^2\right) - \sum_{n} A_{3in}\kappa_0 \tag{3-89}$$

and

$$C_{4i} + D_{4i} G_4 = \sum_n A_{3in} \kappa. \tag{3-90}$$

3.2.3 Back EMF and Torque Calculations

From the field solutions generated in the previous subsection, other important global quantities for evaluating the performances of surface-mounted PM machines are developed. In this subsection, relevant electromagnetic characteristics, such as the flux linkage and the back EMF, are obtained based on the subdomain models. Also developed are expressions for the electromagnetic torque and cogging torque.

3.2.3.1 Flux Linkage

Flux linkage occurs when a magnetic field interacts with a material such as a magnetic field travels through a coil of wire. The flux linkage from one coil side of an arbitrary winding is calculated from the magnetic vector potential in the general equation for flux linkage. The calculation can be simplified by the mean of Stokes integral theorem

$$\psi_{i1} = \frac{LN_c}{A_s} \iint_S \vec{B} \cdot d\vec{s} = \frac{LN_c}{A_s} \iint_S \nabla \times \vec{A} \cdot d\vec{s} = \frac{LN_c}{A_s} \oint_C \vec{A} \cdot d\vec{s} = \frac{LN_c}{A_s} \int_{\alpha_i - b_{sa}/2}^{\alpha_i - b_{sa}/2 + d} \int_{R_t}^{R_{sb}} A_{z3i} \cdot r\, dr\, d\alpha, \tag{3-91}$$

where L is the stack length of the motor, A_s is the area of one coil side and N_c is the number of turns per coil.

Based on A_{z3i} in (3-20) and (3-91)

$$y_{i1} = \frac{LN_c}{A_s}\left[Q_0 d + \sum_n \frac{Q_n}{E_n} \sin\left(E_n d\right) \right], \tag{3-92}$$

where

$$Q_0 = \int_{R_t}^{R_{sb}} A_0 \cdot r\,dr \tag{3-93}$$

and

$$Q_n = \int_{R_t}^{R_{sb}} A_n \cdot r\,dr. \tag{3-94}$$

Following the same approach, the flux linkage in the other coil side of the same slot is

$$\psi_{i2} = \frac{LN_c}{A_s}\left[Q_0 d - \sum_n \frac{Q_n}{E_n} \sin\left(n\pi - E_n d\right) \right]. \tag{3-95}$$

The summation of the flux linkages associated with all the coil sides of the corresponding phase results in the total flux linkage of each phase. This calculation includes a connection matrix S_w that represents the winding distribution in the slot

$$\begin{bmatrix} \psi_a \\ \psi_b \\ \psi_c \end{bmatrix} = S_w \psi_c. \tag{3-96}$$

Presented is an estimation method for the flux linkage. These results will be used to estimate the phase back-EMF for the Halbach motor.

3.2.3.2 Back EMF

Using Lenz's law, the induced EMF always opposes the cause of its production. Here, the cause of generation of back-EMF is the rotation of armature. The armature torque produces rotation of armature. Torque is due to armature current and armature current is created by the supply voltage. Therefore, the ultimate cause of production of the back EMF is the supply voltage. The three-phase back-EMF vector is calculated by the derivative of flux linkage calculated in (3-96) with respect to time when the winding is open circuit

$$\begin{bmatrix} E_a \\ E_b \\ E_c \end{bmatrix} = \omega \begin{bmatrix} \frac{d\psi_a}{dt} \\ \frac{d\psi_b}{dt} \\ \frac{d\psi_c}{dt} \end{bmatrix}. \tag{3-97}$$

3.2.3.3 Electromagnetic and Cogging Torques

The electromagnetic torque is calculated as

$$T_{em} = \left(E_a I_a + E_b I_b + E_c I_c\right) \Big/ \omega . \tag{3-98}$$

Concerning the cogging torque, many methods have been used such as the lateral force [83], complex permeance [84, 85] and energy [86, 87]. The task of calculating and minimizing the cogging torque in PM machines is typically accomplished using either the virtual work or Maxwell stress tensor methods. In this development, the Maxwell stress tensor is proposed providing accurate prediction of the air-gap field by way of the subdomain method accounting for tooth-tips. The derivation is based on the open circuit field

$$T_c = \left(\frac{LR_s^2}{\mu_0} \right) \int_0^{2\pi} B_{2r} B_{2\alpha} d\alpha. \tag{3-99}$$

3.3 Results and Model Validation

Validation of the proposed electromagnetic analytical model depends on the modeling accuracy to predict motor torque with slot and tooth tip effects. A finite element analysis is used to validate the analytical model for Halbach Array machine shown in Figure 3-1 and a conventional one having both a three-phase 12-slot/10-pole embodiment. In the present validation, the simulation on the conventional and the Halbach Array SPM motors is performed by the help of the commercial FEA software MotorSolve v6.01 (Infolytica Corporation, Montréal, Canada). The motor design parameters applied in the present study are provided in Table **3-1**.

Table 3-1 Main Motor Parameter

Parameters	**Values**
Slot Number, N_s	12
Pole Number, p	10
Stator Outer Diameter, D_s	100 mm
Magnet Remanence, B_r	1.12 T
Relative Permeability, μ	1.05
Air gap Length, g	1 mm
Magnet Thickness, h_m	3 mm
Active Length, L	50 mm
Winding Turns / Coil, N_c	35
Magnet Magnetization	Radial
Stator Inner Diameter	55 mm
Tooth Tips Edge	3 mm
Slot-opening Angle	5.5°
Winding Slot Angle	14.5°
Stator Yoke Height	5 mm
Rotor Outer Diameter	53 mm
Peak Rated Current	10 A
Motor Speed	400 RPM

The non-overlapped winding layout is shown in Figure 3-5. The use of this configuration in SPM motors to meet the optimal flux weakening condition is supported. Therefore, machines made with concentrated windings have shorter end coils, which reduce the total copper ohmic losses, the length and the weight of the machine. In addition, this configuration is chosen to maximize the winding factor of 93.3% with a coil span equal to unity [88].The results for the Fourier series expansion are computed with a finite number of harmonics for k, m, and n. Generally, the limited number of harmonics needs to be considered in the analytical model to produce good results, while the mesh in the FE model must be adjusted before achieving acceptable results. The computation time of the analytical field solutions is dependent from the harmonic numbers (k, m, n), for (100, 50, 50), by way of example, the average calculation time is 14.3s (with 2.3 GHz CPU) on the Matlab platform. For the Halbach Array magnets configuration, when the magnet ratio Rmp, equal to 0.5, the predicted 2-D analytical radial flux density and MotorSolve simulation in the centerline of air gap position are presented in Figure 3-6. The resulting air gap flux density waveform distributions are distorted at the slot-openings showing that the analytical subdomain model is able to capture the slot-openings and tooth tips effects. The proposed model predicts the flux density within the considered five subdomains. MotorSolve only provides the flux density prediction for only the air-gap. The validation of flux density would promote further analysis in the demagnetization withstand ability for different magnet ratio cases and inductance prediction.

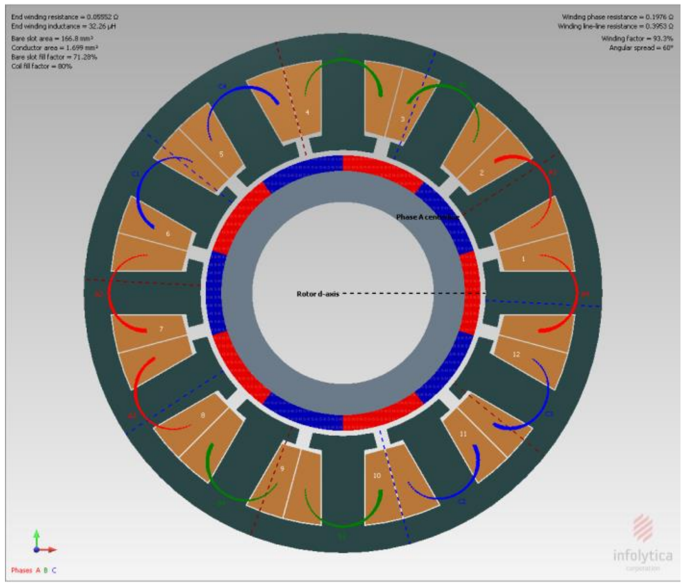

Figure 3-5 Non-Overlapping Winding Layout in MotorSolve

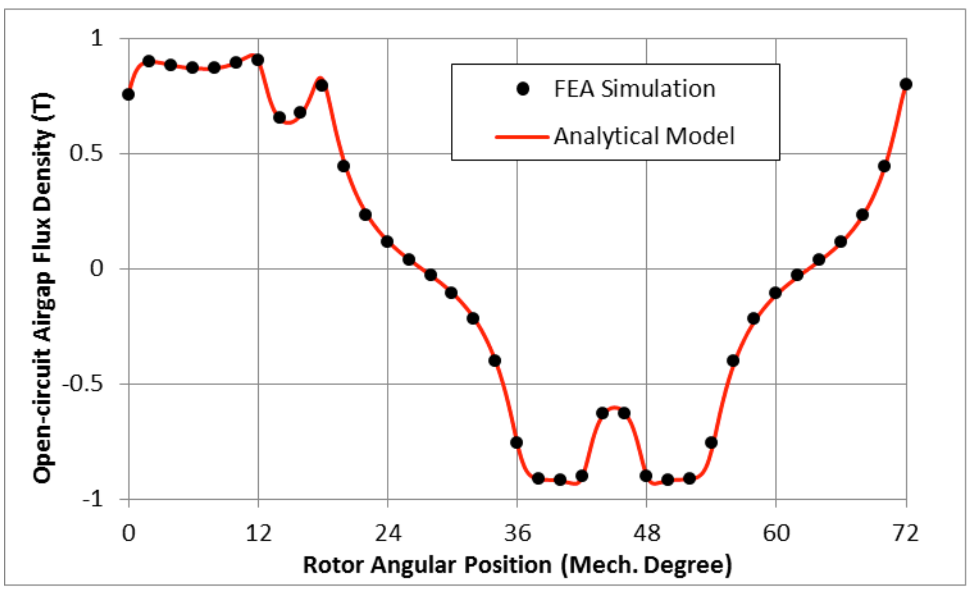

Figure 3-6 Comparison of FEA and Analytically Predicted Air-gap Flux Density

By varying the magnet ratio, the proposed model can predict a variety of magnetization patterns as shown in Figure 3-7. It should be noted that the conventional SPM magnet has a magnet ratio R_{mp} equal to unity, while the magnet ratio should be 0.5 for the model shown in Figure 3-1, when the side and the central magnet segments have the same size. The highest flux density peak value (FDPV) is given by lowest Halbach Array magnet ratio, which is approximately 10% higher than the conventional magnetization. By increasing the magnet ratio, the FDPV decreases and the shape of the flux becomes wider within each pole range. This is because the central magnet with radial magnetization becomes wider as the magnet ratio increases. The air gap flux density waveform reaches its widest and lowest peak amplitude in the magnet ratio of unity.

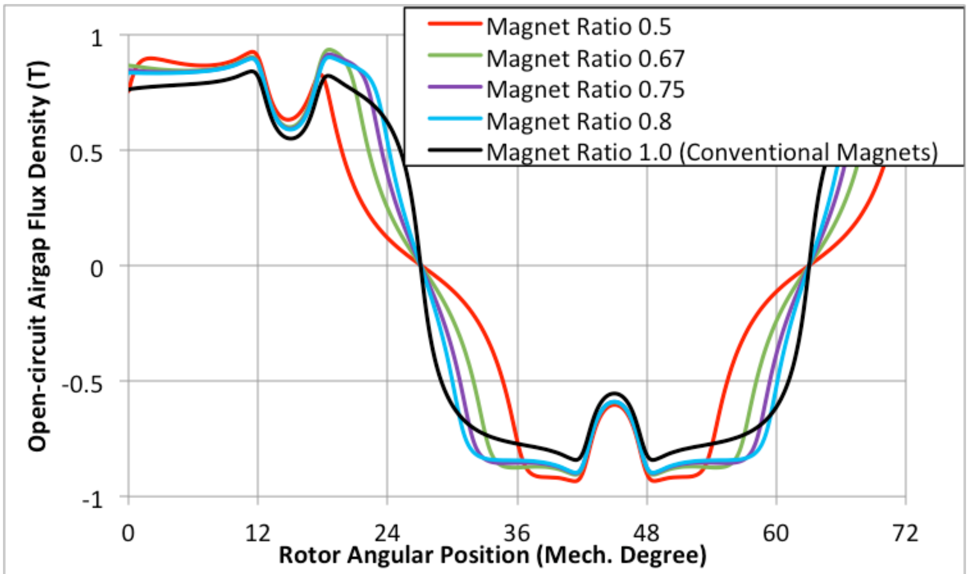

Figure 3-7 Predicted Air-gap Flux Density with Different Magnet Ratio Values

The stator windings are excited with sinusoidal currents with a peak value of 10A. Shown in Figure 3-8, Figure 3-9 and Figure 3-10 are the comparisons between the analytically calculated and FEA simulated waveforms of electromagnetic torque, cogging torque and back-EMF respectively. The analytical results provide good agreements with those obtained from FEA simulation.

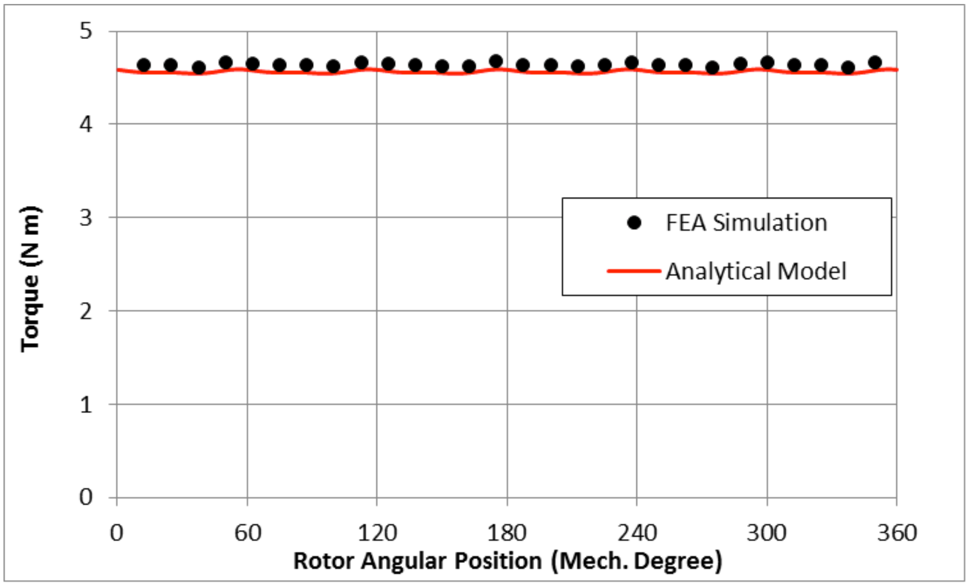

Figure 3-8 Analytical and MotorSolve FEA Predictions of Electromagnetic Torque

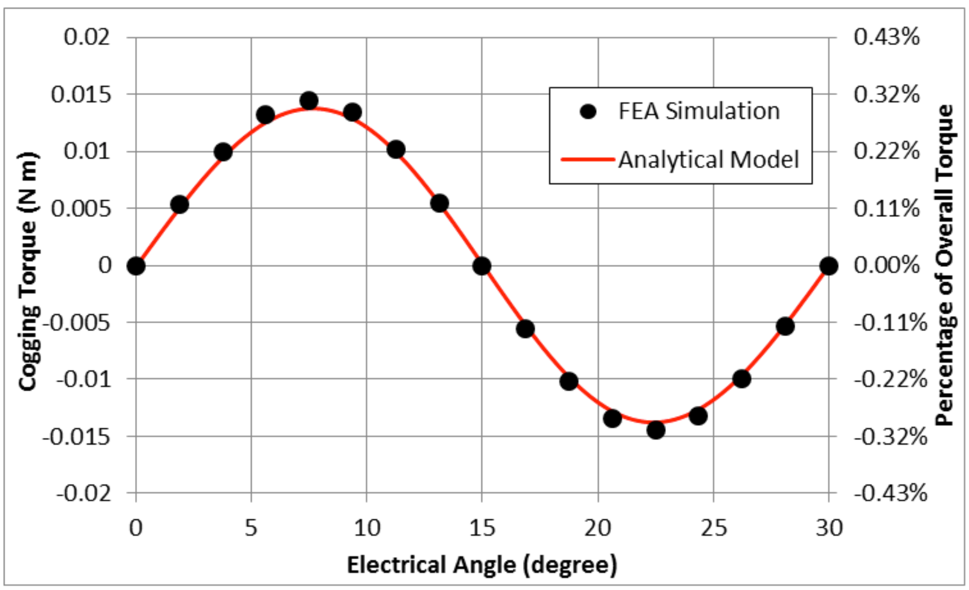

Figure 3-9 Analytical and MotorSolve Predictions of Cogging Torque

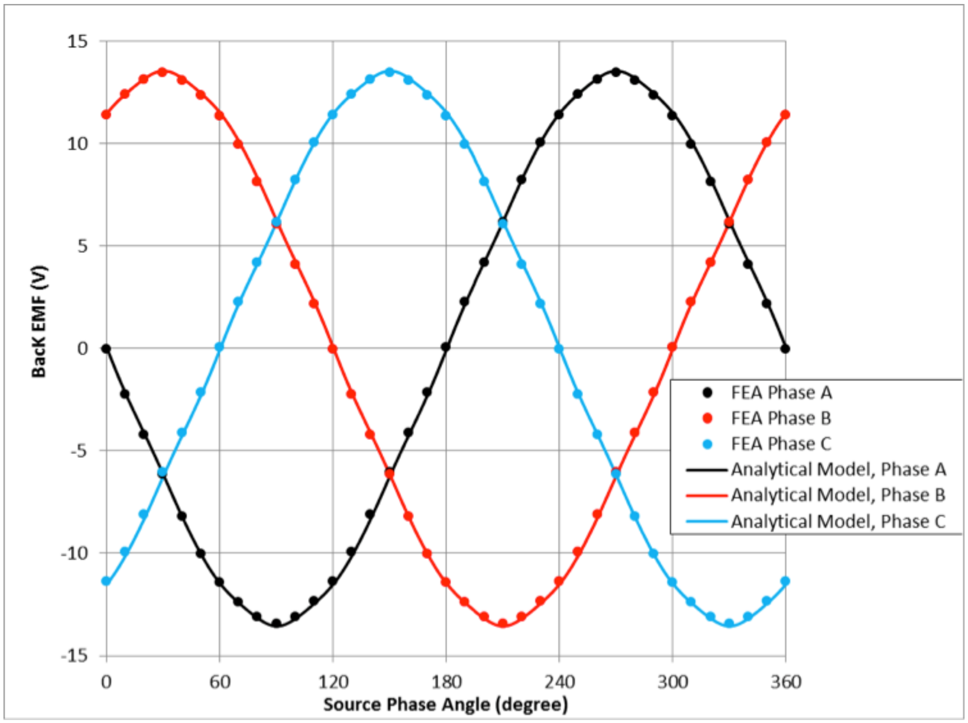

Figure 3-10 Analytical and MotorSolve Predictions of Back EMF

Shown in Figure 3-11 are the flux lines with different magnet ratio values. The flux lines are densely low in the passive region (rotor back iron) for the magnet ratio 0.5. When increasing the magnet ratio, the FDPV increases to the value of conventional magnet pattern.

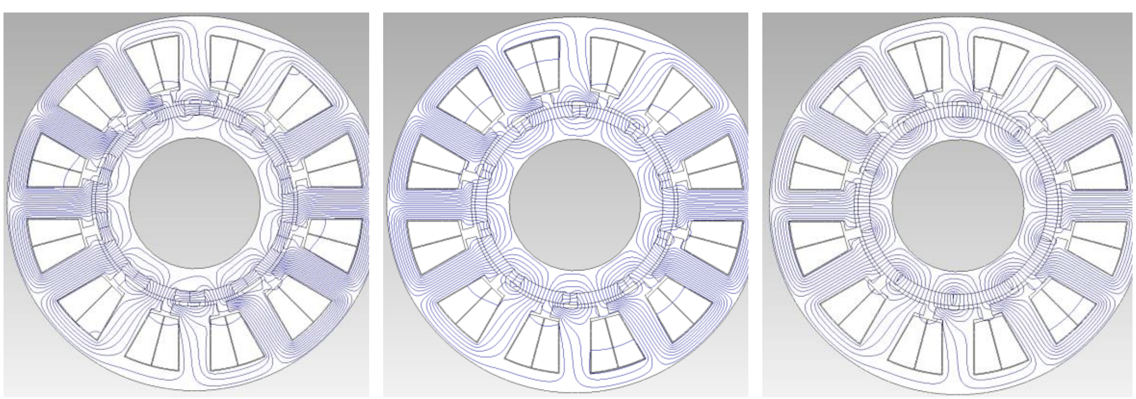

(**a**) (**b**) (**c**)

Figure 3-11 Magnetic Field Distributions: (a) Rmp=0.5; (b) Rmp=0.7; (c) Rmp=1

For comparison purposes, the electromagnetic performance for the conventional (non-Halbach) motor design with the same parameters in Table 1 is shown in Figure 3-12, Figure 3-13 and Figure 3-14. All results for the analytical calculations are in agreement with FEA simulations.

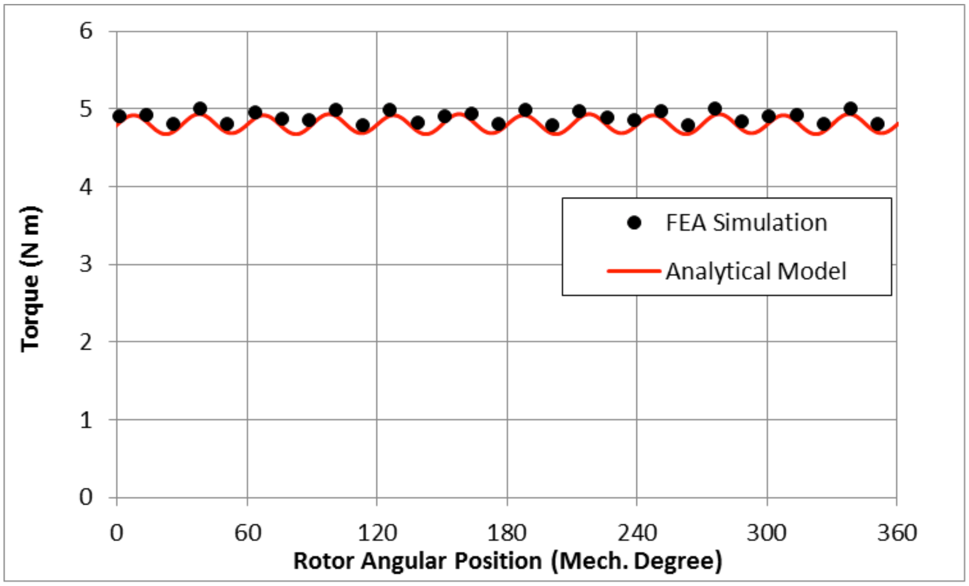

Figure 3-12 Analytical and MotorSolve FEA Predictions of Total Torque

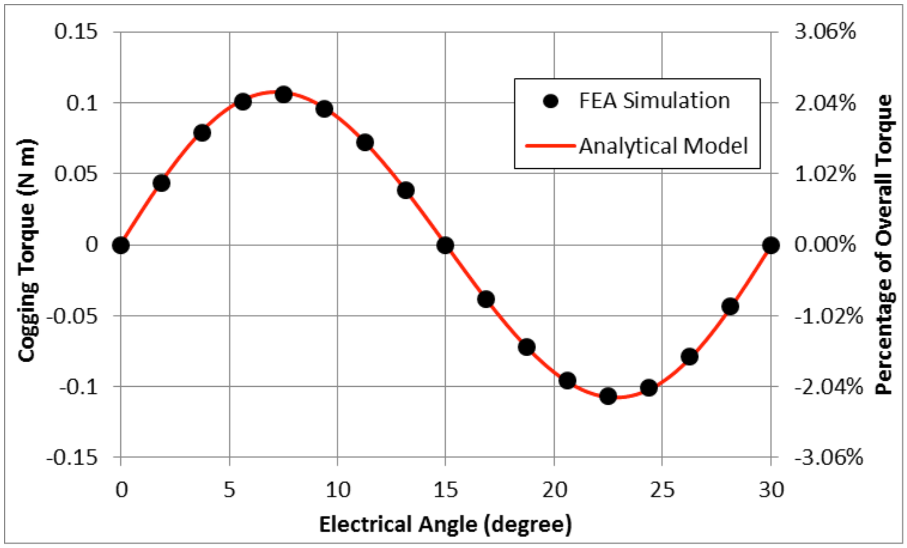

Figure 3-13. Analytical and MotorSolve Predictions of Cogging Torque

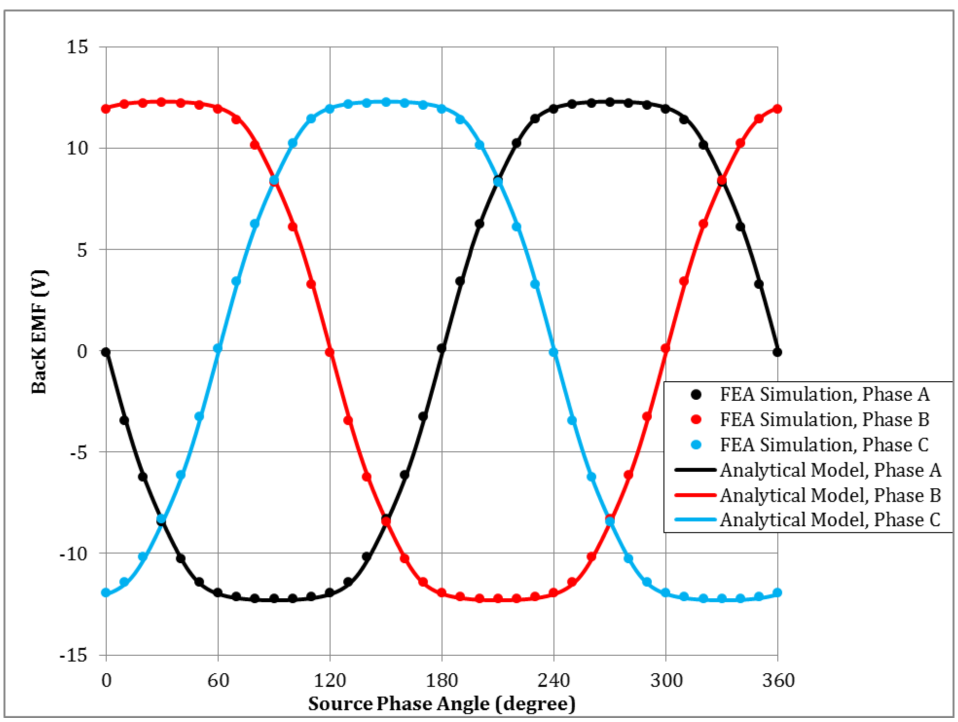

Figure 3-14 Analytical and MotorSolve Predictions of Back EMF

The back-EMF for Halbach Array motor is more sinusoidal than conventional surface-mounted permanent magnet motor. As a result, the Halbach Array machine, as shown in Figure 3-9 (R_{mp}=0.5), provides much lower cogging torque (with a peak magnitude of 0.015 Nm) comparing to conventional motor in Figure 3-13 (with a peak magnitude of 0.11 Nm).

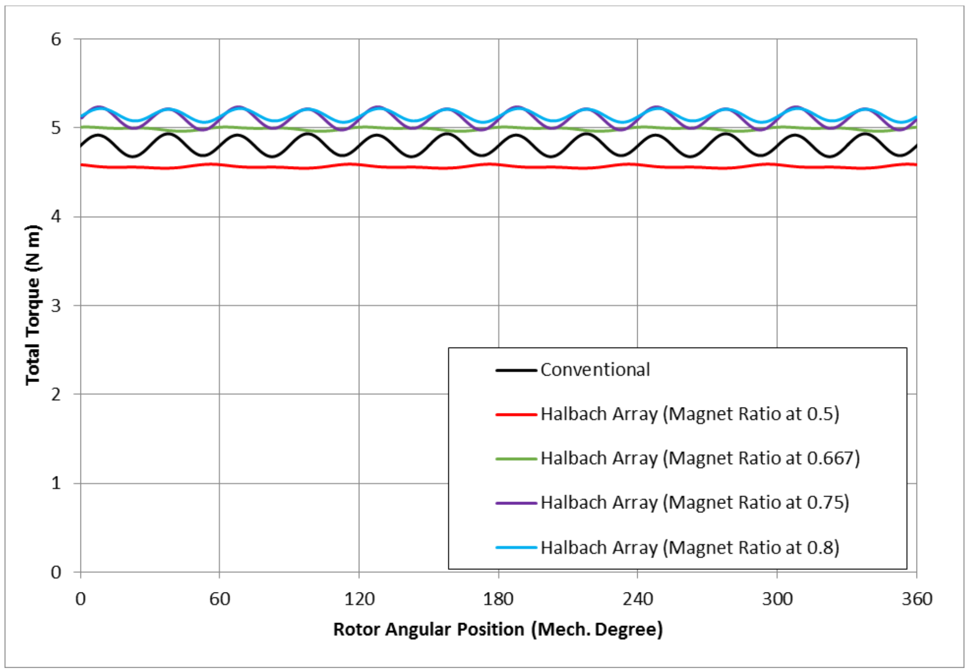

Figure 3-15 Analytical Torque with Different Magnet Ratio Values

Comparison motor torques among the different machine designs is presented in Figure 3-15. Among the magnet ratios of 0.5, 0.667, 0.75, 0.8 and 1, the design for 0.8 provides the highest torque, which is approximately 10% higher than the conventional design (R_{mp}=1) in this particular configuration while it has reached 25% for other cases. Also note that the design with a magnet ratio of 0.5 actually generates 4.5% less torque comparing to the convention magnet configuration. These results demonstrate that the maximization process of electromagnetic torque is nonlinear with respect to the magnet ratio. Only with an appropriate and optimal magnet ratio can the Halbach Array design provide a higher torque compared to the conventional SPM motor given the same size and supply constraints. From such calculations, it suggests that the PM motor output torque is related to the integration of the half cycle of flux linkage for each coil; and the optimal magnet ratio to maximize the torque requires the maximum integration of this flux linkage for each coil, under the same input conditions [58]

$$\frac{\partial \int_{\frac{\pi}{2}}^{\frac{3\pi}{2}} \psi_{coil} \, d\theta}{\partial R_{mp}} = 0. \tag{3-100}$$

3.4 Thermal Analysis

In addition to the electromagnetic modeling, a thermal analysis of the reported 10-pole SPM motor is performed using FEA simulation. Such an analysis is to provide illuminated evaluations for the heat generation and its transfer within the motor embodiment during operation. As a result, the temperature distribution within the motor assembly can be predicted. Overheat spots on copper windings or thermal-sensitive electric components are regarded as constraints to the motor embodiment and will be examined. Unless sufficient heat could be removed from the motor assembly, or limited current magnitude would be allowed for necessary cooling to suffice, over-heat or melting would happen in the motor material and cause malfunction of operation, or even bring about safety issues.

In the present study, the thermal analysis and evaluation are performed under the requirements that the maximum temperature within the motor assembly be lower than 180 ^{0}C (any spots with temperature higher than 180 ^{0}C will be considered as motor over-heat). There are two main sources for the heat generation while a PM motor machine operates, which are often referred as the copper loss and the iron loss. Copper losses are generally the heat losses generated within the copper winding conductor because of its carried electric current, which are proportional to the winding resistance and the square of the current magnitude. Generally, lower current values or winding resistance (e g, shorter total length or fewer numbers of turns in stator) will reduce the heat caused by the copper loss. Also, the limitation of the total motor weight would require less use of copper in windings, which could minimize its cross-sectional area, increase the conductor resistance and therefore increase heating.

For the iron loss, two mechanisms occur, namely eddy current loss and hysteresis loss. The eddy current loss is produced by relative movement between conductors (stator iron core) and magnetic flux lines. The hysteresis loss is due to reversal of magnetization of stator iron core whenever it is subjected to changing magnetic forces. The iron loss depends on variables such as the thickness of the laminations in the stator, the magnitude of the flux density, the stator iron material resistivity, and most importantly, the frequency at which the motor operates. To use a laminated stator and decrease the thickness of the laminations with electrical insulation from each other could reduce the iron loss.

The modeling of the iron loss power P_{iron} per unit volume of the stator material in this study was performed as (2-1). The coefficients here for iron losses are related to the given stator material properties from manufacturers, and the integration of the iron heat loss within the entire stator body is calculated in FE model using above equation performed in the stator teeth and yoke (back iron) domains.

In the present study, Hiperco 50A alloy is used as the motor core material and the stator slot encapsulation material (CW 2710/HW 2711, Huntsman, Woodlands, TX) is used for slot potting and thermal conduction enhancement. Further studies regarding different motor materials can be performed. The temperature distribution of the present SPM motor (10p/12s) is modeled to examine whether overheat occurs with present conditions. Shown in Figure 3-16 (a) is the time-based temperature variation for different motor components, under the operating conditions mentioned in Table 2-1; Figure 3-16 (b) shows the axisymmetric temperature distribution in the 3D motor model, provided by MotorSolve FEA simulation. The ambient temperature for this case study is set to be 40^{o}C. All three heat transfer mechanisms, conduction (within the motor solid assembly), convection (on motor external surface) and radiation (on motor external surface) are considered. In this case shown in Figure 3-16, no overheat is observed under the present operating condition. Taking into account the end winding heat effect, the maximum temperature would occur within the copper windings and their ends, where the copper heat loss is generated and has the longest distance (length of thermal transfer path) to the low-temperature ambient.

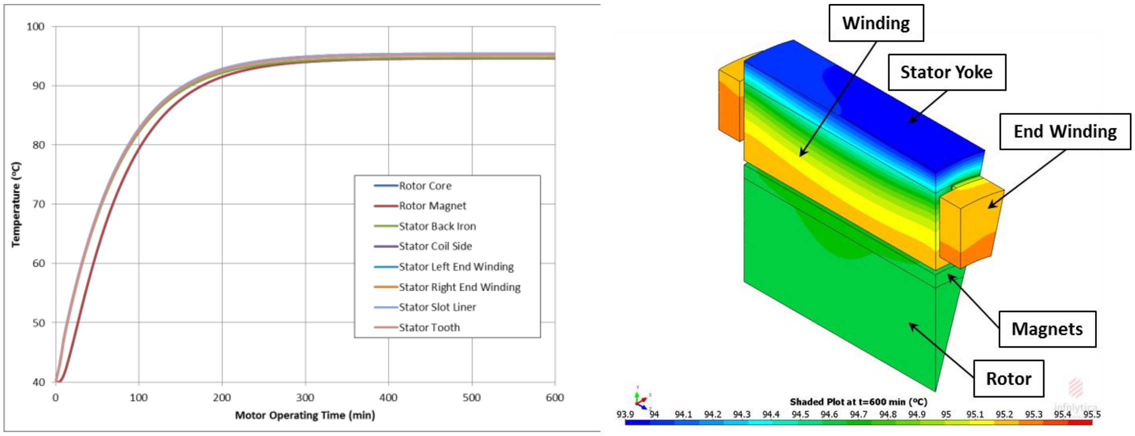

(**a**) (**b**)

Figure 3-16 Motor Thermal Analysis: (a) Time-based Temperature Profiles; (b) Temperature Contours for 3D Thermal Modeling

Although the configuration of Halbach Array magnet and its advantages are reported previously, the torque dense capability of a Halbach Array motor is not widely realized. In the present study, Halbach Array SPM motors are verified to be able to produce higher torque than a conventional SPM with the same magnet volume and at the same rotor speed, provided the optimal Halbach Array magnet ratio, Rmp, is applied. It is also noted that compared to induction motor (IM) machines, the permanent magnet (PM) motors, including SPM and IPM (interior permanent magnet) machines, are able to achieve greater torque/current density, also with higher efficiency and reliability in low speed operation [88]. On the other hand, the general torque production also implies that in these motor categories, lower supply current may be required to retain the same torque performance using the Halbach Array SPM motor compared to others including the standard IM motors. As a result, lower supply current will present lower copper heat loss. Therefore, for industrial applications such as subsea electrical submersible pumps (ESP) or progressive cavity pumps (PCP), which require of driving motors with high torque density at a relative lower speed [89], the Halbach Array SPM motor is a good choice for its ability of high torque dense performance, with lower heat loss and higher efficiency. Such high-torque, low-speed motors could also eliminate the necessity of using a gear-reduction unit to reduce the high rotational speed driven by an IM machine, and reduce its mechanical loss and possible failures.

3.5 Conclusions

Developed in this chapter is a subdomain model accounting for tooth-tip and slot effects for surface mounted permanent magnet (SPM) Halbach Array motor. The proposed analytical model can accurately predict the electromagnetic flux field distributions in motor applications of conventional and Halbach Array SPM machines. Based on the resultant magnetic field, the electromagnetic performances of the motor, such as the cogging torque, back-EMF, and electromagnetic torque are accurately calculated. The finite element (FE) analysis validates the predictions of the proposed analytical model.

Due to the feature of Halbach Array magnet configuration, the magnetic flux field is augmented on one side (outward of rotor), while cancelled on the other side (inward of rotor). In the present study, much less flux saturation is observed in rotor back iron with Halbach Array configuration compared to the conventional ones. Thus in Halbach-Array design, more magnets could be installed in the rotor to achieve higher torque, with lower risk to cause flux saturation within the rotor back iron; on the other hand, less back iron material is needed in the Halbach Array designed rotor.

Also, we conclude that the Halbach Array magnet ratio would be one of the most important design parameters in Halbach Array SPM motors, because it influences on the flux density in both peak value and waveform which will therefore stimulate the resultant torque. With the appropriate magnet ratio in the motor embodiment, the Halbach Array motor is capable to produce higher torque than the conventional SPM motor for the same volume of magnets. Furthermore, potentially lower supply current requirement of the Halbach Array SPM motor would reduce the heat loss and increase the motor operating efficiency. For the industry applications (such as PCP motor) with direct-drive motors operating at low rotor-speed, it suggests that with magnet ratio optimization, the Halbach Array SPM motor is capable to exceed other machines (IM, IPM, or conventional SPM) in both torque performance and efficiency. In the low speed operation, the Halbach Array SPM motor could be able to provide 10-25% more overall torque, with the same motor size and the same input current.

4 DESIGN AND OPTIMIZATION OF HALBACH ARRAY MOTOR FOR ELECTRIC VEHICLES APPLICATION CONSIDERING DRIVE CYCLES

4.1 Introduction, Survey on Electric Vehicle Powertrain

Electric vehicles (EVs) have become more and more prevalent in recent years, as they are considered as the most sustainable solution to help protect the environment and to achieve high energy efficiency for transportation [90]. Our future is heading towards the use of EVs. Optimists, such as Bloomberg New Energy Finance (BNEF) in its 2019 Electric Vehicle Outlook report see the total EVs stock soaring to about 32% of the world's passenger vehicles, 548 million by 2040 [91].

A modern electric drive train is conceptually illustrated in Figure 4-1 The drive train comprises three major subsystems: propulsion system, source of energy, and auxiliary power supply [92]. The electric propulsion subsystem consists of the vehicle controller, power electronic converter, electric motor, mechanical transmission, and driving wheels. The energy source subsystem involves the energy management unit, the energy source, and the energy-refueling unit [93]. The auxiliary subsystem includes the power steering unit, the hotel climate control unit, and the auxiliary supply unit. Traction motors are the key component for propulsion system. To meet the requirements of various driving conditions of frequent acceleration or deceleration, climbing under heavy load and high-speed cruise, traction motors require high torque and power density, high efficiency, wide speed range, high reliability, and low noise.

In EV tractions, Permanent Magnet (PM) motors have been widely used and considered as the most promising candidates in automotive, industrial and servo application [88, 94, 95]. They are designed with different rotor topologies. Whereas rare earth magnets arrangement defines the type of PM motor. Of the family of PM motors, two motor types have been selected due to their major advantages for EVs, first one with interior permanent magnet (IPM) motor and second one with ring magnet on the rotor surface called Surface Permanent Magnet (SPM) motor. PM motors advantages for urban-used cars where frequent start-stops occur at low speeds. Besides, they have a better geometrical integration into engine cabinet and reduce total weight of vehicle [92]. When comparing PM motors with other type of motors (Induction Motor IM…), PM Motors have lower current ratings. Subsequently, lower current rating for inverter improves battery utilization. The use of PM motors also improves battery utilization and driving range thanks to their high efficiency at low speeds. Moreover, the introduction of high-energy-density PM has made it possible to achieve very high-flux densities in motors. This accordingly makes it possible to achieve high torques, which in turn allows one to make the motor small and light. Many cars adopted PM motors, such as Nissan Leaf and Toyota Prius.

Some EVs adopt propulsion solutions without PM, such as Tesla Model S, which uses copper rotor induction motors (IMs). However, the starting current of IMs can be high and this is disadvantageous for battery duration IM have simple structure, less maintenance requirement, reliability, robustness, low cost and operation at poor environmental conditions [96]. The torque and field control can be divided by vector control methods. Speed range may be extended by flux weakening in the constant power region. IM has negative features such as low efficiency compared with PM, high loss and low power factor. To overcome these problems, dual inverters are used for the purpose of extending constant power, and rotor losses are reduced in design stage [97, 98]. If compared with DC motor drives, AC motor drives have some advantages such as higher efficiency, less maintenance need, robustness, reliability, higher power density, effective regenerative braking. Presented in this manuscript is the application of new magnet arrangement called Halbach Array (HA) [99] adopting SPM configuration for EVs.

The HA magnetization was originally revealed in the 1970's and replicated by Klaus Halbach in the mid 1980s [18]. This new magnetic array arrangement oriented the magnet poles such that the flux is magnified in a specific direction while limiting the flux in the opposite direction. Despite concentrating the magnetic flux is a desired direction; a Halbach Array may not necessarily improvement torque density. In fact, it is possible to create an adverse effect on torque density if the overall design is not chosen appropriately [99]. For that reason and the associated manufacturing costs, Halbach Arrays have not found a niche in electric motor applications. An integrated Halbach-magnetic-geared PM motor was proposed in [100], in which an outer-rotor PM motor is artfully integrated into a coaxial magnetic gear. On the other hand, an investigation was held on motor driver with HA magnetization for urban electric vehicle [101], where they tried to reduce the iron and copper losses in no-load condition to extend the urban vehicle drive range.

Several researches have been carried out in the design and optimization of synchronous motor for traction application including all the main typologies such as SPM [102], IPM [103-105], IM [106, 107] and Switched Reluctance Motors (SRM)

[108-111]. In these researches, the design and optimization procedure is based upon rated motor specifications and they do not consider the actual working cycle of the electric car. In order to investigate the effect of driving conditions on design of traction motors, some established driving cycles could be employed to test the EV. An optimization design for PM assisted reluctance motor was presented in [112, 113] given the torque profiles of a selected driving cycles.

The reduction of level of the harmonics of the excitation flux created by the HA permanent magnets decreases iron losses in the synchronous motor core [101]. Additionally, increasing the amplitude of the fundamental component of the electromotive force and the fundamental harmonic, while reducing the harmonics of higher rank, is possible with a HA magnetization in the rotor [99, 114]. As a result, this will lead to lower copper losses and lower iron losses due to the absence of higher harmonics in the stator core. Reduction of the losses is of particular high interest for traction applications where a vehicle operates at variable speed.

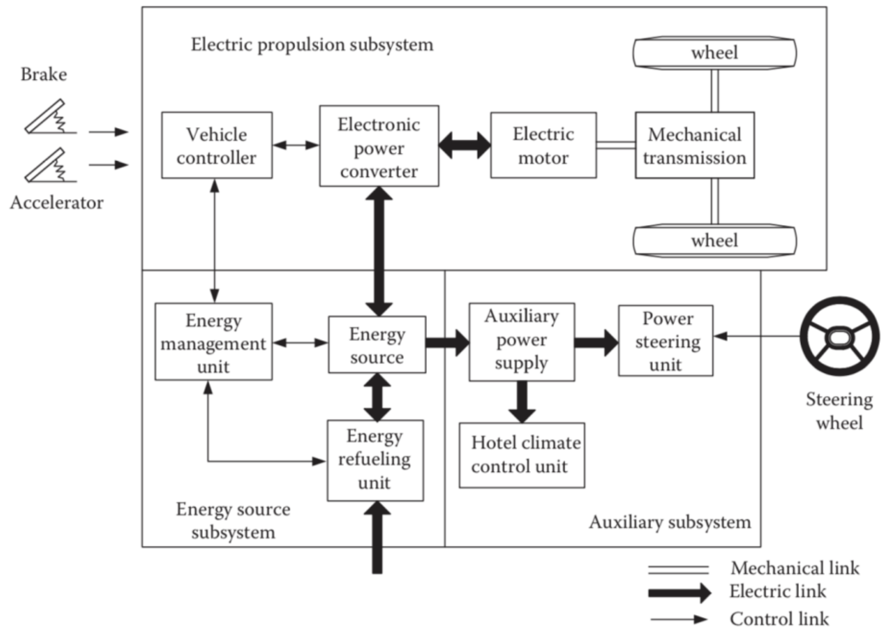

Figure 4-1 Conceptual illustration of general EV Configuration [92]

This chapter describes design techniques for HA motor and compares the optimized design with the IPM used in Nissan Leaf 2012 model that are based on two standard driving cycles: the Urban Dynamometer Driving Schedule (UDDS) and US06 Supplemental Federal Test Procedure (SFTP) [115]. These driving cycles are adopted to carefully test the traction motor performance in terms of torque, efficiency, and thermal condition, while satisfying the required torque–speed requirements. The torque–speed envelope is derived under the power limit that the Nissan Leaf inverter can supply which is 80 kW. To check the temperature of the windings and magnets under various driving conditions, Thermal analysis is performed. Based on the analytical design presented in [99], the torque is estimated to calculate current and losses in the HA traction motor. Accordingly, The benefits and the disadvantages of the HA motor for EV tractions can be fully elaborated. Some suggestions regarding the design of EV traction motors are provided.

4.2 System Overview

EV motor and inverter should be developed appropriately involving optimization of the relationship between current and torque/power output. Besides, reduction gear should be integrated with the motor to achieve the desired torque and maximum speed needed by the specific drive cycles. In this part, problem descriptions and assumptions are presented. Then, the Nissan Leaf motor specifications are summarized.

4.2.1 Problem Descriptions and Assumptions

The EV motor has to overcome various driving conditions and road load, which are established by roadway gradient, rolling resistance, the vehicle mass and aerodynamic drag coefficient. The motor is required to have a high starting torque for initial acceleration, high power density and high efficiency to extend the battery range. In addition, a wide operating speed range facilitates single gear transmission to maximize the whole powertrain efficiency. The EV's motor torque-speed profile is composed of three regions; constant torque, constant power and natural characteristics regions [116]. The torque is constant up to the base speed of the motor when the constant power region is reached. In the constant power region, the motor operates beyond the base speed thanks to the field weakening and it is characterized by constant power and decreasing torque. The motor fails to maintain the rated power beyond this region and the speed drops according to the natural characteristics of the motor. That's the maximum speed of the motor. Extending the constant power region of the motor will minimize the motor power for EV application [117]. A high torque and good efficiency in the field-weakening region (constant power region) are of tremendous importance in EVs.

In the following, HA motor is designed and optimized to overcome the driving performances of Nissan Leaf 2012 IPM. To have a fair comparison between the two motors, there are no changes on the number of poles and slots. The HA motor has a two-segmented HA with non-overlapping windings. The 2-D mathematical model developed in [99] is based on the following assumptions: (1) infinite permeable iron materials, (2) negligible end effect, (3) linear demagnetization characteristic and full magnetization in the direction of magnetization, (4) non-conductive stator/rotor laminations, and (5) the gaps between magnets have the same constant relative permeability as magnets [76].

4.2.2 Nissan Leaf Motor Design Specifications

The Nissan Leaf 2012 motor is an IPM with 8 poles and 48 slots [118]. Figure 4-2 shows the cross-sectional view of the Nissan IPM motor with an overlapping winding layout. Compact in size, it delivers high power and efficiency to support the quick response characteristic of EVs. The motor efficiency map in Figure 4-3 is published in [118] and verified in Figure 4-4 by the Oak Ridge National Laboratory (ORNL) under 80kW, DC-link voltage 375V and 65C Water-Ethylene Glycol temperature [119]. From the published data about the Nissan Leaf motor [118-120], a Motor-Cad model is built and the generated efficiency map Figure 4-5 validated with both efficiency maps cited in [118] and [119]. The geometric parameters are presented in Table **4-1**.

Table 4-1 Nissan Leaf 2012 motor geometric parameters

Parameters	Value
Number of Poles/Slots	8/48
Stator Outer Diameter	198.12 mm
Motor Length	260 mm
Rotor Outer Diameter	130 mm
Stator Bore	132 mm
Air Gap	1 mm
Tooth Tip Depth	1.2 mm
Slot Depth	21.1 mm
Slot Opening	2.7 mm
Number of strands in hand	20
Turns	6
Reduction Ratio	7.9377

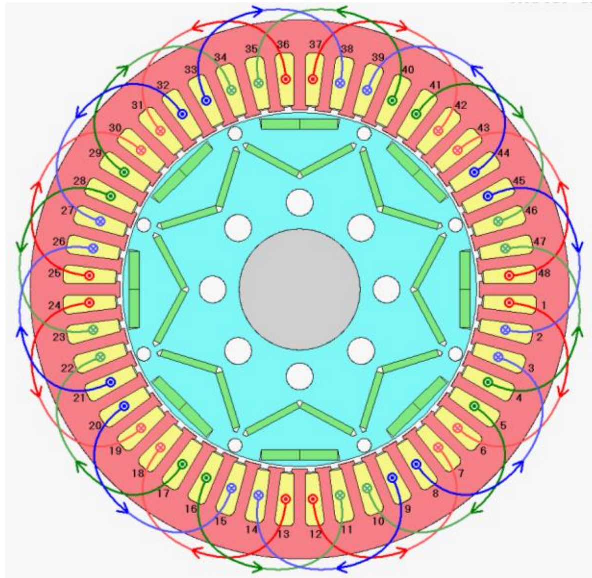

Figure 4-2 Cross-sectional view of Nissan Leaf 2012 IPM and winding layout

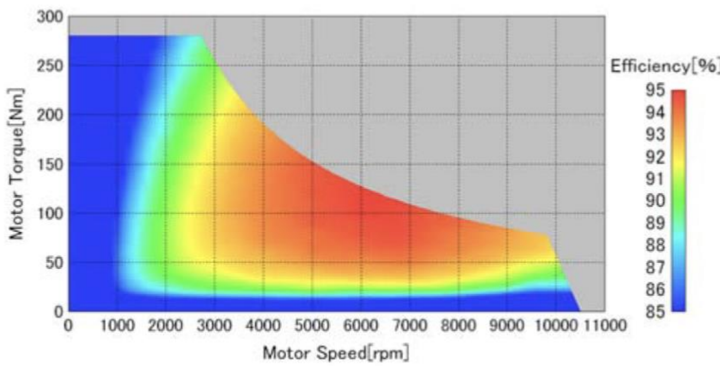

Figure 4-3 Nissan Leaf Published Efficiency of the Electric Motor

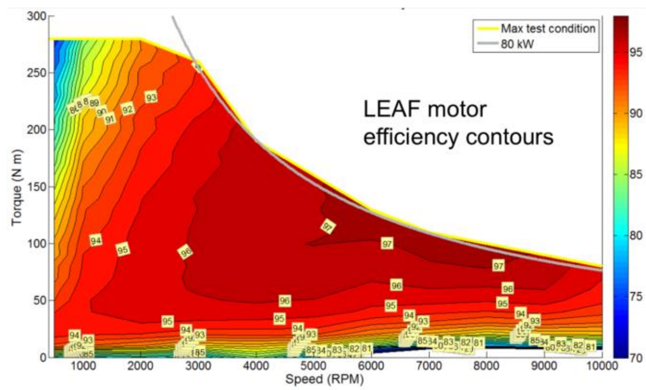

Figure 4-4 Nissan Leaf Measured Efficiency of the Electric Motor

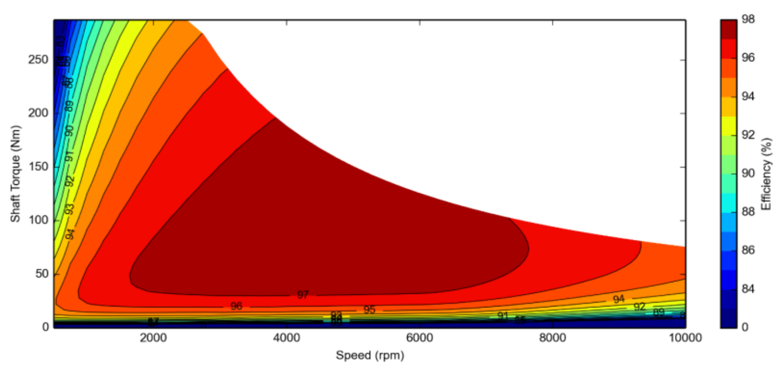

Figure 4-5 Nissan Leaf Modeled Efficiency of the Electric Motor

The basic structure of Nissan IPM adopts a water-cooling system to facilitate high continuous power output and uses a resolver as the rotary position sensor ensuring high response. The IPM motor is combined with a three-parallel-shaft gear reducer with a reduction ratio stated in Table **4-1**. The electromagnetic simulation is presented in Figure 4-6 showing the flux lines in one pole region.

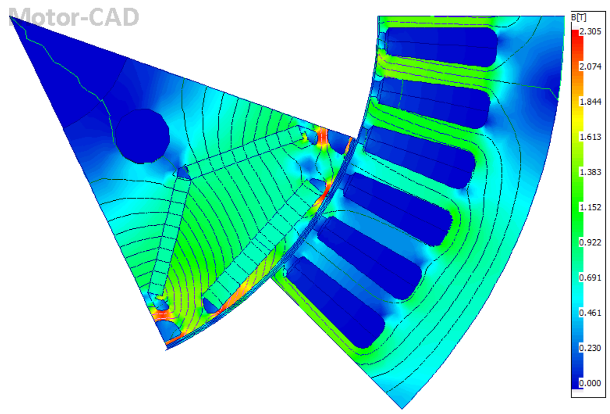

Figure 4-6 One Pole Electromagnetic Flux Lines

4.3 Design Optimization of Surface Mounted Halbach Array Motor to UDDS and SFTP Driving Cycles

In this section, HA motor and EV specifications are presented along with design optimization constraints. Afterwards, multi-objective driving cycles optimization is developed. Finally, design outcomes are evaluated and compared with the commercial Nissan Leaf motor 2012.

4.3.1 Motor and Vehicle Specifications and Optimization Constraints

The Nissan Leaf grants a driving range of around 160 km at UDDS driving cycle with a top speed of 140 km/h. It is a city car with the capability to operate in suburban area. The basic specifications and properties for Nissan Leaf are presented in Table **4-2**. The drive train works with one motor coupled to the front axles via differential. The differential gear ratio of 7.93 is quite high, in order to reduce the motor torque demand, resulting in lower motor size. However, this selection in differential gear ratio will increase the need for a wide operating motor speed range, in order to achieve the maximum vehicle speed. At this point, the optimized HA motor will need a smaller gear ratio having higher torque and lower current needs. Resulting a significant decrease of power losses especially in copper losses. The motor's torque demand and operating speed over UDDS and SFTP are specified via fundamental analytical vehicle loading equations, regarding the acceleration, the grading resistance forces and the rolling resistance [111]. The EV parameters are kept unchanged during the optimization process for HA motor except for the gear ratio. Conversely, we are substituting the IPM motor with HA motor adapting the gear ratio to reach the torque and speed requirements. Therefore, the gear ratio is optimized accordingly to fulfill the same maximum speed as the Nissan leaf vehicle.

Table 4-2 Nissan Leaf vehicle specification [119]

Mass	1521 kg
Rolling Resistance Coefficient	0.007
Air Density	1.225 kg/m^3
Frontal Area	2.29 m^2
Drag Coefficient	0.28
Final Drive Ratio	7.938
Wheel Radius	0.3 m
Mass Correction Factor	1.04

Motor speed and shaft torque over the SFTP and UDDS driving cycles are illustrated in Figure 4-7 and Figure 4-8 respectively with 7.93 gear ratio. US06/SFTP was developed to address the representation of aggressive, high speed and/or high acceleration driving behavior, rapid speed fluctuations, and driving behavior following startup [115, 121]. Whereas, UDDS simulates an urban route of 7.5 mi with frequent stops. The maximum speed is 56.7 mph and the average speed is 19.6 mph [121].

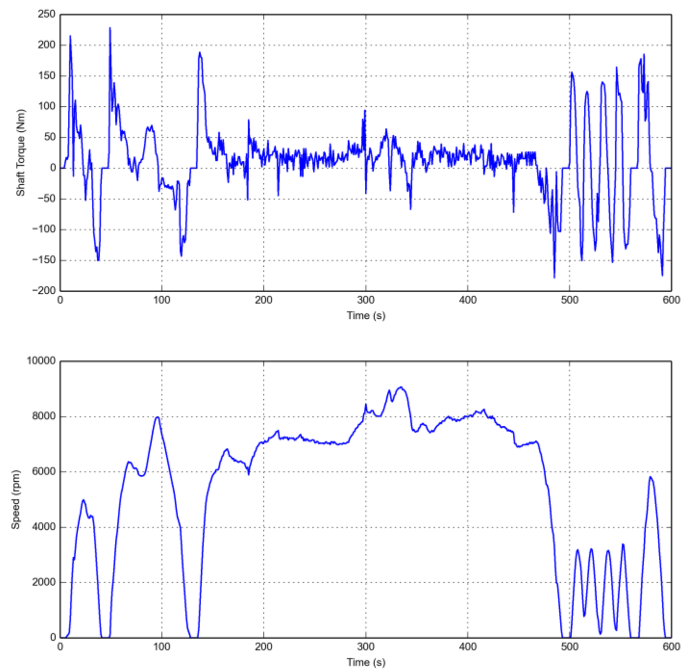

Figure 4-7 Motor speed and shaft torque over SFTP driving cycle

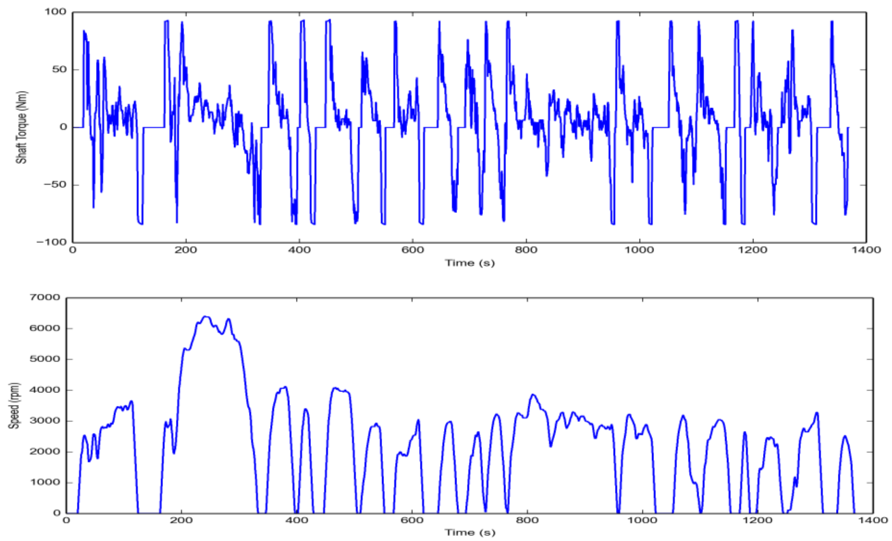

Figure 4-8 Motor speed and shaft torque over UDDS driving cycle

4.3.2 Multi-Objective Halbach Array Optimization and Evaluation

A 48-slots, 8-pole HA motor, equipped with slot overlapping winding, described in Figure 4-9, has been considered in this design analysis. It shares the same stator geometry of a Nissan Leaf motor. The rotor is symmetric and it is equipped with 3 magnets per pole, each magnet has its own magnetization to form HA magnetization with an active region in the air gap.

The design optimization process is based on parameters defined in Table **4-1** achieving minimum energy loss over the UDDS and SFTP. HA motor should be maintained at high efficiency for the widest possible speed range. This may be achieved by employing the torque per copper loss (TCL) over the selected driving cycles. From the needs of EVs on electric motors, in this paper, two criterions are projected to evaluate the design of HA motors in EVs. They are the electromagnetic torque referring to (4-1), the TCL represented in (4-3). The analytical model HA motor is based on the HA subdomain model developed in [99] where the torque is calculated based on power input and design parameters.

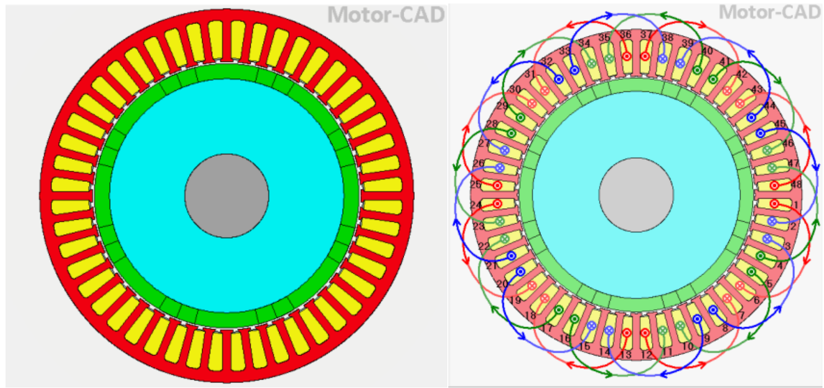

Figure 4-9 Cross-sectional view of HA motor and winding layout

$$T_{em} = \left(E_a I_a + E_b I_b + E_c I_c\right) / \omega, \tag{4-1}$$

where E_a, E_b and E_c are the three-phase back-EMF vector components, ω is the speed and I_a, I_b and I_c are the three-phase current vector components.

Hereafter, the copper loss is computed as

$$P_{copper} = R_{ph} I_r^2, \tag{4-2}$$

where R_{ph} represents the phase resistance and I_r is the rated current driving the motor. Hence, the TCL over a driving cycle is expressed as

$$TCL = \int_{UDDS+SFTP} \frac{T_{em}}{P_{copper}}. \tag{4-3}$$

The two criterions are selected as the two design objectives of HA motor in this paper. Obviously, it is challenging to simultaneously maximize these objectives. Therefore, the appropriate compromise between the maximum torque and maximum torque per copper loss, is defined as the optimization function [122], which is stated as

$$\max\left\{w_t \frac{T_{em}}{T_{emb}} + w_{tcl} \frac{TCL}{TCL_b}\right\}, \tag{4-4}$$

$$T_{emb} = \max\left\{T_{em}\right\}, \tag{4-5}$$

$$TCL_b = \max\left\{TCL\right\} \tag{4-6}$$

$$\text{and } w_t + w_{tcl} = 1, \tag{4-7}$$

where ω_t and ω_{tcl} are the weight factors of the electromagnetic torque and the torque per copper loss, respectively, T_{emb} represents the base value of the electromagnetic torque, TCL_b represents the base value of the torque per copper loss. The base value of the electromagnetic torque is calculated by maximizing the defined parameters when maximizing the electromagnetic torque. Similarly, the base value of the torque per copper loss is computed by optimizing the defined parameters when maximizing the torque per copper loss.

Referring to (4-4), the optimization with two objectives has been reduced to one objective function by using two weight factors and two base values. The maximum value of the optimization objective function is unity. Selecting various weight factors designate the shares, which are taken up by the electromagnetic torque and torque per copper loss in the optimization function. Consequently, if one of the two objectives is desired to be emphasized, its weight factor may be chosen larger value than the other factor.

The block diagram in Figure 4-10 demonstrates the algorithm of the proposed Analysis Led Design (ALD) process. At first, the design parameters are optimized to maximize individually the two objective functions, which are the electromagnetic torque and the torque per copper loss. Subsequently, the base values of the electromagnetic torque and the torque per copper loss are calculated. Then, the weight factors are selected and the multi-objective optimization function is established. Finally, the design parameters are optimized to maximize the multi-objective function. It has to be noted that this process is implemented using analytical model for HA motor and MotoCad model.

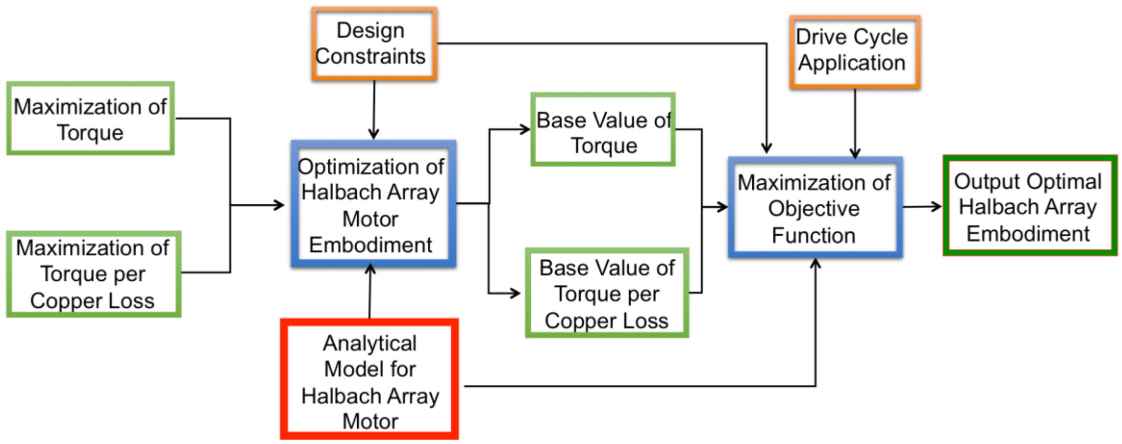

Figure 4-10 Analysis Led design process diagram

Table 4-3 Optimization parameters range of variation

Parameters	**Range (mm)**
Rotor OD	120-150
Air Gap	1-2
Slot Opening	2.5-3.5
Tooth Width	3.5-5.5
Tooth Tip	1-1.4
Magnet Thickness	11-20
Stator Yoke	10-12
Magnet Ratio	0.6-1
Number of Turns	80-180
Wire Slot Fill	63% **Fixed**

The geometrical design parameters are presented in Table **4-3** as the optimized parameters along with the range of variations. Taking into account the constraints from the Nissan Leaf IPM motor, the analytical model is employed in genetic algorithm to optimize multiple analysis designs. Genetic algorithms are search techniques that use ideas from the biological process of evolution. By virtue of natural selection, genetic algorithms can be used as robust numerical optimizers on problems that would normally be tremendously challenging due to complex search spaces. The genetic algorithm has an advantage in that it is a global optimization strategy, as opposed to more conventional methods, which will often stop at local maxima.

The selected torque weight factors are 0, 0.3, 0.4, 0.5 and 1. Adopting this selection, we are calculating the base values for torque and for TCL over the drive cycles at first with 0 and 1 values. Table **4-4** represents the optimized embodiment for base values where the objective function includes only the torque or TCL over drive cycles. It has to be noted that these parameters are presented in the analytical subdomain model developed in Figure 4-11 [99], where the HA magnet ratio is expressed as follows:

$$R_{mp} = \frac{b_r}{b_m}, \tag{4-8}$$

where pole arc β_r to pole pitch of a single pole β_m.

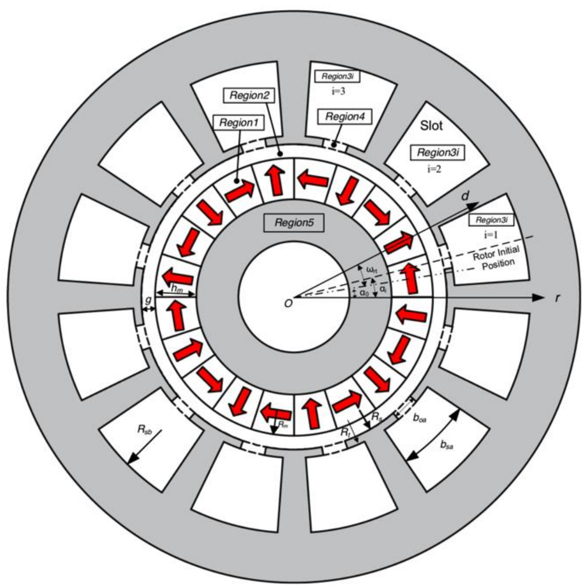

Figure 4-11 Symbols and Regions of Subdomain Model with Tooth-tips

Table 4-4 Optimized Configuration for Base Torque and base TCL Designs

Parameters	Base Torque Results	Base TCL Results
Rotor OD (mm)	138.1	145
Air Gap (mm)	1	1
Slot Opening (mm)	2.5	3.5
Tooth Width (mm)	5	3.5
Tooth Tip (mm)	1	1
Magnet Thickness (mm)	20	20
Stator Yoke (mm)	13.45	10
Magnet Ratio	0.702	0.7
Total Number of Turns (Number of strands in hand x Turns)	120 (6x20)	94 (4x16)
Torque (Nm)	437.46	249.28
Torque Per Copper Loss (Nm/Wh)	3.41	8.595

Figure 4-12 shows the values of two criterions at different combinations of torque weight factors. It can be seen that at 0.5 weight factor the torque increase to reach a level of 422 Nm and the TCL decrease to around 5.5 Nm/Wh over the average of the two-drive cycle (UDDS and SFTP). This analysis results the best design that means high torque, low copper loss and high torque density regarding the fixed volume condition.

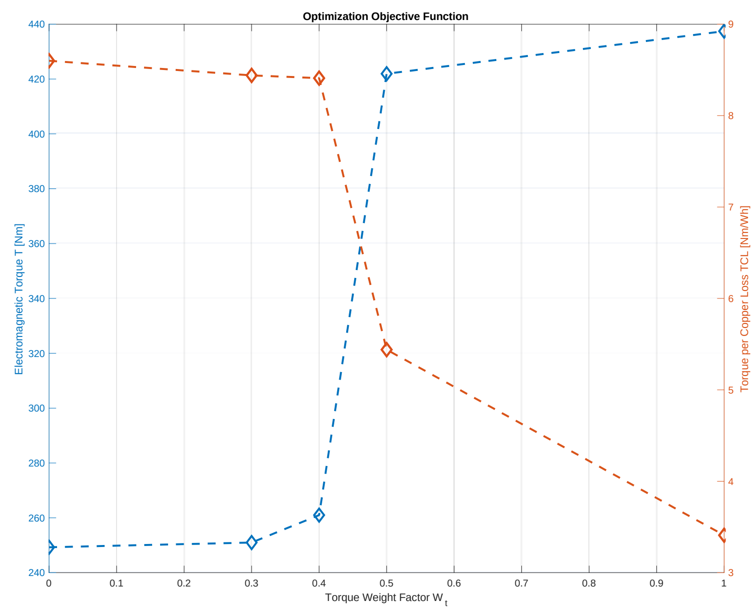

Figure 4-12 Torque and TCL pattern varying weight factor

In order to make a fair comparison between the Nissan IPM and optimized HA motors, the average efficiency over drive cycles, electrical input energy, recovered electrical output energy, shaft generating energy and total loss are presented in Table **4-5**. The average shaft motoring energy is 2207.11Wh. As shown, the lowest total loss is generated by TCL base design. Consequently, the highest average efficiency over drive cycle is about 96.72% for TCL base design. Besides, when the EV is braking, the EV machine operates as a generator, whose torque is negative and speed is positive to realize energy recovery. In fact, the recovered electric output energy for the TCL base design generates the highest amount energy. The developed analytical method to optimize EV motors provides higher efficiency than the Nissan Leaf IPM motor.

Table 4-5 Motor designs performance summary over drive cycles

	Nissan Leaf IPM	Base Torque (W_T=1)	Base TCL (W_T=0)	HA Design 1 (W_T=0.3)	HA Design 2 (W_T=0.4)	HA Design 3 (W_T=0.5)
Average Efficiency over Drive Cycle (%)	94.95	94.91	96.72	96.68	96.7	95.8
Electrical Input Energy (Wh)	2329.34	2313.93	2279.83	2281	2278	2307.11
Shaft Motoring Energy (Wh)	2207.11	2207.11	2207.11	2207.11	2207.11	2207.11
Electrical Output (recovered) Energy (Wh)	717.49	705.01	752.35	725.57	722.16	701.69
Shaft Generating	750.77	754.29	752.35	752.48	750.7	752.03

Energy (Wh)						
Total Loss (Wh)	155.51	156.1	99.57	100.8	100.6	121.04

It can be seen that the third design, having a torque weight factor equal 0.5, have 21% less total loss compared to the Nissan Leaf IPM. In addition, it provides 50% more torque than the Nissan IPM. Whereas, the maximum motor speed is half of the Nissan motor. Hence, the gear ratio is optimized accordingly to fulfill the torque and speed requirements of the selected design case. The efficiency map of the third design is presented in Figure 4-13.

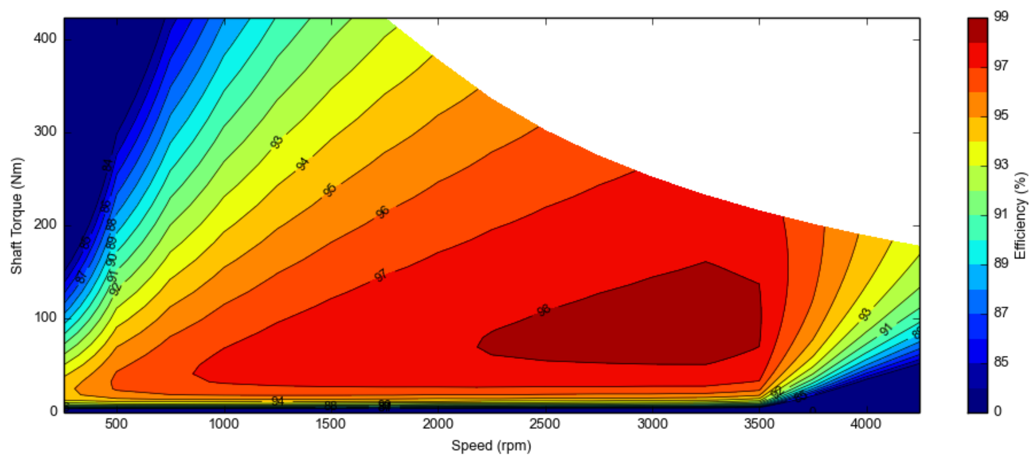

Figure 4-13 HA Motor Design 3 Efficiency Map

4.4 Conclusions

In this Chapter, a new design and optimization method is proposed for HA machines to fulfill requirements of the multiple driving conditions in EVs via ALD. It has been shown that the proposed HA motor satisfies requirements of the multiple driving conditions in EVs. It has been presented that the proposed design method considering the maximum operating speed and performances specifications.

HA configuration has a major benefit in decreasing iron loss and copper loss while increasing electromagnetic performances. Reduction of the losses provides then higher efficiency over wider speed range. This was proven by the increase of average efficiency over drive cycles.

5 MODELING AND OPTIMIZATION OF HALBACH ARRAY MAGNETIC LINEAR SCREW

5.1 Introduction

Linear motion devices such as tubular linear actuators are used in a wide range of applications that demand high force density, high precision and high-speed actuation [123, 124]. A unique linear motion device is a tubular permanent magnet linear machine employing magnetic coupling to achieve rotary to linear motion transmission. An emerging technology is introduced via the MLS, which represents the magnetic counterpart of the mechanical lead screw. Compared to the mechanical ones, the advantage of a MLS is the capability to produce high-density forces without the need of any mechanical intermediate mechanism.

MLSs have been considered attractive since they improve the performance and the reliability of the system. This is achieved by avoiding the problems associated with the fatigue loading and by reducing the losses resulting from the mechanical friction as well as the nonexistence of end-turn effects [125]. Hence, researchers have been able to properly describe these systems and they started proposing a variety of magnetic lead screw embodiments to realize the performance potential for a wide range of applications.

The first design of a trans-rotary magnetic device was proposed in [126]; it employs a magnetic spur gear as a measuring device for the liquid level in a tank. It uses permanent magnets to convert a translational movement into a rotation. This was the basis for later publications, in which new designs of a rotation to translation motion converter have been proposed [127-129]. The basic idea was to achieve a trans-rotary motion conversion by using helical shaped permanent magnets mounted on both the rotor and the translator parts. The proposal in [130] was a model for a linear electromagnetic actuator providing a high density force. Their design was based on a magnetic screw-nut concept involving helical shaped radially magnetized permanent magnets mounted on both parts. An analytical analysis was provided for the magnetic force and torque generated. The results were validated using a numerical analysis. The proposed design was shown to achieve high force densities on the order of 10 MN/m^3. Another MLS was presented in [131]. The authors proposed an overall design of a 500 kN force for wave energy conversion application. They based their design on an embedded-magnet topology instead of a surface mounted structure. The resulting magnetic fields as well as the thrust force were analyzed using finite-element analysis and validated using a scaled 17 kN MLS experimental prototype.

Many applications require a high-density force actuation leading to new MLS embodiments. These new designs have been based on a Halbach Array structure instead of radially magnetized permanent magnets [18, 19, 52]. In fact, the fundamental field of Halbach Array is stronger than that of a conventional magnetization. Moreover, the power efficiency of the motor with Halbach Array is higher. The magnetic field of Halbach Array is more purely sinusoidal than that of the others, resulting in a simple control structure [99]. One such design was proposed in [132] where the author adopted a Halbach Array disposed helically to create a high force density linear actuator to be used in an artificial heart. The permanent magnets were mounted on both parts of the magnetic lead screw. A comparison of the electromagnetic performances of both the Halbach Array and the radially magnetized magnetic screw was presented and a numerical validation was performed to verify the results. A separate MLS design was introduced in [133] based on quasi-Halbach Arrays to develop a trans-rotary magnetic gear. It was stated that a quasi-Halbach Array structure provides a significant force advantage over radial magnetization. The proposed MLS embodiment was analyzed using finite elements and verified through a comparison with experimental data gathered from a quasi Halbach magnetization prototype.

Presented herein is a MLS employing a double-sided Halbach Array. This chapter starts by describing the structure of the proposed MLS. Next, a detailed analytical model was developed to assess the electromagnetic performances of the designed MLS by applying the scalar potential and the equivalent surface-distributed current method to calculate the generated magnetic flux and thrust force. Then, a model validation is presented based on FEA. This section concludes by an example of a practical application of the newly developed model and a summary of these work findings.

5.2 Model Structure and Analytics

In this section, a description of the proposed MLS structure is highlighted along with the different assumptions considered. A detailed analytical model of the presented MLS design is developed and used to compute both the magnetic flux and the thrust force generated during the motion conversion process.

5.2.1 Model Structure

Shown in Figure 5-1 is the proposed MLS concept consisting of two magnetic parts: screw and nut; both the nut and the screw have helically surface mounted permanent magnets [132]. The permanent magnets are arranged to form a Halbach Array configuration. The main advantage of Halbach magnetization is to enhance the magnetic fields interaction between the screw and the nut in the air gap region. A Halbach Array is mainly comprised of four magnetic segments with the respective magnetization rotated 90 degrees about a vector tangent to the screw within an axial lead length of λ Figure 5-2**Error! Reference source not found.**. This arrangement of permanent magnets will create a concentrated magnetic flux on one side of the array (active surface) over the other (passive surface) [99]. Adopting a Halbach Array in the design will offer a higher operational performance of the MLS converting a low speed rotational motion from the nut to a high magnetic force density at the screw part without the need of a mechanical contact [134]. Both Halbach Array and MLS geometric properties will be presented in the next section when deriving the analytical model.

The focus of this part is to develop an analytical approach to model MLS. In fact, we aim to present an accurate prediction of the generated magnetic thrust force given a variety of design parameters such as material properties, permanent magnets (PM) grade and geometric embodiment of the MLS. The analytical model will then be integrated with an optimization routine to optimize the MLS by minimizing the permanent magnets volume subject to a constrained thrust force given within a specific interval.

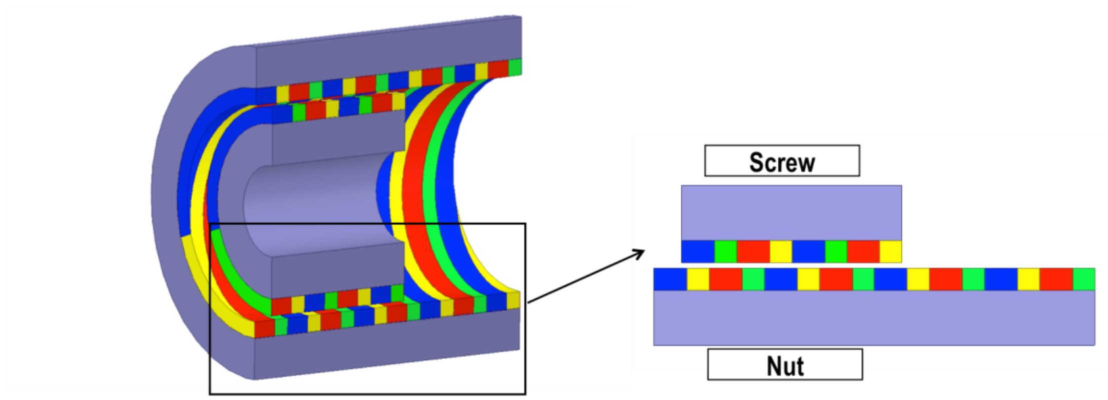

Figure 5-1 MLS Components and Configuration

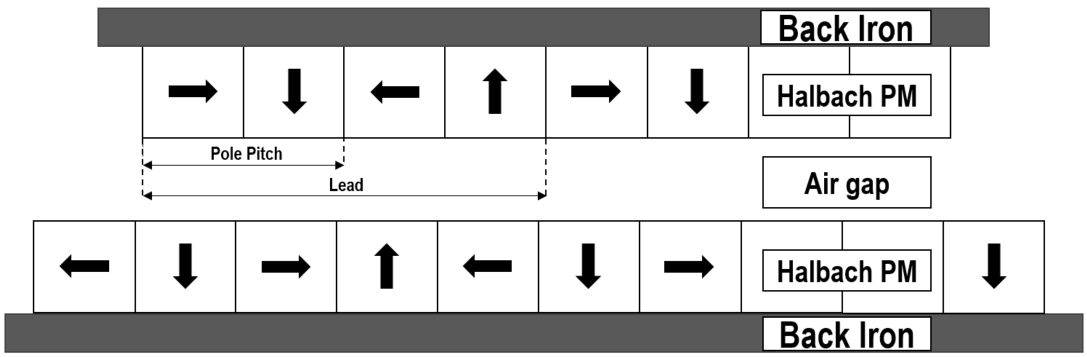

Figure 5-2 MLS Regions

5.2.2 Analytical Modeling

By deploying helical magnets on the external surface of the screw and the internal surface of the nut, the magnetic field distribution in the air gap region of the MLS will be three-dimensional. Though, if the pole pitch is much greater than the air gap width, the field distribution can be approximated as axially symmetric. Consequently, without loss of generality, an axially symmetric geometry shown in Figure 5-2 can be adopted for calculating the magnetic field distribution and the generated thrust force.

Based on electromagnetic theory, the magnetic field of permanent magnet can be described as the magnetic field produced by both region-distributed current and surface distributed current [135, 136]. In the interface between magnets and air, the surface distributed current density can be presented as shown in Figure 5-3. The angle between the magnetization vector M and the radial direction is α. Then the magnetization vector M can be expressed as

$$\overrightarrow{M} = M\cos\alpha\vec{z} + M\sin\alpha\vec{r}. \tag{5-1}$$

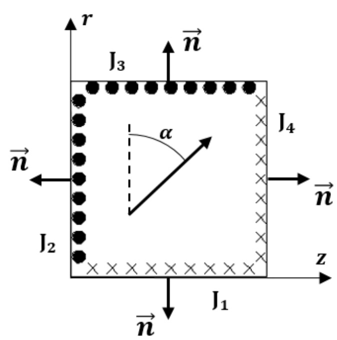

Figure 5-3 Surface Distributed Current Model

The mathematical expressions of the surface distributed current vectors are

$$\begin{aligned}
\overrightarrow{J_1} &= \left(\overrightarrow{M} - \overrightarrow{M_{air}}\right)\times\vec{n} = \overrightarrow{M}\times\left(-\vec{r}\right) = -M\cos\alpha\cdot\vec{\theta} \\
\overrightarrow{J_2} &= \left(\overrightarrow{M} - \overrightarrow{M_{air}}\right)\times\vec{n} = \overrightarrow{M}\times\left(-\vec{z}\right) = M\sin\alpha\cdot\vec{\theta} \\
\overrightarrow{J_3} &= \left(\overrightarrow{M} - \overrightarrow{M_{air}}\right)\times\vec{n} = \overrightarrow{M}\times\left(\vec{r}\right) = M\cos\alpha\cdot\vec{\theta} \\
\overrightarrow{J_4} &= \left(\overrightarrow{M} - \overrightarrow{M_{air}}\right)\times\vec{n} = \overrightarrow{M}\times\left(\vec{r}\right) = -M\sin\alpha\cdot\vec{\theta}
\end{aligned}\ . \tag{5-2}$$

For the Halbach Array case, the magnetization vector is rotated by 90° which means α is equal to {0, 90, 180, 270} degrees. Thus, the distributions of magnetization components M_r and M_z can be expressed using the Fourier series representation

$$M_z = \sum_{k=1,3,5}^{\infty} \frac{4B_r}{\mu_0 k\pi} A_{zk} \sin\left(\frac{k\pi}{\tau} z\right)$$
$$M_r = \sum_{k=1,3,5}^{\infty} \frac{4B_r}{\mu_0 k\pi} A_{rk} \cos\left(\frac{k\pi}{\tau} z\right), \tag{5-3}$$

where

$$A_{zk} = \sin\left(\frac{k\pi}{2}\right)\sin\left(\frac{k\pi\left(1 - M_R\right)}{2}\right),$$
$$A_{rk} = \sin\left(\frac{k\pi}{2} M_R\right), \tag{5-4}$$

and M_R is the ratio of the axial direction length τ_r of the radial direction magnetized permanent magnet (shown in Figure 5-5) to a pole length τ.

$$M_R = \frac{\tau_r}{\tau}. \tag{5-5}$$

While the MLS is composed of magnetic screw and magnetic nut, the magnets in the nut are considered as surface distributed current. Hence, the nut will be considered as a slotless stator composed of a sequence of rotating rectangular coils, having surface current distribution to form the magnetization of each permanent magnet as shown in Figure 5-4. This assumption is adopted in order to simplify the electromagnetic modeling and thrust force calculation.

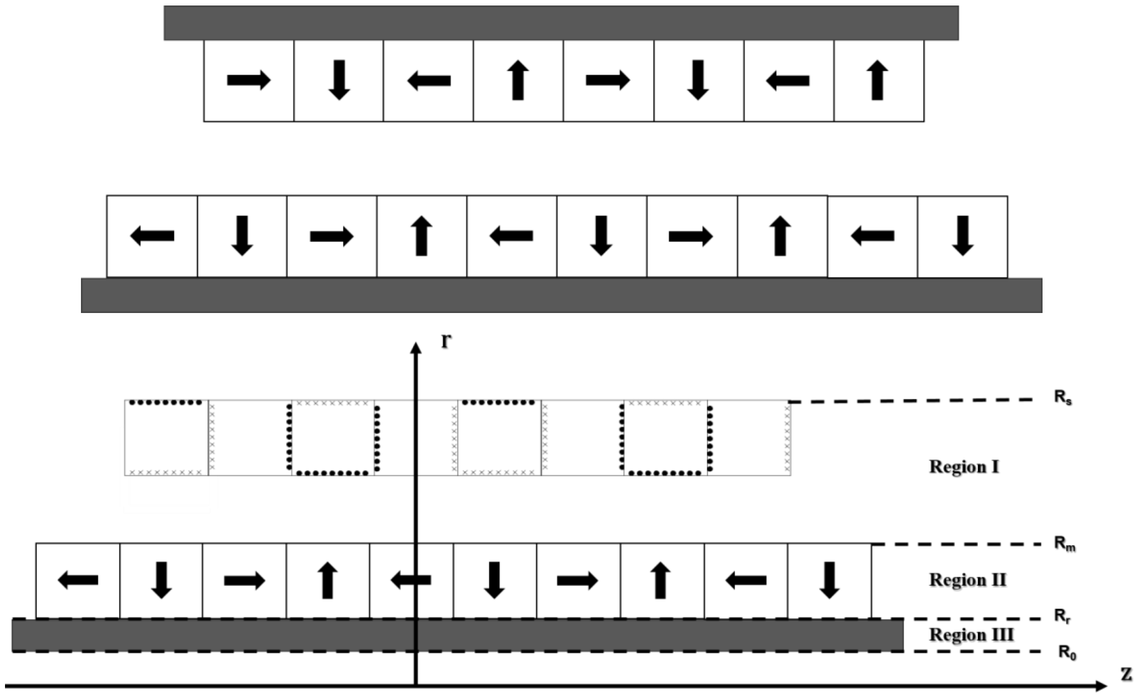

Figure 5-4 Equivalent MLS System

In this work, the MLS nut is assumed to conserve the same electromagnetic properties of a slotless stator. To derive the analytical solution for the magnetic field distribution in the MLS, the following assumptions are made:

1) The magnetic field distributions are calculated from the product of the magnetic field intensity produced by the magnets and relative permeance at any position.

2) The lengths of cyclical Halbach magnet arrays and the cores of the machines in the z direction are assumed to be infinite.

3) The eddy current and hysteresis loss in the back iron are neglected.

Sown in Figure 5-4 is the topology of MLS machines that have Halbach Array magnets in both the nut and screw. The magnets in the nut are assumed to be rectangular coils having surface current density. Analytical solutions derived from the Maxwell equations and simplified boundary conditions are more accurate and more insightful than numerical techniques. Thus a subdomain method is adopted [99]. The proposed model includes three regions: the air-gap-coil as Region I, PM as Region II and back iron as Region III.

For the MLS, the flux density vector $\vec{B}$ and magnet field intensity vector $\vec{H}$ in Regions I, II and III, are respectively related by the following expressions [74]

$$\overrightarrow{B_I} = \mu_0 \overrightarrow{H_I}, \tag{5-6}$$

$$\overrightarrow{B_{II}} = \mu_0 \mu_r \overrightarrow{H_{II}} + \mu_0 \overrightarrow{M}, \tag{5-7}$$

and

$$\overrightarrow{B_{III}} = \mu_0 \mu_{iron} \overrightarrow{H_{III}}, \tag{5-8}$$

where μ_0 is the permeability of the air, μ_r is the relative permeability of permanent magnets, and μ_{iron} is the relative permeability of iron.

The magnetic field intensity vector is derived from the scalar potential as

$$H_z = -\frac{\partial \varphi}{\partial z} \text{ and } H_r = -\frac{\partial \varphi}{\partial r}, \tag{5-9}$$

where H_r and H_z are respectively the r and z direction component of the magnetic field intensity and φ is the magnetic scalar potential. The distribution in regions I, II and III are all governed by the Laplace equation

$$\frac{\partial^2 \varphi}{\partial z^2} + \frac{\partial^2 \varphi}{\partial r^2} = 0 . \tag{5-10}$$

Due to the homogeneous harmonic distribution of the magnetization components M_r and M_z, the general solution for the magnetic scalar potential in these regions is given as:

$$j_n(r,z) = \sum_{k=1,3,5}^{\infty} \left(A_{nk} e^{k\frac{p}{t}r} + B_{nk} e^{-k\frac{p}{t}r} \right) \cos\left(k\frac{p}{t}z \right). \qquad (5\text{-}11)$$

The parameters A_{nk} and B_{nk} are constants in the three regions (n = I, II or III) to be determined by the mean of boundary conditions explained in the following section. With the magnets in the nut modeled as rectangular coils, the corresponding back iron can be neglected. Therefore, the synthetic boundary condition on the surface where r = R_s in Figure 5-4 is the Neumann boundary condition when the permeability of iron is far greater than the air permeability. By neglecting the flux leakage in the back iron region, the Dirichlet boundary conditions is adopted in the boundary at $r = R_0$, namely

$$\begin{aligned} B_{zI}(r,z)\big|_{r=R_s} &= 0 \\ B_{rIII}(r,z)\big|_{r=R_0} &= 0 \end{aligned}, \qquad (5\text{-}12)$$

where B_r and B_z are respectively the r and z direction components of $\vec{B}$.

Since both $B_{zII}(r,z)$ and $B_{rII}(x, y)$ are governed by (5-7), the boundary conditions between R_r and R_m can be very complex. Hence, making the expressions of the magnetic field distributions difficult to solve. Concerning the synthetic boundary conditions at r = R_r and r = R_m, M_r is governed by (5-4), whereas M_z is replaced by an equivalent surface current J_s, expressed as

$$J_s = \frac{M_z}{m_r}. \qquad (5\text{-}13)$$

Thus, the synthetic boundary conditions at r = R_r and r = R_m are expressed as

$$\begin{aligned}
&H_{zI}\left(r,z\right)\Big|_{r=R_m} = H_{zII}\left(r,z\right)\Big|_{r=R_m} + \frac{M_z}{m_r} \\
&B_{rI}\left(r,z\right)\Big|_{r=R_m} = B_{rII}\left(r,z\right)\Big|_{r=R_m} \\
&H_{zIII}\left(r,z\right)\Big|_{r=R_r} = H_{zII}\left(r,z\right)\Big|_{r=R_r} + \frac{M_z}{m_r} \\
&B_{rII}\left(r,z\right)\Big|_{r=R_r} = B_{rIII}\left(r,z\right)\Big|_{r=R_r}
\end{aligned} . \tag{5-14}$$

Solving (5-10) subject to the distributions of Halbach magnetization components and the boundary conditions of (5-11) and (5-13), the proposed general solutions in the air-gap and synthetic nut coils region I is obtained as

$$\begin{aligned}
B_{zI}\left(r,z\right) &= \sum_{k=1,3,5}^{\infty} \frac{4B_r}{pk}\left(A_{rk} - \frac{E_bE_d - e^{-k\frac{p}{t}h_m}E_eE_a + e^{-k\frac{p}{t}h_m}E_eE_c - e^{-2k\frac{p}{t}h_m}E_bE_f}{E_dE_c - e^{-2k\frac{p}{t}h_m}E_aE_f}\right)\left(\frac{e^{2k\frac{p}{t}\left(r-R_s\right)} - 1}{e^{-2k\frac{p}{t}h_g} + 1}\right)e^{-k\frac{p}{t}\left(R_m - r\right)}\sin\left(k\frac{p}{t}z\right) \\
B_{rI}\left(r,z\right) &= \sum_{k=1,3,5}^{\infty} \frac{4B_r}{pk}\left(A_{rk} - \frac{E_bE_d - e^{-k\frac{p}{t}h_m}E_eE_a + e^{-k\frac{p}{t}h_m}E_eE_c - e^{-2k\frac{p}{t}h_m}E_bE_f}{E_dE_c - e^{-2k\frac{p}{t}h_m}E_aE_f}\right)\left(\frac{e^{2k\frac{p}{t}\left(r-R_s\right)} + 1}{e^{-2k\frac{p}{t}h_g} + 1}\right)e^{-k\frac{p}{t}\left(R_m - r\right)}\cos\left(k\frac{p}{t}z\right)
\end{aligned} . \tag{5-15}$$

In the permanent magnet region II, the flux density field is calculated as

$$\begin{aligned}
B_{zII}\left(r,z\right) &= \sum_{k=1,3,5}^{\infty} \frac{4B_r}{pk}\left(\frac{e^{k\frac{p}{t}\left(r-R_m\right)}E_bE_a - e^{k\frac{p}{t}\left(r-R_m-h_m\right)}E_eE_a - e^{k\frac{p}{t}\left(R_r-r\right)}E_eE_c + e^{k\frac{p}{t}\left(R_r-r-h_m\right)}E_bE_f}{E_dE_c - e^{-2k\frac{p}{t}h_m}E_dE_f}\right)\sin\left(k\frac{p}{t}z\right) \\
B_{rII}\left(r,z\right) &= \sum_{k=1,3,5}^{\infty} \frac{4B_r}{pk}\left(A_{rk} - \frac{e^{k\frac{p}{t}\left(r-R_m\right)}E_bE_d - e^{k\frac{p}{t}\left(r-R_m-h_m\right)}E_eE_a + e^{k\frac{p}{t}\left(R_r-r\right)}E_eE_c - e^{k\frac{p}{t}\left(R_r-r-h_m\right)}E_bE_f}{E_dE_c - e^{-2k\frac{p}{t}h_m}E_dE_f}\right)\cos\left(k\frac{p}{t}z\right)
\end{aligned} . \tag{5-16}$$

The general solution in back iron region III is given by

$$B_{zIII}(r,z) = \sum_{k=1,3,5}^{\infty} \frac{4B_r}{\pi k}\left(M_1 - \frac{e^{-2k\frac{\pi}{\tau}h_m}E_eE_a - e^{-k\frac{\pi}{\tau}h_m}E_bE_d - E_eE_c + e^{-k\frac{\pi}{\tau}h_m}E_bE_f}{e^{-2k\frac{\pi}{\tau}h_m}E_aE_f - E_dE_c}\right)\left(\frac{e^{-2k\frac{\pi}{\tau}(r-R_0)}+1}{e^{-2k\frac{\pi}{\tau}h_g}-1}\right)e^{-k\frac{\pi}{\tau}(R_r-r)}\sin\left(k\frac{\pi}{\tau}z\right),$$
$$B_{rIII}(r,z) = \sum_{k=1,3,5}^{\infty} \frac{4B_r}{\pi k}\left(M_1 - \frac{e^{-2k\frac{\pi}{\tau}h_m}E_eE_a - e^{-k\frac{\pi}{\tau}h_m}E_bE_d - E_eE_c + e^{-k\frac{\pi}{\tau}h_m}E_bE_f}{e^{-2k\frac{\pi}{\tau}h_m}E_aE_f - E_dE_c}\right)\left(\frac{e^{-2k\frac{\pi}{\tau}(r-R_0)}-1}{e^{-2k\frac{\pi}{\tau}h_g}-1}\right)e^{-k\frac{\pi}{\tau}(R_r-r)}\cos\left(k\frac{\pi}{\tau}z\right) \quad (5\text{-}17)$$

where

$$\begin{aligned}
E_a &= \left(e^{-2k\frac{\pi}{\tau}h_g} - 1\right) + \frac{1}{\mu_r}\left(e^{-2k\frac{\pi}{\tau}h_g} + 1\right)\\
E_b &= A_{zk}\frac{1}{\mu_r}\left(e^{-2k\frac{\pi}{\tau}h_g} + 1\right) + A_{rk}\left(e^{-2k\frac{\pi}{\tau}h_g} - 1\right)\\
E_c &= \left(e^{-2k\frac{\pi}{\tau}h_g} - 1\right) - \frac{1}{\mu_r}\left(e^{-2k\frac{\pi}{\tau}h_g} + 1\right)\\
E_d &= \left(e^{-2k\frac{\pi}{\tau}h_b} + 1\right) + \frac{\mu_{iron}}{\mu_r}\left(1 - e^{-2k\frac{\pi}{\tau}h_b}\right)\\
E_e &= A_{zk}\frac{\mu_{iron}}{\mu_r}\left(e^{-2k\frac{\pi}{\tau}h_b} + 1\right) + A_{rk}\left(e^{-2k\frac{\pi}{\tau}h_b} + 1\right)\\
E_f &= \left(1 + e^{-2k\frac{\pi}{\tau}h_b}\right) - \frac{\mu_{iron}}{\mu_r}\left(1 - e^{-2k\frac{\pi}{\tau}h_b}\right)
\end{aligned}, \quad (5\text{-}18)$$

such that the thickness of the air gap is $h_g = R_s - R_m$, the thickness of the Halbach Array is $h_m = R_m - R_r$ and the thickness of the back iron is $h_b = R_r - R_0$.

With the flux field solutions developed for each MLS region, the thrust force acting on one pole of the nut as a result of the interaction of the magnetic field produced by the magnets on the nut and the equivalent surface current on the screw is obtained as

$$F_{pole} = \int_S \left(J_{ci} \times B\right) dS \,, \quad (5\text{-}19)$$

where J_{ci} are the current densities in the screw pole and $i=1,2,3,4$ (Figure 5-5).

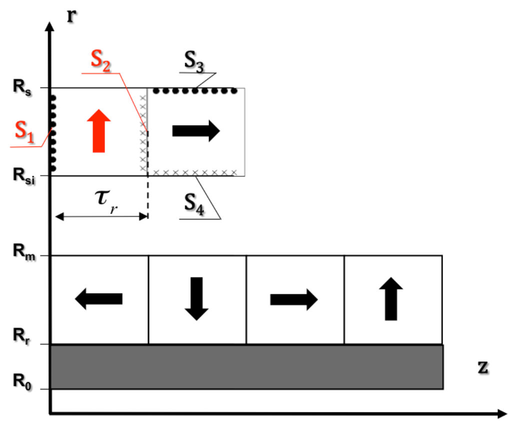

Figure 5-5 Force Calculation over One Pole Pitch

As a result, the total thrust force acting on one pole of the nut is the sum of the four integrals

$$F_{pole} = F_1 + F_2 + F_3 + F_4 = \iint_{S1} \left(J_{c1} \times B\right) dS + \iint_{S2} \left(J_{c2} \times B\right) dS + \iint_{S3} \left(J_{c3} \times B\right) dS + \iint_{S4} \left(J_{c4} \times B\right) dS \qquad (5\text{-}20)$$

where S1, S2, S3 and S4 are the surface areas of the current sheet shown in Figure 5-5. From (5-2)

$$\begin{aligned} \overrightarrow{J_{c1}} &= \frac{B_r}{\mu_0 \mu_r} \cdot \vec{\theta} \\ \overrightarrow{J_{c2}} &= -\frac{B_r}{\mu_0 \mu_r} \cdot \vec{\theta} \\ \overrightarrow{J_{c3}} &= \frac{B_r}{\mu_0 \mu_r} \cdot \vec{\theta} \\ \overrightarrow{J_{c4}} &= -\frac{B_r}{\mu_0 \mu_r} \cdot \vec{\theta} \end{aligned} \qquad (5\text{-}21)$$

The total force calculation will be split in two parts. The first part calculates the force acting on radial magnet F_1+F_2. The second part describes the force acting on side magnet of the Halbach Array pole F_3+F_4. Thus,

$$F_1 + F_2 = \sum_{k=1,3,5}^{\infty} 4\pi J_c I_{rk} \sin\left(k\pi \frac{z_d}{\tau}\right) \sin\left(k\pi \frac{\tau_r}{2\tau}\right), \tag{5-22}$$

where z_d is the is the axial displacement of the radial south pole on the nut with respect to the radial south pole on the screw, τ_r is the axial length of the radial magnet pole shown Figure 5-5, and

$$I_{rk} = \left(i_1 + i_2\right) i_{rk}, \tag{5-23}$$

where

$$i_{rk} = \left(\frac{4B_r}{k\pi}\right)\left(A_{rk} - \left(\frac{E_bE_d - E_eE_a e^{-k\pi\frac{h_m}{\tau}} + E_eE_c e^{-k\pi\frac{h_m}{\tau}} - E_bE_f e^{-2k\pi\frac{h_m}{\tau}}}{E_cE_d - E_aE_f e^{-2k\pi\frac{h_m}{\tau}}}\right)\right)\left(\frac{1}{e^{-2k\pi\frac{h_g}{\tau}} + 1}\right), \tag{5-24}$$

$$i_1 = \frac{\tau}{k\pi}\left(R_s e^{k\pi\frac{R_m - R_s}{\tau}} - R_{si} e^{k\pi\frac{R_m + R_{si} - 2R_s}{\tau}}\right) - \left(\frac{\tau}{k\pi}\right)^2\left(e^{k\pi\frac{R_m - R_s}{\tau}} - e^{k\pi\frac{R_m + R_{si} - 2R_s}{\tau}}\right), \tag{5-25}$$

and $$i_2 = \frac{\tau}{k\pi}\left(R_{si} e^{k\pi\frac{R_m - R_{si}}{\tau}} - R_s e^{k\pi\frac{R_m - R_s}{\tau}}\right) - \left(\frac{\tau}{k\pi}\right)^2\left(e^{k\pi\frac{R_m - R_s}{\tau}} - e^{k\pi\frac{R_m - R_{si}}{\tau}}\right). \tag{5-26}$$

Then,

$$F_3 + F_4 = \sum_{k=1,3,5}^{\infty} \frac{4\pi\tau}{k} J_c \cos\left(k\pi \frac{\left(z_d - \frac{\tau}{2}\right)}{\tau}\right) \sin\left(k\pi \frac{\tau - \tau_r}{2\tau}\right)\left(R_{si}B_{kRsi} - R_sB_{kRs}\right), \tag{5-27}$$

where

$$B_{kRsi} = \frac{4B_r}{\pi k}\left(A_{rk} - \frac{E_bE_d - e^{-k\frac{\pi}{\tau}h_m}E_eE_a + e^{-k\frac{\pi}{\tau}h_m}E_eE_c - e^{-2k\frac{\pi}{\tau}h_m}E_bE_f}{E_dE_c - e^{-2k\frac{\pi}{\tau}h_m}E_aE_f}\right)\left(\frac{e^{2k\frac{\pi}{\tau}\left(R_{si} - R_s\right)} + 1}{e^{-2k\frac{\pi}{\tau}h_g} + 1}\right) e^{-k\frac{\pi}{\tau}\left(R_m - R_{si}\right)} \tag{5-28}$$

and

$$B_{kRs} = \frac{4B_r}{\pi k}\left(A_{rk} - \frac{E_b E_d - e^{-k\frac{\pi}{\tau}h_m} E_e E_a + e^{-k\frac{\pi}{\tau}h_m} E_e E_c - e^{-2k\frac{\pi}{\tau}h_m} E_b E_f}{E_d E_c - e^{-2k\frac{\pi}{\tau}h_m} E_a E_f} \right)\left(\frac{2}{e^{-2k\frac{\pi}{\tau}h_g} + 1} \right) e^{-k\frac{\pi}{\tau}\left(R_m - R_s\right)} . \qquad (5\text{-}29)$$

5.3 FEA Validation

Given the analytical expression of the magnetic flux and the thrust force developed previously, an FEA analysis has been performed to validate the analytical model obtained in the previous section. A study case is presented in this part of the manuscript. Given the same inputs both analytical and numerical simulation have been realized and both results have been compared.

Analytical simulations have been performed for the 6-poles MLS assembly shown in Figure 5-1. The main design parameters are given in Table **5**-**1**.

Table 5-1 Main Design Parameters

Description	Value
Nut Length	304.8 mm
Screw Length	152.4 mm
MLS Outer Diameter	152.4 mm
Back Iron Thickness	10 mm
Magnet Thickness	25.4 mm
Air-Gap Length	1 mm
Lead	50.8 mm
Pole Pitch	25.4 mm
Magnet Grade	N48H
Magnet Ratio	0.6

The MLS system which contains 6 poles of magnets along the screw and 12 poles of magnets on the nut so that at any displacement less than six pole-pitches, there are always six active poles engaged in generating thrust force. The analytical model calculation developed in section 2 is based only on one pole pitch. Thus, the resulting thrust estimation will be multiplied by the number of active poles (four in this case).

In the 3-D FEA model, a Dirichlet boundary condition is adopted at the radius far away from the MLS. The calculations are performed with the helical disposition of magnets as shown in Figure 5-6. This 3-D FEA validation process of the proposed 2-D analytical model is used to assess the model accuracy/utility when optimizing the MLS system.

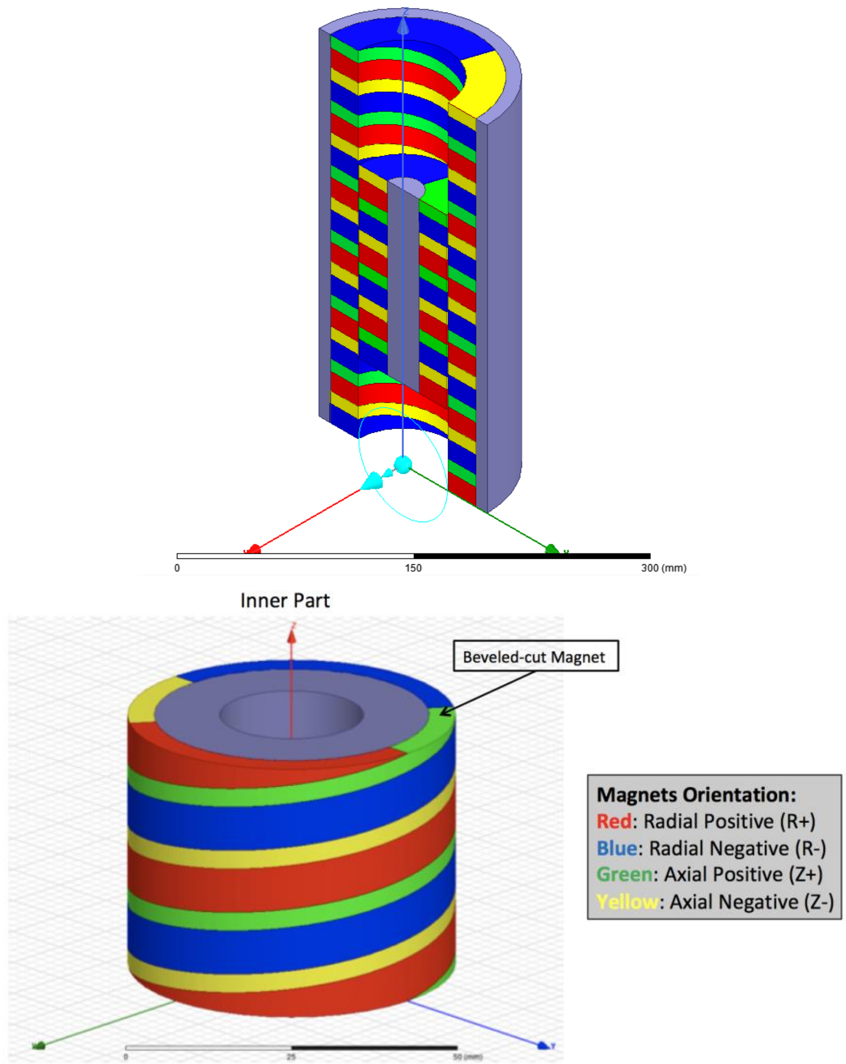

Figure 5-6 3D FEA Model and Configuration

Shown in Figure 6 are the air-gap flux density distributions. It can be seen that the peak air gap axial flux density is 1.16T while that of the radially magnetize one is 1.21T.

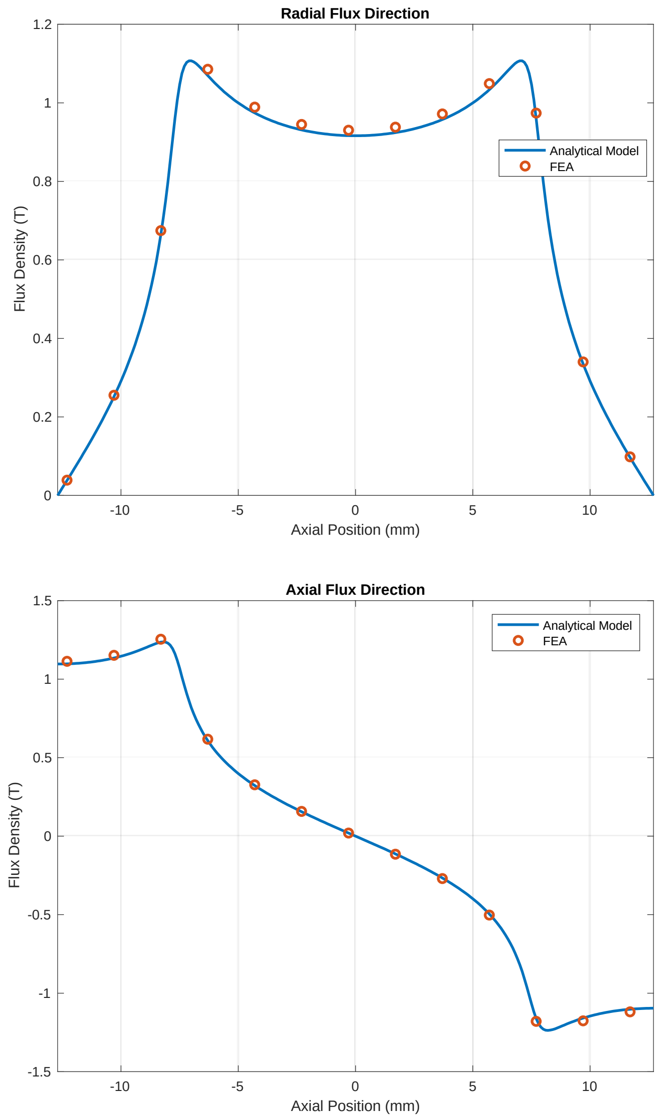

Figure 5-7 Air-Gap Flux Density (a) Radial Direction, (b) Axial Direction

Presented in Figure 5-8 is a comparison of the analytical and 3-D FEA predicted thrust force as a function of the axial displacement. As seen, the analytical calculation matches the FEA result. The maximum difference between the two is less than 3% mostly due to the effect of saturation and flux leakage that are neglected in the analytical prediction.

As shown in Figure 5-8**Error! Reference source not found.**, when the relative displacement shown in Figure 5-3 between the radial north or radial south poles on the screw and nut is zero, the magnetic field distribution is symmetrical with respect to the axial center of the device and the resulting thrust force is zero. However, when the displacement between the magnetic radial poles increases, the tangential component of the air-gap flux density becomes significant, and the thrust force will be developed. This force will reach its maximum when the displacement is half a pole-pitch.

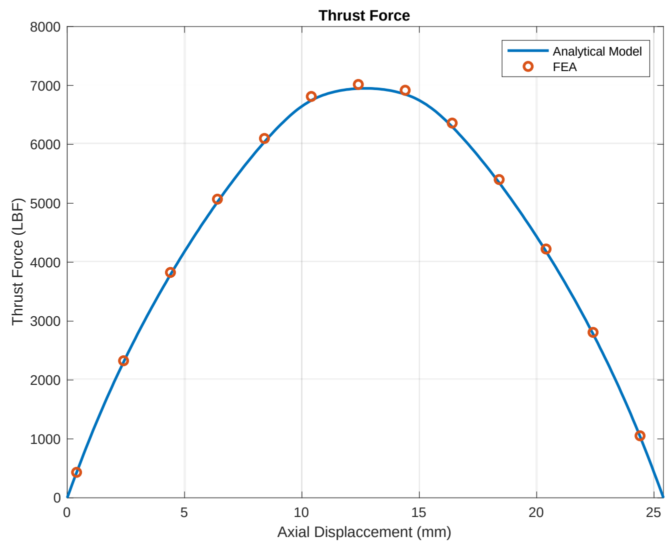

Figure 5-8 Resultant Thrust Force Validation

The simulated FEA magnetic field distributions are presented in Figure 5-9. It can be noted that most of the magnetic flux lines pass through the air gap. However, it has been noted that the flux leakage is significantly low in the Halbach MLS due to the use of the axially magnetized permanent magnets. To minimize this leakage even more a sensitivity analysis is performed with respect to the Halbach Array magnet ratio and concludes its impact in the flux density and the resulting thrust force.

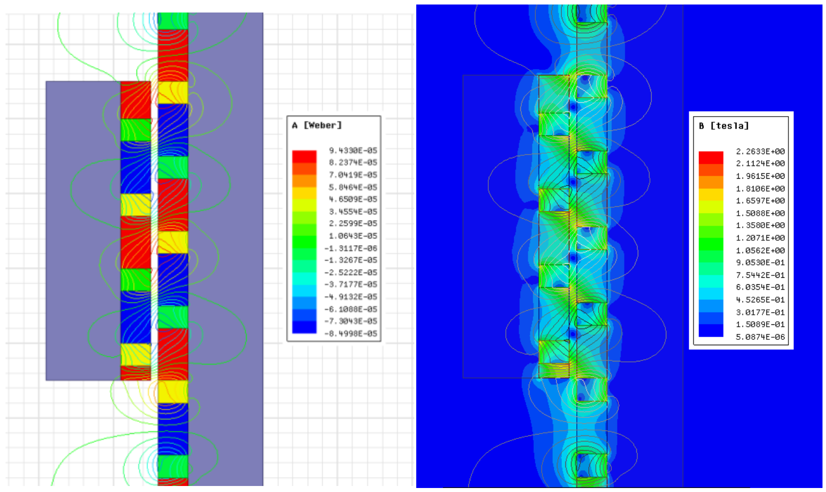

Figure 5-9 Magnetic Field Distribution on Halbach MLS

The developed analytical model had utility in a variety of simulation based design processes in different application fields. For example, an optimization process that consists of minimizing the overall cost of the MLS while achieving a thrust force level. The magnet cost is presenting around 60% of the overall cost of the MLS. Therefore, minimizing the magnet usage will impact dramatically the MLS price. A sequential quadratic programming algorithm can be deployed to minimize the magnet volume with the constraint of keeping the thrust force at a specific level.

5.4 Simulation Based Design

Early stage design provides the greatest opportunities to explore design alternatives and perform trade studies before costly design decisions are made. The goal of this section is to develop a simulation based analysis that selects the optimal MLS embodiment based on geometric constraints, cost, capacity and application.

5.4.1 Analytical Modeling

5.4.1.1 Magnet Ratio Sensitivity Analysis

By varying the magnet ratio, the proposed model predicts a variety of magnetization patterns as presented in Figure 5-10. It should be noted that the conventional MLS has a magnet ratio M_R equal to unity, while for the Halbach MLS having a M_R equal to 0.5, the axial and the radial magnet segments have the same width. The highest radial flux density peak value (RFDPV) is given by the lowest Halbach Array magnet ratio (M_R=0.5), which is approximately 73% higher than the conventional magnetization. By increasing the magnet ratio, the RFDPV decreases and the shape of the flux becomes wider within each pole range. This is because the central magnet with radial magnetization becomes wider as the magnet ratio increases. On one hand, the radial air gap flux density waveform reaches its widest and lowest peak amplitude in the magnet ratio of unity. On the other hand the highest axial flux density peak value (AFDPV) is given by Halbach Array magnet ratio M_R equal to 0.9, which is approximately 30% higher than the case of M_R equal to 0.5. By increasing the magnet ratio, the AFDPV increases and the shape of the flux becomes narrower within each pole range. The reason is that the axial magnet becomes wider as the magnet ratio decreases. The axial air gap flux density waveform reaches its widest and lowest peak amplitude in the magnet ratio of 0.5.

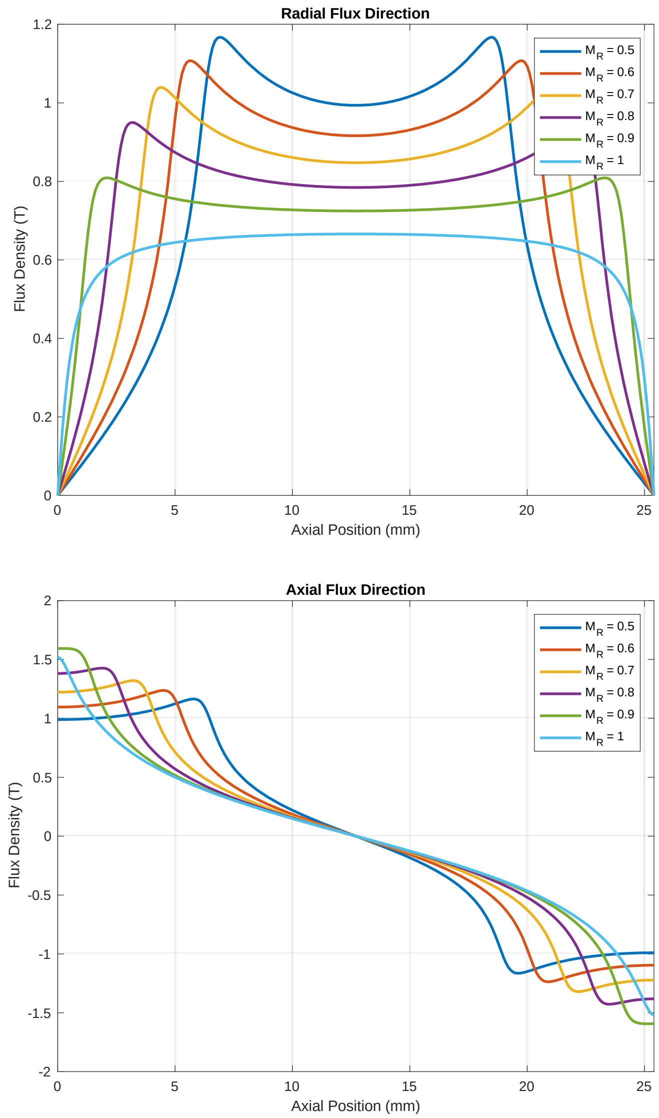

Figure 5-10 Air-Gap Flux Density (a) Radial Direction, (b) Axial Direction

While for the thrust force shown in Figure 5-11, the highest force is given with a magnet ratio equal to 0.5 for our particular case. It can be seen that the MLS having M_R equal to 0.6 has approximately 95% higher thrust force than the conventional MLS. Also, it should be noted that the thrust force performance could be improved, when adopting high performance PMs.

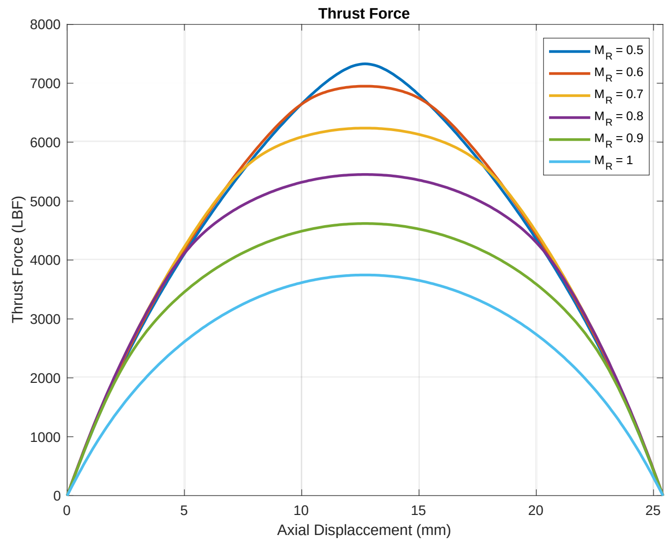

Figure 5-11 Thrust Force Variation with respect to Magnet Ratio M_R

As a result the percent increase of thrust force generated by Halbach Array magnetization comparing to conventional magnetization depends on the magnet ratio adopted in the design. Thus the magnet ratio should be chosen properly.

5.4.1.2 Magnet Thickness Sensitivity Analysis

Presented in this part is a sensitivity analysis with respect to magnet thickness used to investigate the cases where Halbach Array is advantageous comparing to conventional magnetization. The magnet ratio is fixed to 0.5 and varying the magnet thickness from 12.7 mm to 25.4 mm.

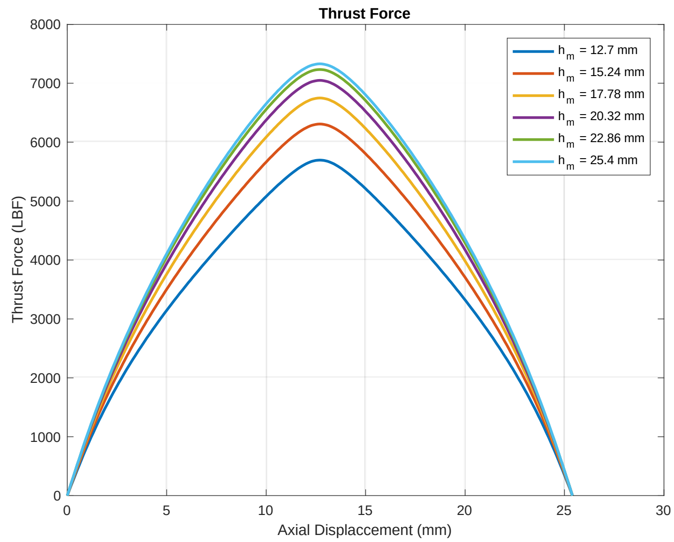

Figure 5-12 Thrust Force Variation with respect to Magnet Thickness h_m

The resultant thrust force generated when varying the magnet thickness is presented in Figure 5-12. It is worth noting that the thicker the magnets are the higher the force will be. However, adopting thick magnets will increase the used magnet volume. Consequently, this will increase the overall cost of the MLS.

5.4.1.3 Pole Pitch Sensitivity Analysis

Now, varying the pole pitch between 25.4 mm and 50.8 mm and M_R equal to 0.5 while keeping all other parameters fixed and given in Table **5-1**.

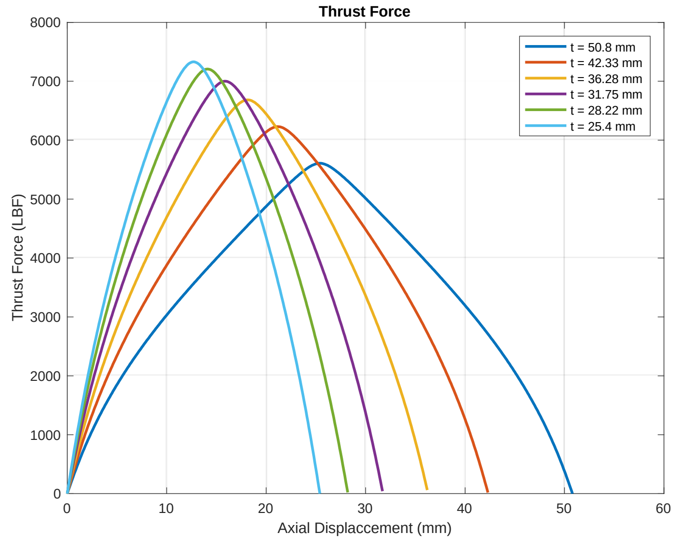

Figure 5-13 Thrust Force Variation with respect to Pole Pitch τ

As illustrated in Figure 5-13, the thrust force is increasing while to pole pitch is becoming smaller. The percent increase in force between τ equal to 50.8 mm and 25.4 is approximately 30%. Here the manufacturing feasibility is a major constraint to produce the maximum thrust force.

5.4.2 Automated System Design

The main role of simulation-based design is based system simulation by evaluating design alternatives obtained in the conceptual design. Modeling often begins with the conceptual designs along with the system requirements and the definition of key performance indicators. Hence, the developed analytical model of MLS is employed given the objective function along with simulations inputs and modeling constraints as explained in the automated system design flow chart described in Figure 5-14. The design parameters are then selected to simulate the air-gap magnetic field and predict the thrust force generated.

It is quite common in many optimization problems to have two or more conflicting design objectives. They could be aggregated using a weighted sum in a single objective. But in this way one objective could tend to be predominant in the selection of the optimal solution. A more effective approach to cope with multi-objective problems introduces the concept of dominance and ranks the solutions in Pareto fronts.

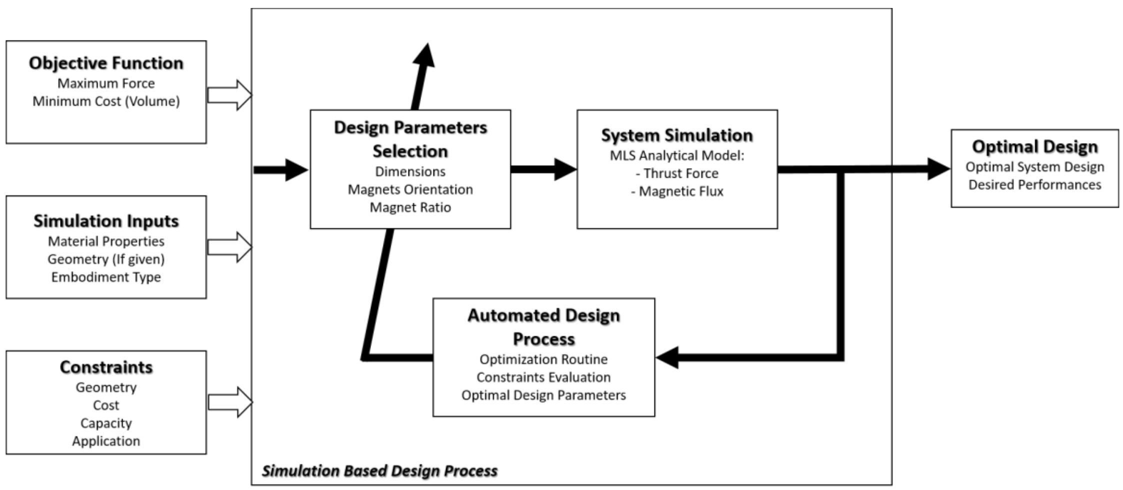

Figure 5-14 Automated System Design Flow Chart

In the following, Pareto front optimization algorithm [137] is deployed to maximize the magnetic force and minimize the permanent magnet usage under the geometric constraints. For the MLS optimization model, there are two objective functions and seven variables presented in Table **5-2**. Pareto front analysis used genetic algorithm. The upper and lower bounds of design parameters are presented in Table **5-2**.

Table 5-2 Main Design Parameters

Description	Lower Bound	Upper Bound
Screw Length	152.4 mm	203.2 mm
MLS Outer Diameter	152.4 mm	203.2 mm
Back Iron Thickness	8 mm	15 mm
Magnet Thickness	12.7 mm	25.4 mm
Air-Gap Length	1 mm	2 mm
Pole Pitch	12.7 mm	50.8 mm
Magnet Ratio	0.5	1

Generating a set of points using this procedure, the Pareto front results are computed and presented in Figure 5-15. It will be very useful for making decision and testing the analytical model capabilities before moving onto the manufacturing phase. Selection of particular solution in the Pareto front will decide how much to favor (penalize) the thrust force and penalize (favor) the magnet volume usage.

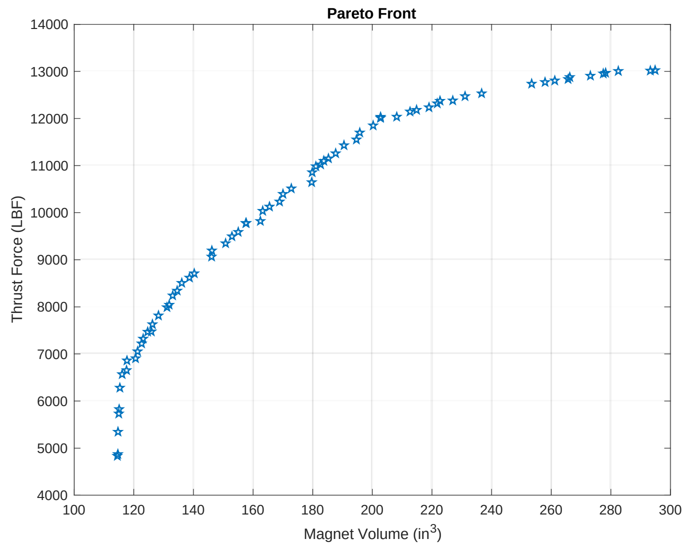

Figure 5-15 Pareto Front Analysis

5.5 Conclusions

In this chapter, an analytical model for high force density MLS based on the concept of magnetic screw-nut has been developed. The novel 2D analytical model was established based on magnetic scalar potential and equivalent current methods to predict the generated electromagnetic performances, namely the magnetic flux density and the thrust force. Moreover, an accurate prediction of the generated magnetic thrust force given a variety of design parameters such as material properties, PM grade and geometric embodiment of the MLS is developed. The analytical model has been integrated with an optimization routine to enable design optimization of the proposed device by minimizing the permanent magnets volume used to generate a constrained thrust force given within a specific interval to achieve a high force demanding application. In fact, the developed model would be a great asset in the simulation based design process.

The use of a Halbach PM arrays in the proposed MLS offers the advantages of developing a high force density only by converting a low speed rotation motion. The proposed Halbach magnetized MLS has been compared with conventional design variant through sensitivity analysis on the magnet ratio parameter. The analytical model has proven his utility for simulation-based design applications due to its reduced running time compared to finite element analysis software.

In the last part, automated design was carried out using Pareto optimization algorithm that can adequately generate the operating front of the MLS. The presented work can be used as an alternative to the FEA methods by overcoming their long running time limitation while preserving accuracy and complexity.

6 CONCLUSIONS AND FUTURE WORK

6.1 Conclusions

This thesis developed a general analytical model which is capable of predicting the electromagnetic performance of permanent magnet machines with Halbach Array, having different magnet remanence and arc for each single magnet segment. The developed analytical models and related investigations were examined by finite element analyses.

A two-dimensional mathematical model estimating the torque of a Halbach Array surface permanent magnet (SPM) motor with a non-overlapping winding layout is developed. The magnetic field domain for the 2-D motor model is divided into five regions: slots, slot openings, air gap, rotor magnets and rotor back iron. Applying the separation of variable method, an expression of magnetic vector potential distribution can be represented as Fourier series. By considering the interface and boundary conditions connecting the proposed regions, the Fourier series constants are determined. The proposed model offers a computationally efficient approach to analyze SPM motor designs including those having a Halbach Array. Since the tooth-tip and slots parameters are included in the model, the electromagnetic performance of an SPM motor, described using the cogging torque, back-EMF and electromagnetic torque, can be calculated as function of the slots and tooth-tips effects. The proposed analytical predictions are compared with results obtained from finite-element analysis. Finally, a performance comparison between a conventional and Halbach Array SPM motor is performed.

The Halbach Array magnet configuration provides an augmented magnetic flux field on one side, while cancelled on the other side. In the presented study, much less flux saturation is observed in rotor back iron with Halbach Array configuration compared to the conventional ones. In addition in Halbach-Array design, more magnets could be installed in the rotor to achieve higher torque, with lower risk to causing flux saturation within the rotor back iron; on the other hand, less back iron material is needed in the Halbach Array designed rotor. This helps decreasing the motor total weight. Therefore, a direct benefit could deduct in traction application.

Halbach Array magnet ratio is one of the most important design parameters in Halbach Array SPM motors, because it influences on the flux density in both peak value and waveform, which will therefore stimulate the resultant torque. With the appropriate magnet ratio in the motor embodiment, the Halbach Array motor is capable of producing higher torque for the same volume of magnets. Furthermore, potentially lower supply current requirements of the Halbach Array SPM motor would reduce the heat loss and increase the motor operating efficiency.

The developed motor analytical model provides a fast and reliable tool to optimize motors that fulfill the specified requirements, while offering the desire level of performance across the duty cycles.

The reduction of losses offered by Halbach Array magnetization provides then higher efficiency over wider speed range. This was proven by the increase of average efficiency over drive cycles. While Halbach Array motor speed range is reduced compared to Nissan Leaf, better electromagnetic performances are drawn in driving conditions, increased overall efficiency and higher driving range. The reduction of level of the harmonics of the excitation flux created by the HA permanent magnets decreases iron losses in the synchronous motor core. Additionally, increasing the amplitude of the fundamental component of the electromotive force and the fundamental harmonic, while reducing the harmonics of higher rank, is possible with a HA magnetization in the rotor. As a result, this will lead to lower copper losses and lower iron losses due to the absence of higher harmonics in the stator core. Reduction of the losses is of particular high interest for traction applications where a vehicle operates at variable speed. The design techniques for Halbach Array motor are presented. A comparison analysis is carried out between the optimized design with the IPM used in Nissan Leaf 2012 model based on two standard driving cycles: the Urban Dynamometer Driving Schedule (UDDS) and US06 Supplemental Federal Test Procedure (SFTP). These driving cycles are adopted to carefully test the traction motor performance in terms of torque, efficiency, and thermal condition, while satisfying the required torque–speed operating range. The torque–speed envelope is derived under the power limit that the Nissan Leaf inverter can supply which is 80 kW. Based on the analytical design presented in, the torque is estimated to calculate current and losses in the HA traction motor. Accordingly, The benefits and the disadvantages of the Halbach Array motor for EV tractions are elaborated. Design guidelines of EV traction motors are provided.

Chapter 5 presents a newly developed analytical model of a double-sided Halbach Array magnetic lead screw. The proposed model is based on using the scalar potential theory to calculate the magnetic field distribution from the inner part of the

MLS while presenting the permanent magnets in the outer part as an equivalent surface distributed currents. This allows calculating the electromagnetic performances such as the generated thrust force. The results of our model present significant match during validation with finite elements analysis. Based on such accuracy, the developed model is deployed during early stage design process of the MLS. The analytical model has been incorporated within a simulation based analysis process. This aims to have elaborated insights and trade-off studies during the early stage design phase. Pareto front method is applied to calculate the optimal embodiment of the MLS with respect to geometric, cost, capacity and application constraints. The adoption of a Halbach PM arrays in the proposed MLS offers the advantages of developing a high force density only by converting a low speed rotation motion. The optimized Halbach magnetized MLS has been compared with conventional design variant through sensitivity analysis on the magnet ratio parameter.

The analytical model has proven its utility for simulation-based design applications due to its reduced running time compared to finite element analysis software. The presented work can be used as an alternative to the FEA methods by overcoming their long running time limitation while preserving accuracy and complexity. Analytical models are powerful tools for the design and research of PM brushless machines. This thesis has developed a package of analytical models, of both high accuracy and physical understanding. The developed analytical models are applicable to permanent magnet machines and magnetic linear screw having segmented Halbach array. An analytical model is developed to predict optimal magnet ratio for Halbach Array. Their accuracies have been extensively verified by finite element analysis.

Halbach array exhibits higher fundamental air-gap flux density than radial magnetized case, especially when the magnet is thick. The electromagnetic torque and magnet usage efficiency for between PM brushless machines having conventional pole, optimized Halbach arrays and proposed magnet poles have been comparatively studied. The influences of design parameters on electromagnetic performances are also extensively studied. It is found that the thicker the magnet, the smaller the optimal magnet ratio R_{mp} for machines having rotor back iron. This is valid for SPM and MLS. In contrast to the iron-cored rotor, the optimal magnet ratio increases as the magnet thickness increases for the air-core rotor. In addition, the optimal magnet5 ratio for the machines having an iron-cored rotor is always greater than 0.5, while the machines having an air-cored rotor is always lower than 0.5.

6.2 Future Work

Ultimately, with the advent of Halbach Array magnetization, it is also widely applied on:

- Axial field motors
- Generator design and application
- Rotary machines
- Magnetic gears (Spur, coaxial and cycloidal)
- Slotless machines
- Maglev and eddy current brake systems
- Tubular machines

- Linear motors

Analytical models could be developed using subdomain models and optimized magnet ratio to draw the maximum electromagnetic performances.

Besides, following the analytical research work in this thesis, future research includes:

- Extending the 2-D field model with subdomain method to estimate magnets degradation.
- Coupling the developed design with new control system to minimize power supply.
- Extending analysis for MLS with different magnet shape and grades and including demagnetization in the developed model.

Rolling element bearings are critical components in motors and monitoring their condition is critical to avoid failures. The literature indicates that even though the emphasis is on vibration measurement methods for the detection of defects in rolling element bearings in SPM motor, stator current harmonics measurement can be an effective alternative to the vibration measurement because of its faster diagnosis. Very few studies have been carried out on stator current monitoring of an SPM motor for the detection of defects in these rolling bearing along with vibration monitoring and other condition monitoring methods. Hence, there is a need for a comprehensive study of Halbach SPM motor rolling element-bearing faults detection using stator current harmonics measurement in combination with vibration, acoustic emission and Halbach SPM condition monitoring techniques. So future work can undertake for the detection and diagnosis of SPM motor rolling element-bearing faults have been carried out using vibration monitoring, acoustic emission and shock pulse along with stator current harmonics measurements. A comparison analysis could be made between conventional SPM and Halbach SPM.

REFERENCES

1. https://www.un.org/development/desa/statements/wp-content/uploads/sites/12/2016/01/Overview_SDGs_EN.pdf.
2. Perera, F., *Pollution from fossil-fuel combustion is the leading environmental threat to global pediatric health and equity: Solutions exist.* International journal of environmental research and public health, 2017. **15**(1): p. 16.
3. https://www.eia.gov/todayinenergy/detail.php?id=30712.
4. https://www.ucsusa.org/clean-energy/coal-and-other-fossil-fuels/environmental-impacts-of-natural-gas - .XGxHhC-ZOMI.
5. https://www.eia.gov/energyexplained/?page=us_energy_transportation.
6. Bicer, Y. and I. Dincer, *Life cycle environmental impact assessments and comparisons of alternative fuels for clean vehicles.* Resources, Conservation and Recycling, 2018. **132**: p. 141-157.
7. https://www.reuters.com/article/us-britain-autos-idUSKBN1AB0U5.
8. https://www.reuters.com/article/environment-norway-autos/more-than-half-of-new-norway-car-sales-now-electric-or-hybrid-idUSL8N1OY194.
9. http://theconversation.com/electric-vehicles-are-changing-the-world-and-theyre-only-just-getting-started-90402.
10. https://delfastbikes.com/blog/new-trend-on-the-road-are-electric-vehicles-going-to-change-the-world/.
11. http://energy.mit.edu/news/electric-motors-find-new-roles-robots-ships-cars-microgrids/.
12. http://news.mit.edu/2016/electric-motors-find-new-roles-james-kirtley-1024.

13. Berg, W., S. Nowak, M. Kelly, S. Vaidyanathan, M. Shoemaker, A. Chittum, M. DiMascio, and C. Kallakuri. *The 2016 state energy efficiency scorecard*. 2016. American Council for an Energy-Efficient Economy.

14. McCoy, G.A. and J.G. Douglass, *Premium Efficiency Motor Selection and Application Guide–A Handbook for Industry*. 2014, Washington State University Energy Program.

15. Marinescu, M. and N. Marinescu, *Compensation of anisotropy effects in flux-confining permanent-magnet structures.* IEEE Transactions on Magnetics, 1989. **25**(5): p. 3899-3901.

16. Yuan, F., L. Zeng, X. Chen, C. Liang, X. Ding, and X. Luo, *A Multi-Module Electrodynamic Exciter with a Variable Pole-Arc Ratio Disk Halbach Array for a High-Bandwidth Dynamic Torsional Stiffness Test.* Sensors, 2019. **19**(6): p. 1272.

17. Jing, L., T. Zhang, Y. Gao, R. Qu, Y. Huang, and T. Ben, *A Novel HTS Modulated Coaxial Magnetic Gear With Eccentric Structure and Halbach Arrays.* IEEE Transactions on Applied Superconductivity, 2019. **29**(5): p. 1-5.

18. Halbach, K., *Design of permanent multipole magnets with oriented rare earth cobalt material.* Nuclear instruments and methods, 1980. **169**(1): p. 1-10.

19. Zhu, Z. and D. Howe, *Halbach permanent magnet machines and applications: a review.* IEE Proceedings-Electric Power Applications, 2001. **148**(4): p. 299-308.

20. Merritt, B.T., R.F. Post, G.R. Dreifuerst, and D.A. Bender, *Halbach array motor/generators: A novel generalized electric machine*. 1994, Lawrence Livermore National Lab., CA (United States).

21. Dwari, S. and L. Parsa, *Design of Halbach-array-based permanent-magnet motors with high acceleration.* IEEE Transactions on industrial electronics, 2011. **58**(9): p. 3768-3775.

22. Jian, L. and K. Chau, *A coaxial magnetic gear with halbach permanent-magnet arrays.* IEEE Transactions on Energy conversion, 2010. **25**(2): p. 319-328.

23. Xie, K., D. Li, R. Qu, and Y. Gao, *A novel permanent magnet vernier machine with Halbach array magnets in stator slot opening.* IEEE Transactions on Magnetics, 2017. **53**(6): p. 1-5.

24. Jang, S.-M., S.-H. Lee, and I.-K. Yoon, *Design criteria for detent force reduction of permanent-magnet linear synchronous motors with Halbach array.* IEEE Transactions on magnetics, 2002. **38**(5): p. 3261-3263.

25. Häfeli, U.O., K. Gilmour, A. Zhou, S. Lee, and M.E. Hayden, *Modeling of magnetic bandages for drug targeting: Button vs. Halbach arrays.* Journal of Magnetism and Magnetic Materials, 2007. **311**(1): p. 323-329.

26. Zheng, P., J. Bai, C. Tong, Y. Sui, Z. Song, and Q. Zhao, *Investigation of a novel radial magnetic-field-modulated brushless double-rotor machine used for HEVs.* IEEE transactions on magnetics, 2012. **49**(3): p. 1231-1241.

27. Liu, R., H. Zhao, P. Zheng, X. Gan, R. Zhao, and B. Kou. *Experimental evaluation of a radial-radial-flux compound-structure permanent-magnet*

synchronous machine used for HEVs. in *2008 14th Symposium on Electromagnetic Launch Technology*. 2008. IEEE.

28. Zhao, J., B. Li, and Z. Gu, *Research on an axial flux PMSM with radially sliding permanent magnets.* Energies, 2015. **8**(3): p. 1663-1684.

29. Platt, D., *Permanent magnet synchronous motor with axial flux geometry.* IEEE Transactions on Magnetics, 1989. **25**(4): p. 3076-3079.

30. Wu, L., Z. Zhu, D.A. Staton, M. Popescu, and D. Hawkins, *Comparison of analytical models of cogging torque in surface-mounted PM machines.* IEEE Transactions on Industrial Electronics, 2011. **59**(6): p. 2414-2425.

31. Bianchi, N., S. Bolognani, and F. Luise, *Potentials and limits of high-speed PM motors.* IEEE Transactions on Industry Applications, 2004. **40**(6): p. 1570-1578.

32. Binder, A., T. Schneider, and M. Klohr, *Fixation of buried and surface-mounted magnets in high-speed permanent-magnet synchronous machines.* IEEE Transactions on Industry Applications, 2006. **42**(4): p. 1031-1037.

33. Soleimani, J., A. Vahedi, and S. Mirimani, *Inner permanent magnet synchronous machine optimization for HEV traction drive application in order to achieve maximum torque per ampere.* 2011.

34. Muñoz, A.R. and T.A. Lipo, *Dual stator winding induction machine drive.* IEEE Transactions on Industry Applications, 2000. **36**(5): p. 1369-1379.

35. Ishak, D., Z. Zhu, and D. Howe, *Comparison of PM brushless motors, having either all teeth or alternate teeth wound.* IEEE Transactions on Energy Conversion, 2006. **21**(1): p. 95-103.

36. Wrobel, R. and P.H. Mellor, *Design considerations of a direct drive brushless machine with concentrated windings.* IEEE Transactions on energy conversion, 2008. **23**(1): p. 1-8.

37. Wu, L., R. Qu, D. Li, and Y. Gao, *Influence of pole ratio and winding pole numbers on performance and optimal design parameters of surface permanent-magnet vernier machines.* IEEE Transactions on Industry Applications, 2015. **51**(5): p. 3707-3715.

38. Choi, G. and T.M. Jahns, *Reduction of eddy-current losses in fractional-slot concentrated-winding synchronous PM machines.* IEEE Transactions on Magnetics, 2016. **52**(7): p. 1-4.

39. Abdel-Khalik, A.S., S. Ahmed, and A.M. Massoud, *Effect of multilayer windings with different stator winding connections on interior PM machines for EV applications.* IEEE Transactions on Magnetics, 2015. **52**(2): p. 1-7.

40. Lipo, T.A., *Introduction to AC machine design*. Vol. 63. 2017: John Wiley & Sons.

41. Tovar-Barranco, A., F. Briz, A. López-de-Heredia, and I. Villar. *Comparison of permanent magnet synchronous machines with concentrated windings and different rotor configurations*. in *2017 19th European Conference on Power Electronics and Applications (EPE'17 ECCE Europe)*. 2017. IEEE.

42. Cistelecan, M.V., F.J. Ferreira, and M. Popescu. *Three phase tooth-concentrated multiple-layer fractional windings with low space harmonic content*. in *2010 IEEE Energy Conversion Congress and Exposition*. 2010. IEEE.

43. Reddy, P.B., A.M. El-Refaie, and K.-K. Huh, *Effect of number of layers on performance of fractional-slot concentrated-windings interior permanent magnet machines.* IEEE Transactions on Power Electronics, 2014. **30**(4): p. 2205-2218.

44. Dajaku, G. and D. Gerling. *A novel 24-slots/10-poles winding topology for electric machines*. in *2011 IEEE International Electric Machines & Drives Conference (IEMDC)*. 2011. IEEE.

45. Mi, C., G.R. Slemon, and R. Bonert, *Modeling of iron losses of permanent-magnet synchronous motors.* IEEE Transactions on Industry applications, 2003. **39**(3): p. 734-742.

46. Mi, C.C., G.R. Slemon, and R. Bonert, *Minimization of iron losses of permanent magnet synchronous machines.* IEEE Transactions on Energy Conversion, 2005. **20**(1): p. 121-127.

47. Roshen, W., *Iron loss model for permanent-magnet synchronous motors.* IEEE Transactions on Magnetics, 2007. **43**(8): p. 3428-3434.

48. Chai, F., P. Liang, Y. Pei, and S. Cheng, *Magnet shape optimization of surface-mounted permanent-magnet motors to reduce harmonic iron losses.* IEEE Transactions on Magnetics, 2016. **52**(7): p. 1-4.

49. Huang, W.-Y., A. Bettayeb, R. Kaczmarek, and J.-C. Vannier, *Optimization of magnet segmentation for reduction of eddy-current losses in permanent magnet synchronous machine.* IEEE Transactions on energy conversion, 2010. **25**(2): p. 381-387.

50. Xia, Y., G. Li, Z. Qian, Q. Ye, and Z. Zhang. *Research on rotor magnet loss in fractional-slot concentrated-windings permanent magnet motor*. in *2016 IEEE 11th Conference on Industrial Electronics and Applications (ICIEA)*. 2016. IEEE.

51. Wang, J., D. Howe, and G.W. Jewell, *Analysis and design optimization of an improved axially magnetized tubular permanent-magnet machine.* IEEE transactions on energy conversion, 2004. **19**(2): p. 289-295.

52. Mallinson, J., *One-sided fluxes--A magnetic curiosity?* IEEE Transactions on magnetics, 1973. **9**(4): p. 678-682.

53. Bjørk, R., A. Smith, and C.R.H. Bahl, *Analysis of the magnetic field, force, and torque for two-dimensional Halbach cylinders.* Journal of magnetism and magnetic materials, 2010. **322**(1): p. 133-141.

54. Shute, H.A., J.C. Mallinson, D.T. Wilton, and D.J. Mapps, *One-sided fluxes in planar, cylindrical, and spherical magnetized structures.* IEEE Transactions on Magnetics, 2000. **36**(2): p. 440-451.

55. Xia, Z., Z. Zhu, and D. Howe, *Analytical magnetic field analysis of Halbach magnetized permanent-magnet machines.* IEEE Transactions on Magnetics, 2004. **40**(4): p. 1864-1872.

56. Zhu, Z.Q. and D. Howe, *Halbach permanent magnet machines and applications: a review.* IEE Proceedings-Electric Power Applications, 2001. **148**(4): p. 299-308.

57. Ng, K., Z. Zhu, and D. Howe, *Open-circuit field distribution in a brushless motor with diametrically magnetised PM rotor, accounting for slotting and*

eddy current effects. IEEE Transactions on Magnetics, 1996. **32**(5): p. 5070-5072.

58. Shen, Y., G.Y. Liu, Z.P. Xia, and Z.Q. Zhu, *Determination of maximum electromagnetic torque in PM brushless machines having two-segment Halbach array.* IEEE Transactions on Industrial Electronics, 2014. **61**(2): p. 718-729.

59. Wang, H., Y. Ye, Q. Wang, Y. Dai, Y. Yu, and P. Weng, *Analysis for ring arranged axial field Halbach permanent magnets.* IEEE Transactions on applied superconductivity, 2006. **16**(2): p. 1562-1565.

60. Looser, A., T. Baumgartner, J.W. Kolar, and C. Zwyssig, *Analysis and measurement of three-dimensional torque and forces for slotless permanent-magnet motors.* IEEE Transactions on Industry Applications, 2012. **48**(4): p. 1258-1266.

61. Jang, S.-M., S.-S. Jeong, D.-W. Ryu, and S.-K. Choi, *Design and analysis of high speed slotless PM machine with Halbach array.* IEEE transactions on magnetics, 2001. **37**(4): p. 2827-2830.

62. Wu, L., Z. Zhu, D. Staton, M. Popescu, and D. Hawkins, *An improved subdomain model for predicting magnetic field of surface-mounted permanent magnet machines accounting for tooth-tips.* IEEE Transactions on Magnetics, 2011. **47**(6): p. 1693-1704.

63. Zhu, Z. *Recent development of Halbach permanent magnet machines and applications*. in *Power Conversion Conference-Nagoya, 2007. PCC'07*. 2007. IEEE.

64. Zhu, Z., Z. Xia, and D. Howe, *Comparison of Halbach magnetized brushless machines based on discrete magnet segments or a single ring magnet.* IEEE Transactions on Magnetics, 2002. **38**(5): p. 2997-2999.

65. Wang, J., D. Howe, and Z. Lin, *Design optimization of short-stroke single-phase tubular permanent-magnet motor for refrigeration applications.* IEEE Transactions on Industrial electronics, 2010. **57**(1): p. 327-334.

66. Dhulipati, H., S. Mukundan, K.L.V. Iyer, and N.C. Kar. *Skewing of stator windings for reduction of spatial harmonics in concentrated wound PMSM*. in *Electrical and Computer Engineering (CCECE), 2017 IEEE 30th Canadian Conference on*. 2017. IEEE.

67. Hwang, C., S. Cheng, and P. Li. *Design optimization for cogging torque minimization and efficiency maximization of an SPM motor*. in *Electric Machines & Drives Conference, 2007. IEMDC'07. IEEE International*. 2007. IEEE.

68. Islam, J., D. Svechkarenko, R. Chin, A. Szucs, J. Mantere, and R. Sakki. *Cogging torque and vibration analysis of a direct-driven PM wind generator with concentrated and distributed windings*. in *Electrical Machines and Systems (ICEMS), 2012 15th International Conference on*. 2012. IEEE.

69. Lee, J., T. Nomura, and E.M. Dede, *Topology optimization of Halbach magnet arrays using isoparametric projection.* Journal of Magnetism and Magnetic Materials, 2017. **432**: p. 140-153.

70. Braune, S., S. Liu, and P. Mercorelli. *Design and control of an electromagnetic valve actuator*. in *Computer Aided Control System Design,*

2006 IEEE International Conference on Control Applications, 2006 IEEE International Symposium on Intelligent Control, 2006 IEEE. 2006. IEEE.

71. Mercorelli, P., K. Lehmann, and S. Liu. *Robust flatness based control of an electromagnetic linear actuator using adaptive PID controller*. in *42nd IEEE Conference on Decision and Control*. 2003.

72. Furlani, E.P., *Permanent magnet and electromechanical devices: materials, analysis, and applications*. 2001: Academic press.

73. Liu, G., M. Shao, W. Zhao, J. Ji, Q. Chen, and Q. Feng, *Modeling and analysis of halbach magnetized permanent-magnets machine by using lumped parameter magnetic circuit method.* Progress In Electromagnetics Research M, 2015. **41**: p. 177-188.

74. Jin, P., Y. Yuan, H. Lin, S. Fang, and S. Ho, *General analytical method for magnetic field analysis of Halbach magnet arrays based on magnetic scalar potential.* Journal of Magnetics, 2013. **18**(2): p. 95-104.

75. Jang, S.-M. and J.-Y. Choi, *Analytical prediction for electromagnetic characteristics of tubular linear actuator with Halbach array using transfer relations.* Journal of Electrical Engineering and Technology, 2007. **2**(2): p. 221-230.

76. Wu, L., Z. Zhu, D. Staton, M. Popescu, and D. Hawkins, *Analytical prediction of electromagnetic performance of surface-mounted PM machines based on subdomain model accounting for tooth-tips.* IET electric power applications, 2011. **5**(7): p. 597-609.

77. Wu, L., Z. Zhu, D. Staton, M. Popescu, and D. Hawkins, *Subdomain model for predicting armature reaction field of surface-mounted permanent-magnet machines accounting for tooth-tips.* IEEE Transactions on Magnetics, 2011. **47**(4): p. 812-822.

78. Markovic, M. and Y. Perriard, *Optimization design of a segmented Halbach permanent-magnet motor using an analytical model.* IEEE Transactions on Magnetics, 2009. **45**(7): p. 2955-2960.

79. Mellor, P.H. and R. Wrobel, *Optimization of a multipolar permanent-magnet rotor comprising two arc segments per pole.* IEEE Transactions on Industry Applications, 2007. **43**(4): p. 942-951.

80. Kumar, P. and P. Bauer, *Improved analytical model of a permanent-magnet brushless DC motor.* IEEE Transactions on Magnetics, 2008. **44**(10): p. 2299-2309.

81. Boughrara, K., D. Zarko, R. Ibtiouen, O. Touhami, and A. Rezzoug, *Magnetic field analysis of inset and surface-mounted permanent-magnet synchronous motors using Schwarz–Christoffel transformation.* IEEE Transactions on Magnetics, 2009. **45**(8): p. 3166-3178.

82. Wu, L., Z. Zhu, D. Staton, M. Popescu, and D. Hawkins, *Combined complex permeance and sub-domain model for analytical predicting electromagnetic performance of surface-mounted PM machines.* 2010.

83. Zhu, Z. and D. Howe, *Analytical prediction of the cogging torque in radial-field permanent magnet brushless motors.* IEEE transactions on magnetics, 1992. **28**(2): p. 1371-1374.

84. Zarko, D., D. Ban, and T.A. Lipo, *Analytical calculation of magnetic field distribution in the slotted air gap of a surface permanent-magnet motor using complex relative air-gap permeance.* IEEE Transactions on Magnetics, 2006. **42**(7): p. 1828-1837.

85. Zarko, D., D. Ban, and T.A. Lipo, *Analytical solution for cogging torque in surface permanent-magnet motors using conformal mapping.* IEEE Transactions on Magnetics, 2008. **44**(1): p. 52-65.

86. Zhu, L., S. Jiang, Z. Zhu, and C. Chan, *Analytical methods for minimizing cogging torque in permanent-magnet machines.* IEEE transactions on magnetics, 2009. **45**(4): p. 2023-2031.

87. De La Ree, J. and N. Boules, *Torque production in permanent-magnet synchronous motors.* IEEE Transactions on industry applications, 1989. **25**(1): p. 107-112.

88. Pellegrino, G., A. Vagati, B. Boazzo, and P. Guglielmi, *Comparison of induction and PM synchronous motor drives for EV application including design examples.* IEEE Transactions on industry applications, 2012. **48**(6): p. 2322-2332.

89. Cui, J., W. Xiao, X. Zhang, X. Zhang, P. Zhang, P. Chen, H. Huang, and X. Wu. *Electric Submersible Progressing Cavity Pump Driven by Low-Speed Permanent Magnet Synchronous Motor*. in *SPE Middle East Artificial Lift Conference and Exhibition*. 2016. Society of Petroleum Engineers.

90. Huynh, T. and M.-F. Hsieh, *Performance analysis of permanent magnet motors for electric vehicles (EV) traction considering driving cycles.* Energies, 2018. **11**(6): p. 1385.

91. https://www.eia.gov, 2019.

92. Ehsani, M., Y. Gao, S. Longo, and K. Ebrahimi, *Modern electric, hybrid electric, and fuel cell vehicles*. 2018: CRC press.

93. Chan, C., K. Chau, and K. Chau, *Modern electric vehicle technology*. Vol. 47. 2001: Oxford University Press on Demand.

94. Pillay, P. and R. Krishnan, *Modeling, simulation, and analysis of permanent-magnet motor drives. I. The permanent-magnet synchronous motor drive.* IEEE Transactions on industry applications, 1989. **25**(2): p. 265-273.

95. Chau, K., C.C. Chan, and C. Liu, *Overview of permanent-magnet brushless drives for electric and hybrid electric vehicles.* IEEE Transactions on industrial electronics, 2008. **55**(6): p. 2246-2257.

96. Zeraoulia, M., M.E.H. Benbouzid, and D. Diallo, *Electric motor drive selection issues for HEV propulsion systems: A comparative study.* IEEE Transactions on Vehicular technology, 2006. **55**(6): p. 1756-1764.

97. Xue, X., K. Cheng, and N. Cheung. *Selection of electric motor drives for electric vehicles*. in *2008 Australasian Universities Power Engineering Conference*. 2008. IEEE.

98. Yildirim, M., M. Polat, and H. Kürüm. *A survey on comparison of electric motor types and drives used for electric vehicles*. in *2014 16th International*

Power Electronics and Motion Control Conference and Exposition. 2014. IEEE.

99. Mallek, M., Y. Tang, J. Lee, T. Wassar, M.A. Franchek, and J. Pickett, *An Analytical Subdomain Model of Torque Dense Halbach Array Motors.* Energies, 2018. **11**(12): p. 3254.

100. Jian, L. and C. KT, *Design and analysis of an integrated Halbach-magnetic-geared permanent-magnet motor for electric vehicles.* Journal of Asian Electric Vehicles, 2009. **7**(1): p. 1213-1219.

101. Dubois, M.R. and J.P. Trovao. *Motor Drive with Halbach Permanent Magnet Array for Urban Electric Vehicle Concept*. in *2015 IEEE Vehicle Power and Propulsion Conference (VPPC)*. 2015. IEEE.

102. Wang, J., X. Yuan, and K. Atallah, *Design optimization of a surface-mounted permanent-magnet motor with concentrated windings for electric vehicle applications.* IEEE Transactions on Vehicular Technology, 2012. **62**(3): p. 1053-1064.

103. Gu, W., X. Zhu, L. Quan, and Y. Du, *Design and optimization of permanent magnet brushless machines for electric vehicle applications.* Energies, 2015. **8**(12): p. 13996-14008.

104. Laskaris, K.I. and A.G. Kladas, *Internal permanent magnet motor design for electric vehicle drive.* IEEE Transactions on Industrial Electronics, 2009. **57**(1): p. 138-145.

105. Wang, A., Y. Jia, and W. Soong, *Comparison of five topologies for an interior permanent-magnet machine for a hybrid electric vehicle.* IEEE Transactions on Magnetics, 2011. **47**(10): p. 3606-3609.

106. Rahman, K.M. and M. Ehsani. *Performance analysis of electric motor drives for electric and hybrid electric vehicle applications*. in *Power Electronics in Transportation*. 1996. IEEE.

107. Williamson, S.S., A. Emadi, and K. Rajashekara, *Comprehensive efficiency modeling of electric traction motor drives for hybrid electric vehicle propulsion applications.* IEEE Transactions on Vehicular Technology, 2007. **56**(4): p. 1561-1572.

108. Ghozzi, S., K. Jelassi, and X. Roboam. *Energy optimization of induction motor drives*. in *2004 IEEE International Conference on Industrial Technology, 2004. IEEE ICIT'04.* 2004. IEEE.

109. Huang, Z., X. Huang, J. Zhang, Y. Fang, and Q. Lu, *Design of an interior permanent magnet synchronous traction motor for high speed railway applications.* 2012.

110. Diao, L.-J., D.-n. Sun, K. Dong, L.-T. Zhao, and Z.-G. Liu, *Optimized design of discrete traction induction motor model at low-switching frequency.* IEEE Transactions on Power Electronics, 2012. **28**(10): p. 4803-4810.

111. Sarigiannidis, A.G., M.E. Beniakar, and A.G. Kladas, *Fast adaptive evolutionary PM traction motor optimization based on electric vehicle drive cycle.* IEEE Transactions on Vehicular Technology, 2016. **66**(7): p. 5762-5774.

112. Degano, M., E. Carraro, and N. Bianchi. *Robust optimization of a traction PMASR motor according to given driving cycles*. in *2014 International Conference on Electrical Machines (ICEM)*. 2014. IEEE.

113. Carraro, E., M. Morandin, and N. Bianchi. *Optimization of a traction PMASR motor according to a given driving cycle*. in *2014 IEEE Transportation Electrification Conference and Expo (ITEC)*. 2014. IEEE.

114. Dubois, M.R. and G. Mailloux, *Analytical calculation of no-load voltage waveforms in machines based on permanent-magnet volume integration.* IEEE Transactions on Magnetics, 2008. **44**(5): p. 581-589.

115. Carraro, E., M. Morandin, and N. Bianchi, *Traction PMASR motor optimization according to a given driving cycle.* IEEE Transactions on Industry Applications, 2015. **52**(1): p. 209-216.

116. Husain, I. and M.S. Islam, *Design, modeling and simulation of an electric vehicle system.* SAE transactions, 1999: p. 2168-2176.

117. Ehsani, M., K.M. Rahman, and H.A. Toliyat, *Propulsion system design of electric and hybrid vehicles.* IEEE Transactions on industrial electronics, 1997. **44**(1): p. 19-27.

118. Sato, Y., S. Ishikawa, T. Okubo, M. Abe, and K. Tamai, *Development of high response motor and inverter system for the Nissan LEAF electric vehicle*. 2011, SAE Technical Paper.

119. Burress, T. *Benchmarking state-of-the-art technologies*. in *Oak Ridge National Laboratory (ORNL), 2013 US DOE Hydrogen and Fuel Cells Program and*

Vehicle Technologies Program Annual Merit Review and Peer Evaluation Meeting. 2013.

120. Rogers, S., *Annual progress report advanced power electronics and electric motors Program.* US Department of Energy, DOE/EE-0864, 2013.

121. Act, F.Q.P., *United States Environmental Protection Agency (USEPA).* Food Quality Protection Act (Public Law. 104Ð170), 1996.

122. Xue, X., K.W.E. Cheng, T.W. Ng, and N.C. Cheung, *Multi-objective optimization design of in-wheel switched reluctance motors in electric vehicles.* IEEE Transactions on industrial electronics, 2010. **57**(9): p. 2980-2987.

123. Hoffmann, C., H. Freudenberg, H. Gerken, M. Hecker, and R. Pirkl, *Device and method for driving at least one capacitive actuator*. 2000, Google Patents.

124. Fujimoto, Y., T. Kominami, and H. Hamada, *Development and analysis of a high thrust force direct-drive linear actuator.* IEEE Transactions on Industrial Electronics, 2009. **56**(5): p. 1383-1392.

125. Wang, J., G.W. Jewell, and D. Howe, *A general framework for the analysis and design of tubular linear permanent magnet machines.* IEEE Transactions on Magnetics, 1999. **35**(3): p. 1986-2000.

126. Faus, H.T., *Magnetic transmission*. 1945, Google Patents.

127. Krebs, G., A. Tounzi, B. Pauwels, D. Willemot, and F. Piriou, *Modeling of a linear and rotary permanent magnet actuator.* IEEE Transactions on Magnetics, 2008. **44**(11): p. 4357-4360.

128. Becherini, G. and B. Tellini, *Helicoidal electromagnetic field for coilgun armature stabilization.* IEEE transactions on magnetics, 2003. **39**(1): p. 108-111.

129. Chitayat, A., *Rotary-linear actuator*. 2001, Google Patents.

130. Wang, J., K. Atallah, and W. Wang, *Analysis of a magnetic screw for high force density linear electromagnetic actuators.* IEEE Transactions on Magnetics, 2011. **47**(10): p. 4477-4480.

131. Holm, R.K., N.I. Berg, M. Walkusch, P.O. Rasmussen, and R.H. Hansen, *Design of a magnetic lead screw for wave energy conversion.* IEEE Transactions on Industry Applications, 2013. **49**(6): p. 2699-2708.

132. Ji, J., Z. Ling, J. Wang, W. Zhao, G. Liu, and T. Zeng, *Design and analysis of a Halbach magnetized magnetic screw for artificial heart.* IEEE Transactions on Magnetics, 2015. **51**(11): p. 1-4.

133. Jenney, K. and S. Pakdelian. *Design and Fabrication of the Trans-Rotary Magnetic Gear Using Quasi-Halbach Arrays*. in *IECON 2018-44th Annual Conference of the IEEE Industrial Electronics Society*. 2018. IEEE.

134. Lu, K., Y. Xia, W. Wu, and L. Zhang, *New helical-shape magnetic pole design for magnetic lead screw enabling structure simplification.* IEEE Transactions on Magnetics, 2015. **51**(11): p. 1-4.

135. Qi, Z., P. Mengchun, and C. Dixiang. *Analytic calculation of magnetic field and force in Halbach permanent magnet linear motor*. in *Electronic Measurement & Instruments (ICEMI), 2011 10th International Conference on*. 2011. IEEE.

136. Xiao-Fan, G., Y. Yong, and Z. Xiao-Jing, *Analytic expression of magnetic field distribution of rectangular permanent magnets.* Applied mathematics and mechanics, 2004. **25**(3): p. 297-306.

137. Ngatchou, P., A. Zarei, and A. El-Sharkawi. *Pareto multi objective optimization*. in *Proceedings of the 13th International Conference on, Intelligent Systems Application to Power Systems*. 2005. IEEE.